Standard Model Higgs Boson Phenomenology at Hadron Colliders

Mariano L. Ciccolini

A thesis submitted to the University of Edinburgh for the degree of

Doctor of Philosophy

in the School of Physics

November 5, 2004

Declaration

I declare that I am the sole author of this thesis, and that the work presented is my own, except where otherwise acknowledged. I further state that no part of this thesis has already been or is being concurrently submitted for any other degree or professional qualification.

Abstract

In this thesis two different aspects of Standard Model Higgs boson phenomenology at hadron colliders are addressed. A precise theoretical knowledge of production cross sections is needed in order to assist in the Higgs boson search efforts of the experimental community. Consequently, the next-to-leading-order electroweak corrections to Higgs boson production in association with a vector boson at hadron colliders have been calculated. Significant corrections were found, and theoretical uncertainties were analysed.

In addition to production cross sections, a deep knowledge of background processes is also needed, especially at hadron colliders. The gluon-induced contributions to off-shell W-boson pair production have been calculated. The invariant amplitude has been used to calculate the contribution from gluon initiated processes to the non-resonant W-boson pair production background to the Higgs boson search channel $gg \to H \to W^-W^+ \to l^-\bar{\nu}_l\, l'^+\nu_{l'}$ at the CERN LHC. These contributions are evaluated in the approximation of massless quarks circulating the loops. These results were used to study the effect of experimental cuts proposed to increase the signal to background ratio of the above mentioned search channel.

Acknowledgements

The research described in Chapter 4 was a collaboration with Stefan Dittmaier and Michael Krämer, who independently checked the results. O. Brein, A. Djouadi and R. Harlander provided the necessary QCD data for the combination of EW and NNLO QCD results. The research described in Chapter 5 was a collaboration with Thomas Binoth, Nikolas Kauer and Michael Krämer, who independently checked the results.

I kindly acknowledge financial support from the University of Edinburgh and the ORS-Scheme Award ORS/2001014035.

I would like to thank my supervisor, Michael Krämer, for all the knowledge, advice and support. I would also like to thank the Particle Physics Theory Group, for providing a very nice and stimulating research environment.

A great thanks to friends, here in Edinburgh, and everywhere. A huge thanks to my parents. And the greatest thanks of all to Karina, who has always been by my side throughout all these years: this thesis is dedicated to her.

Contents

Abstract iii

Table of Contents vii

List of Figures x

List of Tables xii

1 Introduction 1

2 The Standard Model 6

2.1 Spontaneous Symmetry Breaking 6

2.1.1 The linear σ Model 7

2.1.2 Goldstone Theorem 9

2.2 Spontaneous Symmetry Breaking in Gauge Theories: the Higgs Mechanism 11

2.3 Electroweak Theory 13

2.3.1 The classical Lagrangian 14

2.4 Electroweak Symmetry Breaking 16

2.5 Quantization and Gauge fixing 18

3 Higgs boson phenomenology 20

3.1 SM Higgs Mass 20

3.2 SM Higgs Decay 24

3.3 SM Higgs Production 26

3.4 Higgs Boson Searches at Hadron Colliders 29

3.4.1 Higgs Boson Searches at the Fermilab TEVATRON 30

3.4.2 Higgs Boson Searches at the CERN LHC 30

4 Vector Boson Associated Production **36**

4.1 Introduction 36

4.2 The Parton Cross Section 38

4.2.1 Conventions and lowest-order Cross Section 38

4.2.2 Virtual Corrections 40

4.2.3 Real-photon Emission 48

4.2.4 Treatment of Soft and Collinear Singularities 48

4.3 The Hadron Cross Section 53

4.4 Numerical Results 54

4.4.1 Input Parameters 54

4.4.2 Electroweak Corrections 55

4.4.3 The Cross Section at NLO 63

4.5 Electroweak NLO and QCD NNLO Corrections 70

4.6 Conclusions 77

5 Gluon induced $W^{\pm}$ boson pair production **78**

5.1 Introduction 79

5.1.1 Searching for a SM Higgs with $155\,\text{GeV} < M_H < 180\,\text{GeV}$ 79

5.1.2 Vector Boson pair Production at Hadron Colliders 85

5.2 The $gg \to W^{+*}W^{-*}$ Invariant Amplitude 87

5.2.1 Calculation Details 92

5.2.2 Ultraviolet and Infrared Divergences 94

5.3 Gluon Induced off-shell W^+W^- Production with Decay into lepton-neutrino pairs 95

5.3.1 Gauge Invariance 97

5.4 The Massless Case 98

5.5 Numerical Evaluation 100

5.5.1 Methodology 100

5.5.2 Input Parameters 101

5.5.3 Technical and signal-enhancing Cuts 102

5.5.4 Cross Section Results 102

5.6 Conclusions 109

6 Conclusions **110**

A Spinor Helicity Formalism **112**

B Function Base for $gg \to W^-W^+$ processes **114**

C Phase Space Parametrization **116**

List of Figures

1.1 Measured and fitted values of Standard Model Electroweak parameters. 2

1.2 Energy dependence of characteristic cross sections at hadron colliders. . 4

3.1 Higgs Boson mass limits from theoretical considerations. 21

3.2 Comparison of direct and indirect measurements for m_t and M_H. 22

3.3 $\Delta\chi^2$ corresponding to the fit of the Higgs boson mass to the Standard Model electroweak parameters. 23

3.4 Total Higgs boson width vs. M_H. 25

3.5 Higgs boson branching ratio vs. M_H 25

3.6 Higgs production mechanisms at an e^+e^- collider. 26

3.7 Tree level, parton Feynman diagrams for hadronic Higgs production processes. 27

3.8 CERN LHC Higgs boson production cross sections. 28

3.9 Fermilab TEVATRON Higgs boson production cross sections. 28

3.10 Required luminosity for Higgs boson detection at Fermilab TEVATRON. . 31

3.11 ATLAS experiment SM Higgs signal significance for $\int \mathcal{L} = 30\,\mathrm{fb}^{-1}$. 35

3.12 CMS experiment SM Higgs signal significance for $\int \mathcal{L} = 30\,\mathrm{fb}^{-1}$. 35

4.1 Lowest-order diagram for $q\bar{q}' \to V^* \to VH$ $(V = W, Z)$. 38

4.2 Contributions of different vertex functions to $u\bar{d} \to WH$. 40

4.3 Contributions of different vertex functions to $q\bar{q} \to ZH$. 40

4.4 Diagrams for the corrections to the $u\bar{d}W$ vertex. 41

4.5 Diagrams for the corrections to the $q\bar{q}Z$ vertices. 41

4.6 Diagrams for the corrections to the $q\bar{q}H$ vertices. 41

4.7 Diagrams for the corrections to the WWH vertex. 42

4.8 Diagrams for the corrections to the ZZH vertices. 43
4.9 Diagrams for box corrections to $u\bar{d} \to WH$. 44
4.10 Diagrams for box corrections to $q\bar{q} \to ZH$. 44
4.11 Bremsstrahlung diagrams for $u\bar{d} \to WH + \gamma$. 48
4.12 Bremsstrahlung diagrams for $q\bar{q} \to ZH + \gamma$. 48
4.13 δ^{EW} vs. M_H for $p\bar{p} \to W^+H + X$ ($\sqrt{s} = 1.96$ TeV) 56
4.14 δ^{EW} vs. M_H for $p\bar{p} \to ZH + X$ ($\sqrt{s} = 1.96$ TeV) 56
4.15 δ^{EW} vs. M_H for $pp \to W^+H + X$ ($\sqrt{s} = 14$ TeV) 59
4.16 δ^{EW} vs. M_H for $pp \to ZH + X$ ($\sqrt{s} = 14$ TeV) 59
4.17 Different contributions to $\delta^{\mathrm{EW}}_{G_\mu}$ for $p\bar{p} \to W^+H + X$ ($\sqrt{s} = 1.96$ TeV) . 61
4.18 Different contributions to $\delta^{\mathrm{EW}}_{G_\mu}$ for $p\bar{p} \to ZH + X$ ($\sqrt{s} = 1.96$ TeV) . . . 61
4.19 Different contributions to $\delta^{\mathrm{EW}}_{G_\mu}$ for $pp \to W^+H + X$ ($\sqrt{s} = 14$ TeV) . . 62
4.20 Different contributions to $\delta^{\mathrm{EW}}_{G_\mu}$ for $pp \to ZH + X$ ($\sqrt{s} = 14$ TeV) 62
4.21 Total cross section for $p\bar{p} \to W^{\pm}H + X$ ($\sqrt{s} = 1.96$ TeV) 66
4.22 Total cross section for $p\bar{p} \to ZH + X$ ($\sqrt{s} = 1.96$ TeV) 66
4.23 Total cross section for $pp \to W^{\pm}H + X$ ($\sqrt{s} = 14$ TeV) 67
4.24 Total cross section for $pp \to ZH + X$ ($\sqrt{s} = 14$ TeV) 67
4.25 K-factor for the LO, NLO and NNLO QCD corrected cross section for $p\bar{p} \to WH + X$ at the Fermilab Tevatron. 72
4.26 K-factor for the LO, NLO and NNLO QCD corrected cross section for $pp \to WH + X$ at the CERN LHC. 72
4.27 K-factor for the NNLO QCD and NLO EW corrected cross section for $p\bar{p} \to WH + X$ at the Fermilab Tevatron. 73
4.28 K-factor for the NNLO QCD and NLO EW corrected cross section for $pp \to WH + X$ at the CERN LHC. 73
4.29 K-factor for the NNLO QCD and NLO EW corrected cross section for $p\bar{p} \to ZH + X$ at the Fermilab Tevatron. 74
4.30 K-factor for the NNLO QCD and NLO EW corrected cross section for $pp \to ZH + X$ at the CERN LHC. 74
4.31 Total cross section including NNLO QCD and electroweak corrections for ZH and WH production at the Fermilab Tevatron. 75

4.32 Total cross section including NNLO QCD and electroweak corrections for ZH and WH production at the CERN LHC. 75

5.1 Parton distribution functions products as a function of parton momentum fraction. 83

5.2 Feynman diagrams contributing to the gluon-induced off-shell production of W-boson pairs. 89

5.3 Single-resonant diagrams contributing to off-shell W boson pair production. 97

5.4 Ward Identity that must be satisfied by the gauge invariant amplitude. . 97

5.5 Invariant mass distributions for gluon and quark induced on-shell W^+W^-+ X production at a pp collider with center of mass energy $\sqrt{s} = 14\,\text{TeV}$. . 103

5.6 Total cross section for the gluon induced contribution to the process $pp \to W^-W^+ \to l^-\bar{\nu}\, l'^+\nu_{l'} + X$ as a function of the technical cut p_T^{cut}. . 105

5.7 p_T distributions for gluon and quark induced contributions to the process $pp \to W^-W^+ \to l^-\bar{\nu}\, l'^+\nu_{l'} + X$. 105

5.8 Total cross section for the gluon induced contribution to the process $pp \to W^-W^+ \to l^-\bar{\nu}\, l'^+\nu_{l'} + X$ as a function of the technical cut p_T^{cut}, after applying the signal-enhancing cuts. 107

5.9 p_T distributions for gluon and quark induced contributions to the process $pp \to W^-W^+ \to l^-\bar{\nu}\, l'^+\nu_{l'} + X$, including the signal-enhancing cuts. . . 107

List of Tables

4.1 Total lowest-order hadronic cross section $\sigma_0(p\bar{p} \to W^+H + X)$ and corresponding relative electroweak correction δ ($\sqrt{s} = 1.96$ TeV). 57

4.2 Total lowest-order hadronic cross section $\sigma_0(p\bar{p} \to ZH + X)$ and corresponding relative electroweak correction δ ($\sqrt{s} = 1.96$ TeV). 57

4.3 Total lowest-order hadronic cross section $\sigma_0(pp \to W^+H + X)$ and corresponding relative electroweak correction δ ($\sqrt{s} = 14$ TeV). 60

4.4 Total lowest-order hadronic cross section $\sigma_0(pp \to ZH + X)$ and corresponding relative electroweak correction δ ($\sqrt{s} = 14$ TeV). 60

4.5 NLO QCD and EW corrected total cross section for $p\bar{p} \to W^{\pm}H + X$ (sum of W^+H and W^-H) at the Tevatron. 64

4.6 NLO QCD and EW corrected total cross section for $p\bar{p} \to ZH + X$ at the Tevatron. 64

4.7 NLO QCD and EW corrected total cross section for $pp \to W^{\pm}H + X$ at the LHC. 65

4.8 NLO QCD and EW corrected total cross section for $pp \to ZH + X$ at the LHC 65

4.9 PDF uncertainties in the total cross section for $p\bar{p} \to W^{\pm}H + X$ at the Tevatron. 68

4.10 PDF uncertainties in the total cross section for $p\bar{p} \to ZH + X$ at the Tevatron. 68

4.11 PDF uncertainties in the total cross section for $pp \to W^{\pm}H + X$ at the LHC. 69

4.12 PDF uncertainties in the total cross section for $pp \to ZH + X$ at the LHC. 69

4.13 Cross section uncertainty due to renormalization and factorization scale dependence. 76

5.1 Leptons spectra cuts from ref. [112] 85

5.2 Total cross section for gluon and quark induced contributions to the process $pp \to W^+W^-$, with $\sqrt{s} = 14\,\text{TeV}$. 104

5.3 Total cross section for gluon and quark induced contributions to the process $pp \to W^+W^- \to l^-\bar{\nu}l'^+\nu_{l'}$, with $\sqrt{s} = 14\,\text{TeV}$. 104

5.4 Same as table 5.3, but the three physical cuts described in Section 5.5.3 have been applied. 104

5.5 Cuts effect summary. 108

Chapter 1

Introduction

These are exciting times for the particle physics community. Since its proposal almost 40 years ago, the Standard Model of Particle Interactions[1]–[4], has become the most successful theory describing elementary particle phenomena. An example of the achievements of the Standard Model is the prediction of the existence of the massive $W^{\pm}$ and Z bosons, and of the bottom and top quarks.

With the 1975 discovery of the τ lepton[5] the hint of a third generation of particles appeared. Two years later, at Fermilab, the down-type quark of the third generation, the bottom quark, was discovered[6]. The Standard Model predicts a corresponding third generation up-type quark, the top quark, which was discovered in 1994 also at Fermilab[7, 8]. On the other hand, in 1983 the existence of the massive gauge bosons was confirmed, when these particles were discovered at the CERN SPS UA1 and UA2 experiments[9]–[11].

The success of the Standard Model as a theory of fundamental interactions can also be appreciated in the results of the fits to precision electroweak data, by the LEP Electroweak Working group(LEP EWWG) . This collaboration combines the measurements of the four LEP experiments ALEPH, DELPHI, L3 and OPAL on electroweak observables, such as cross sections, masses and various couplings of the heavy electroweak gauge bosons, properly taking into account the common systematic uncertainties. These results are also compared and combined with other experiments, notably NuTeV, CDF, DO and SLD. Individual electroweak parameters can be chosen to be fitted to the rest of the direct measurements in order to evaluate the validity of the Standard Model. The results obtained by the LEP EWWG are summarized in figure

1.1 [12]. This plot shows the difference between the fitted value of the Standard Model electroweak parameters and their directly measured value in units of standard deviations. Out of 18 quantities, 6 differ more than one standard deviation while only 1

Figure 1.1: Measured and fitted values of Standard Model Electroweak parameters, and the corresponding difference in units of standard deviations, taken from ref. [12].

differs more than 2σ.

Despite these highly successful achievements, there is still a missing piece in the Standard Model framework. After the top quark discovery, there is one elementary particle predicted by the Standard Model that has not been observed, yet: the Higgs boson. The Higgs mechanism[13] is a fundamental element in the Standard Model. It is based on the spontaneous symmetry breaking of the $SU(2)_W \times U(1)_Y$ electroweak symmetry due to the appearance of a nonzero vacuum expectation value of a doublet of charged scalar fields. After symmetry breaking, fermions and gauge bosons acquire a mass, which is otherwise forbidden by gauge invariance, and a new massive scalar particle appears in the physical spectrum: the Higgs boson. In addition to mass generation, the existence of a Higgs boson is necessary for unitarity conservation in scattering amplitudes of gauge bosons at high energies. It is important to note that, although

the Higgs mechanism offers a consistent way of breaking the electroweak symmetry, the Standard Model Higgs sector is not understood from a fundamental point of view. The physics underlying electroweak symmetry breaking is not certain. Given the high theoretical importance of the Higgs boson, its search in current and future experiments is a priority.

Standard Model Higgs boson searches were carried out by ALEPH, DELPHI, L3 and OPAL, at LEP. These collaborations have ruled out with 95% C.L. a Higgs boson lighter than 114.4 GeV[14]. Currently, Higgs boson searches continue at the Fermilab Tevatron, a proton-antiproton collider with a centre-of-mass energy of 1.96 TeV. Provided a high luminosity can be achieved, a Standard Model Higgs boson with mass in the range $100\,\text{GeV} \lesssim M_H \lesssim 200\,\text{GeV}$ could be discovered, or ruled out, at the Tevatron. In 2007 the CERN Large Hadron Collider (LHC) is expected to start operation. The CERN LHC, which has been designed in part as a Higgs boson discovery machine, will be a proton-proton collider with centre-of-mass energy of 14 TeV. The Atlas and CMS experiments have carried out analyses which show that, with an integrated luminosity of only $30\,\text{fb}^{-1}$, a Higgs boson discovery with a statistical significance of 5σ or more is possible across the whole Higgs boson mass range $100\,\text{GeV} - 1\,\text{TeV}$ [15]. This integrated luminosity can be reached after one year of running in the low luminosity configuration. Even if a Higgs boson does not exist, in all theoretical models the dynamics of the electroweak symmetry breaking mechanism must be revealed at the 1 TeV scale or below, and the LHC will be able to probe this energy scale.

In order to assist in these Higgs boson searches, a precise theoretical knowledge of all the processes involved is necessary. Much effort has been devoted in the last years to calculate higher order corrections to hadronic processes involving Higgs boson production. Not only a precise knowledge of Higgs production cross sections is needed, but knowledge of background processes cross sections is also important. This is especially the case at high energy hadron colliders, where the signal from Higgs production processes is generally much smaller than the background. Figure 1.2, taken from ref. [17], shows cross sections for typical processes at hadron colliders as a function of collider energy. It can be seen that typical Higgs production cross sections are 7 orders of magnitude smaller than the $b\bar{b}$ pair production cross section and 11 orders of magnitude smaller than the total cross section. The signal can be effectively recovered from the

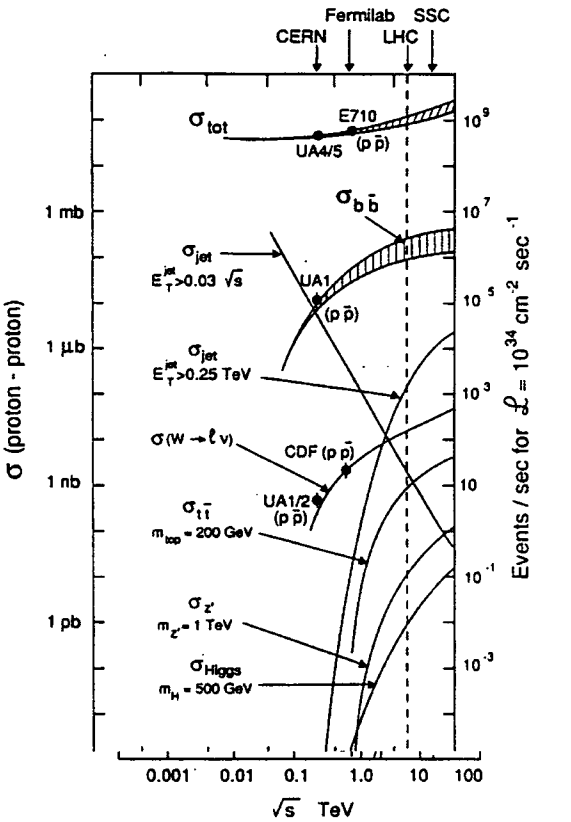

Figure 1.2: Energy dependence of characteristic cross sections at hadron colliders. The energy range covers the following accelerators: CERN SPS, Fermilab Tevatron, CERN LHC and SSC. (Taken from ref. [17].)

background imposing appropriate experimental cuts. However, to be able to assess the effectiveness of these cuts, a precise knowledge of background cross sections is needed.

In this thesis these two aspects of Higgs boson calculations have been explored. Electroweak corrections to Higgs production processes in association with electroweak gauge bosons at hadron colliders, and the cross section of gluon initiated processes contributing to the off-shell W-boson pair production background at the CERN LHC, have been calculated.

At the Fermilab Tevatron

$$p\bar{p} \to VH + X \quad , \quad V = W^{\pm}, Z$$

is the most important Higgs boson production mechanism for a Higgs boson of mass $M_H \lesssim 135\,\mathrm{GeV}$. The next-to-leading-order(NLO) $\mathcal{O}(\alpha)$ electroweak corrections to

Higgs boson production in association with Z- and W-bosons have been calculated. Combination with state-of-the-art next-to-next-to-leading-order(NNLO) QCD corrected results yields the currently most precise Higgs boson production process cross section.

At the future LHC the process

$$gg \to H \to W^-W^+ \to l^-\bar{\nu}l'^+\nu_{l'}$$

is the most promising channel for detecting a Standard Model Higgs-boson with mass in the range 155 GeV − 180 GeV. The main background to this detection channel is vector boson pair production, and the principal contribution to this process is the parton process

$$q\bar{q}' \to W^-W^+ \to l^-\bar{\nu}l'^+\nu_{l'} .$$

The gluon-induced contributions to off-shell W-boson pair production have been calculated. The invariant amplitudes have been used to calculate the contribution from gluon initiated processes to the non-resonant W-boson pair production background process at the CERN LHC, in the approximation of massless quarks circulating the loops. These results were used to study the effect of experimental cuts proposed in [112] to increase the Higgs signal statistical significance.

This thesis is organized as follows: Chapter 2 is a brief review of the Standard Model of particle interactions and the Higgs mechanism. Chapter 3 is a summary of current Standard Model Higgs boson phenomenology. Different Higgs boson mass constraints are studied, Higgs boson decay, production and search strategies at the Fermilab Tevatron and the CERN LHC are discussed. NLO electroweak corrections to vector boson associated production at hadron colliders are presented in Chapter 4. Calculation details are discussed, with emphasis on the treatment of collinear and soft singularities. Numerical results are presented, together with the combination with NNLO QCD corrected results obtained in [57]. Chapter 5 presents the calculation of the invariant amplitude for gluon induced off-shell W-boson pair production. The calculation of the gluon induced contribution to the Higgs search background $pp \to W^+W^- \to l\nu l\nu$ is discussed. After reviewing the calculation techniques, numerical results are presented, including the effect of experimental cuts proposed in [112] to increase the signal to background ratio in Higgs searches at the LHC. Conclusions and possible extensions and improvements to this research are discussed in Chapter 6.

Chapter 2

The Standard Model

The Standard Model is the fundamental theory of particle interactions. It has had extraordinary success in explaining different particle physics phenomena and experimental results. The Standard Model is a non-abelian gauge theory, symmetric under $\mathrm{SU}(2)_W \times \mathrm{U}(1)_Y$ gauge transformations. Gauge invariance is not compatible with the existence of massive gauge bosons. However, the Z and $W^{\pm}$ gauge bosons do have a mass. The solution to this apparent paradox lies in spontaneous symmetry breaking and the Higgs mechanism. This chapter is organized as follows: in Section 2.1 a brief review of spontaneous symmetry breaking in systems with global symmetries, and a classical proof of Goldstone theorem are given. In Section 2.2 the case of theories with local symmetries, gauge theories, is reviewed and the Higgs mechanism is introduced. Finally, in Section 2.3, the Standard Model of electroweak interactions is presented. The different field sectors and electroweak symmetry breaking mechanism are reviewed, with emphasis in obtaining the physical representation of the theory.

2.1 Spontaneous Symmetry Breaking

Consider a theory invariant under a symmetry group G. Two different configurations exist for the lowest energy states, the ground states, of the theory. There may be only one ground state, invariant under G transformations. Or the ground state may be degenerate, where many different lowest energy states exist, all of them transforming into each other under the symmetry group G. If one of these physically equivalent states is chosen as the ground state, the theory is said to have undergone spontaneous

symmetry breaking.

There are many examples in physics of systems with spontaneous symmetry breaking, some of them not belonging to high energy physics. A typical example of a theory with spontaneous symmetry breaking is the infinitely extended ferromagnet [18]. The interaction between the spins in the ferromagnetic material is symmetric under spatial rotations. Consequently, above a critical temperature called the Curie point, the spins are randomly aligned, without a preferred direction. On the other hand, if the temperature is lowered below the Curie point, the system reaches its ground state and the spins spontaneously align in the same random direction. This spin alignment has an observable effect: the system magnetization becomes nonzero.

In a quantum field theory, spontaneous symmetry breaking can be easily analysed at the Lagrangian level. If the Lagrangian is invariant under a symmetry group G, the field configuration that minimizes the interaction potential, the ground state, may be nontrivial, i.e. this field configuration may have a nonzero vacuum expectation value. When this phenomena occurs it is said that the original symmetry G is spontaneously broken by the vacuum expectation values. Early studies of spontaneous symmetry breaking in quantum field theories can be found in refs. [19]-[22].

It is interesting to note that there is a common characteristic in the spontaneous symmetry breaking mechanism in quantum field theories and the ferromagnetic system: in both cases there is an order parameter which is zero for the symmetric theory and acquires a nonzero value in the non-symmetric configuration. In the ferromagnetic system the order parameter is the system magnetization, while in a quantum field theory it is the field vacuum expectation value.

2.1.1 The linear σ Model

In this section the spontaneous symmetry breaking mechanism in theories with global symmetries is studied. A simple example of this type of theories is the Goldstone model, ref. [22]. An extension to the Goldstone model is the the linear σ model, which is analysed in this section. The linear σ model consists of an N-dimensional multiplet of real scalar fields $\varphi_{i=1\ldots N}(x)$ with Lagrangian density

$$\mathcal{L}(\varphi) = \frac{1}{2}(\partial_\mu \varphi)^2 - V(\varphi) \ , \quad V(\varphi) = \frac{\lambda}{4}\left(\varphi^2 - \frac{\mu^2}{\lambda}\right)^2 \ , \quad \mu^2 > 0 \qquad (2.1)$$

The N-multiplet transforms under the symmetry group $SO(N)$ of N-dimensional rotations:

$$\varphi_i' = (R\varphi)_i = R^{ij}\varphi_j \quad \text{with} \quad R_{ij}.R^{jk} = \delta_i^k\,, \tag{2.2}$$

where summation over repeated indices is implied. From this transformation rule it is easy to see that φ^2 is invariant under $SO(N)$, as

$$\varphi'^2 = \varphi_i\,(R^{ij}R^{jk})\,\varphi_k = \varphi^2\,. \tag{2.3}$$

Then, the Lagrangian density is also $SO(N)$ invariant. Another important feature of the Lagrangian is that the term proportional to μ^2 plays the part of the usual mass term but with a -1 sign instead of the usual $+1$ sign. This -1 sign in front of the μ^2 term determines a nontrivial structure for the theory ground state. The classical field configuration $\varphi_0(x)$ that minimizes the potential V satisfies

$$\varphi_0^2 = v^2 = \frac{\mu^2}{\lambda}\,. \tag{2.4}$$

This condition determines an $(N-1)$-dimensional sphere of radius v in configuration space. One may choose a particular ground state configuration φ_0[1],

$$\varphi_0 = (0, 0, \ldots, 0, v)\,, \tag{2.5}$$

and rewrite the field $\varphi(x)$ as

$$\varphi = (\chi_1, \chi_2, \ldots, v + \phi)\,.$$

Replacing this expression into the Lagrangian density 2.1, it takes the form

$$\mathcal{L} = \frac{1}{2}\,(\partial_\mu\phi)^2 - \frac{1}{2}(2\mu^2)\phi^2 + \frac{1}{2}\,(\partial_\mu\chi)^2 - \frac{\lambda}{4}(\chi^2+\phi^2)^2 - \lambda v\phi(\chi^2+\phi^2). \tag{2.6}$$

This new Lagrangian density describes a theory with $N-1$ massless real scalar fields $\chi_{i=1\ldots N-1}$ and one massive real scalar field ϕ, with mass $m_\phi = \sqrt{2}\,\mu$. The original $SO(N)$ symmetry has been broken, but not completely. The new Lagrangian density is explicitly symmetric under transformations belonging to the $SO(N-1)$ group of rotations in $(N-1)$-dimensional configuration space. It is said that the original $SO(N)$ symmetry has been spontaneously broken to $SO(N-1)$. Note that the the number of broken symmetries

$$\mathrm{Dim}[SO(N)] - \mathrm{Dim}[SO(N-1)] = N-1\,,$$

[1] Any other configuration can be obtained from φ_0 applying an $SO(N)$ transformation.

and the number of of massless fields χ_i in the theory after spontaneous symmetry breaking are the same.

2.1.2 Goldstone Theorem

The appearance of $N-1$ massless fields in the linear σ model after spontaneous symmetry breaking is not an exclusive characteristic of this theory. It is a general result known as Goldstone Theorem[22, 23]. The massless fields χ_i are usually known as the Goldstone bosons of the theory. This theorem states that, if the Lagrangian of a given theory is invariant under a set of N symmetry transformations while the vacuum is not, then N massless scalar fields must appear after spontaneous symmetry breaking. In other words, for every spontaneously broken continuous symmetry, the theory must contain a massless particle. In the following paragraphs a proof of Goldstone theorem for classical scalar field theories is presented[24].

Consider a theory with a multiplet of N real scalar fields $\varphi_{i=1\ldots N}(x)$, such that they transform under a real representation T^a of the group G as

$$\begin{aligned} \varphi_i(x) &\rightarrow \exp\left(i\theta^a T^a\right)_{ij} \varphi_j(x)\,, \\ \delta\varphi_i(x) &= i\theta^a T^a_{ij}\varphi_j(x)\,. \end{aligned}$$

If the interaction potential $V(\varphi)$ of the theory is invariant under symmetry transformations of the group G, it can be shown that $V(\varphi)$ satisfies

$$\frac{\partial V}{\partial \varphi_j} T^a_{ji} + \frac{\partial^2 V}{\partial \varphi_i \partial \varphi_k} T^a_{kl}\varphi_l = 0. \tag{2.7}$$

As in the example in the previous section, spontaneous symmetry breaking occurs when there are nontrivial field configurations $\varphi_i = v_i$ that minimize the potential. For these minima to exist, the conditions

$$\left.\frac{\partial V}{\partial \varphi_i}\right|_{\varphi=v} = 0 \tag{2.8}$$

$$\left.\frac{\partial^2 V}{\partial \varphi_i \partial \varphi_j}\right|_{\varphi=v} = [M^2]_{ij}, \tag{2.9}$$

where the matrix $[M^2]_{ij}$ should be positive semidefinite, must be satisfied. Introducing the auxiliary fields $\chi_i(x) = \varphi_i(x) - v_i$, the Lagrangian density can be rewritten as

$$\mathcal{L} = \frac{1}{2}(\partial\chi)^2 - \chi_i \left.\frac{\partial^2 V}{\partial \varphi_i \partial \varphi_j}\right|_{\varphi=v} \chi_j + \ldots\,. \tag{2.10}$$

It can be seen that the term with the second derivative of the interaction potential is a mass term for the fields χ_i, and the mass matrix is $[M^2]_{ij}$.

To extract information about the mass matrix $[M^2]_{ij}$, eq. 2.7 can be evaluated on the ground state,

$$[M^2]_{ik} T^a_{kl} v_l = 0. \tag{2.11}$$

In general, there is always a subgroup $H \subset G$ under which the degenerate ground state $\varphi_i = v_i$ is invariant. Then, the generators of the symmetry group can always be chosen to be

$$G'^a = \left\{ H^b, T'^c \right\} \quad , \quad \text{with} \begin{cases} a &= 1 \ldots \mathrm{Dim}(G) , \\ b &= 1 \ldots \mathrm{Dim}(H) , \\ c &= 1 \ldots \mathrm{Dim}(G) - \mathrm{Dim}(H) , \end{cases}$$

where H^a are the generators of the subgroup H, and T'^a are generators of the group G which also expand the coset G/H. Using this choice of generators, the invariance of the ground state translates to

$$H^b_{ij} v_j = 0 \ , \quad b = 1 \ldots \mathrm{Dim}(H) , \tag{2.12}$$

$$T'^c_{ij} v_j \neq 0 \ , \quad c = 1 \ldots \mathrm{Dim}(G) - \mathrm{Dim}(H) . \tag{2.13}$$

Then, if eq. (2.11) must be satisfied for all G generators, there must be at least $\mathrm{Dim}(G) - \mathrm{Dim}(H)$ zero eigenvalues of $[M^2]$, and the fields associated with these eigenvalues will be massless. This proves Goldstone theorem: $\mathrm{Dim}(G) - \mathrm{Dim}(H)$ symmetries are broken, and this implies the existence of the same number of massless fields, the Goldstone bosons of the theory.

The above proof of Goldstone theorem is valid in the first order of the semi-classical approximation of the quantum theory. It can be shown that Goldstone theorem also holds in the quantized theory. For an example of a proof using the path-integral formalism, see ref. [24].

2.2 Spontaneous Symmetry Breaking in Gauge Theories: the Higgs Mechanism

In the previous section, the spontaneous symmetry breaking mechanism in theories with global symmetries was studied. In this section, theories with *local* symmetries, gauge theories, are analysed. Gauge invariance under a group G is assumed. The Lagrangian density for a pure non-abelian gauge theory with gauge fields $A_\mu^{i=1...\,\mathrm{Dim}(G)}(x)$ reads

$$\mathcal{L}_A = -\frac{1}{4}(F_{\mu\nu}^i)^2\,, \tag{2.14}$$

with the gauge field tensor $F_{\mu\nu}^i$ defined as

$$F_{\mu\nu}^i = \partial_\mu A_\nu^i - \partial_\nu A_\mu^i + g f^{ijk} A_\mu^j A_\nu^k\,. \tag{2.15}$$

The structure constants f^{abc} are defined as

$$[T^a, T^b] = i f^{abc} T^c$$

where T^a are the generators of the gauge symmetry group. The gauge field $A^i{}_\mu(x)$ transform under the adjoint representation of the gauge group G,

$$A_\mu^i(x) \to A_\mu^i(x) + \frac{1}{g}\partial_\mu \chi^i(x) + f^{abc} A_\mu^b \alpha^c\,. \tag{2.16}$$

An N dimensional scalar multiplet $\phi_{i=1...N}(x)$ can be introduced, minimally coupled to the gauge field, without breaking gauge invariance. This scalar multiplet is assumed to transform under a representation τ^a of the gauge symmetry group generators T^a,

$$\phi_i \to (1 + i\alpha^a \tau^a)_{ij}\, \phi_j\,. \tag{2.17}$$

The gauge and scalar fields couple minimally, and this coupling is determined by the covariant derivative

$$D_\mu \phi = \partial_\mu \phi - i g A_\mu^a \tau^a \phi\,. \tag{2.18}$$

Instead of working with the complex fields $\phi_{1...N}(x)$ one can always work with the real fields $\phi_{1...2N}(x)$. Keeping the same notation, the representation matrices must be pure imaginary and antisymmetric. The real antisymmetric representation matrices t^a can be introduced as

$$\tau_{ij}^a = i t_{ij}^a\,. \tag{2.19}$$

In this case the covariant derivative can be written as

$$D_\mu \phi = \partial_\mu \phi + g A_\mu^a t^a \phi \tag{2.20}$$

The gauge invariant Lagrangian density for the scalar field is

$$\mathcal{L}_\phi = \frac{1}{2}(D_\mu \phi)^2 - V(\phi) \quad , \qquad V(\phi) = -\mu^2 \phi^\dagger \phi + \lambda (\phi^\dagger \phi)^2 \, , \tag{2.21}$$

and the contribution from the kinetic term reads

$$\frac{1}{2}(D_\mu \phi)^2 = \frac{1}{2}(\partial_\mu \phi)^2 + g A_\mu^a (\partial_\mu \phi_i t_{ij}^a \phi_j) + \frac{1}{2} g^2 A_\mu^a A^{b\mu} (t^a \phi)_i (t^b \phi)_i \, . \tag{2.22}$$

As in the global symmetry case, there are nontrivial configurations of the scalar multiplet that yield a stable degenerate minimum for the potential. These configurations ϕ_0 satisfy the condition

$$\phi_0{}^\dagger \phi_0 = \frac{\mu^2}{\lambda} \, . \tag{2.23}$$

Choosing one particular ground state ϕ_0, rewriting the scalar field as

$$\phi(x) = \phi_0 + h(x) \tag{2.24}$$

and replacing into the scalar field Lagrangian, it can be seen that a mass term for the gauge fields arises from the kinetic term

$$\Delta \mathcal{L}_\phi = \frac{1}{2} g^2 (t^a \phi_0)_i (t^b \phi_0)_i A_\mu^a A^{b\mu} \, , \tag{2.25}$$

where the mass matrix

$$[M^2]^{ab} = g^2 (t^a \phi_0)_i (t^b \phi_0)_i \tag{2.26}$$

can be defined. As explained in the Goldstone theorem proof, Section 2.1, if the gauge group generators are properly chosen, it is easy to see that the vacuum configuration will be annihilated by some of the new generators, $T^a \phi_0 = 0$. Consequently, the gauge bosons corresponding to these generators will remain massless. On the other hand, as the mass matrix is positive semidefinite, the remaining eigenvalues will be positive, and they will correspond to the new massive gauge bosons.

An important difference between spontaneous symmetry breaking of gauged and ungauged symmetries is the behaviour of Goldstone bosons. In gauged theories, Goldstone bosons can be regarded as parameters of local gauge transformations, they do not form part of the physical spectrum of the theory. Consequently, they can be eliminated

from the theory with an adequate gauge choice. For example, the choice of gauge where the Goldstone fields are set to zero yields a theory where all fields in the Lagrangian correspond to fields in the physical spectrum. This gauge is called the *unitary gauge*[25]. One could also choose a gauge in which, after symmetry breaking, the bilinear terms involving two different fields in the Lagrangian are cancelled out. This choice is called the *'t Hooft gauge*[26]. This gauge yields simpler propagators and interaction vertices than the unitary gauge, but needs the presence of the unphysical Goldstone bosons.

It is important to note that spontaneous symmetry breaking leaves the number of degrees of freedom of the theory unchanged. Before symmetry breaking, and using the same notation as in the Goldstone theorem proof, the number of degrees of freedom is

$$n^f_{\text{before}} = 2\text{Dim}(G) + N\,, \tag{2.27}$$

where the first term comes from the massless gauge field and the second term from the scalar sector. The number of degrees of freedom after symmetry breaking is

$$\begin{aligned} n^f_{\text{after}} &= \\ &= 2\text{Dim}(H) + 3(\text{Dim}(G) - \text{Dim}(H)) + (N - \text{Dim}(G) + \text{Dim}(H))\,, \end{aligned} \tag{2.28}$$

where the first term corresponds to the massless gauge fields, the second term corresponds to the massive gauge fields and the third term correspond to the remaining scalar fields. It is easy to see that

$$n^f_{\text{before}} = 2\text{Dim}(G) + N = n^f_{\text{after}}\,.$$

The usual interpretation is that the degrees of freedom coming from the unphysical Goldstone bosons are absorbed by the gauge fields to create the longitudinal components of the massive vector bosons.

2.3 Electroweak Theory

The Standard Model of electroweak interactions was first proposed for the leptonic sector in refs. [1, 2, 3], and later extended to include the hadronic degrees of freedom in ref. [4]. It is a non-abelian gauge theory with gauge group $\text{SU}(2)_W \times \text{U}(1)_Y$ of weak isospin and hypercharge. Massive gauge bosons are introduced by spontaneous symmetry breaking, with a complex doublet of scalar fields. In this section the

gauge symmetric Standard Model Lagrangian is presented and the rôle of the Higgs mechanism in the mass generation of the physical particles is explained.

2.3.1 The classical Lagrangian

The Standard Model classical theory is formed by three field sectors: the gauge, fermion and scalar sectors. In the quantized theory two more sectors are involved: the gauge fixing sector and the Faddeev-Popov ghosts sector. In the following sections the three classical field sectors are described. The gauge fixing and ghost sectors are described in Section 2.5.

Gauge Sector

There are four gauge fields that transform according to the adjoint representation of $\mathrm{SU}(2)_W \times \mathrm{U}(1)_Y$. The gauge fields Lagrangian can be written as

$$\mathcal{L}_{\text{gauge}} = -\frac{1}{4} F_{1\,\mu\nu} F_1^{\mu\nu} - \frac{1}{4} F_{2\,\mu\nu}^a F_2^{a\,\mu\nu} \quad , \quad a = 1 \ldots 3 \,, \tag{2.29}$$

where the gauge field tensors correspond to

$$F_{1\,\mu\nu} = \partial_\mu B_\nu - \partial_\nu B_\mu \tag{2.30}$$

for the $\mathrm{U}(1)_Y$ field, and

$$F_{2\,\mu\nu}^a = \partial_\mu W_\nu^a - \partial_\nu W_\mu^a + g_2\, \epsilon^{abc} W_\mu^b W_\nu^c \tag{2.31}$$

for the $\mathrm{SU}(2)_W$ field, with ϵ^{abc} the $SU(2)_W$ structure constants. Note that mass terms for the gauge fields are forbidden, as these terms would break gauge invariance.

The coupling to fermions and scalar fields will be determined by the covariant derivative

$$D_\mu = \partial_\mu - i g_2 I_W^a W_\mu^a + i g_1 \frac{Y_W}{2} B_\mu \,, \tag{2.32}$$

where I_W^a are the weak isospin generators, Y_W is the weak hypercharge generator, and g_1 and g_2 are the two gauge coupling constants, corresponding to $U(1)_Y$ and $SU(2)_W$, respectively.

Fermion Sector

Fermions in the Standard Model are arranged in isospin doublets $(\psi_{i,+}, \psi_{i,-})$, where the index runs over the three lepton and quark generations. An important difference exists between the treatment of right-handed $\psi^R = \frac{1+\gamma_5}{2}\psi$ and left-handed $\psi^L = \frac{1-\gamma_5}{2}\psi$ fields in the Standard Model: they transform according to two different representations of the weak isospin group. Right-handed fields transform according to a one dimensional representation, while left-handed fields transform according to the fundamental two-dimensional representation. The theory is chiral, and mass terms are forbidden.

The lepton and quark fields can be used to write the Lagrangian of the fermion sector. If $l_j(x)$ and $\nu_j(x)$ are the charged lepton and neutrino spinor fields, and u_j and d_j are the up- and down-quarks fields, respectively, the weak isospin doublets can be written as

$$L_j^L = \begin{bmatrix} \omega^- \nu_j \\ \\ \omega^- l_j \end{bmatrix} \quad , \quad Q_j^L = \begin{bmatrix} \omega^- u_j \\ \\ \omega^- d_j \end{bmatrix} \quad , \text{ with } \omega^{\pm} = \frac{1}{2}(1 \pm \gamma_5) \; ,$$

and the isospin singlets read

$$l_j^R = \omega^+ l_j \quad , \quad u_j^R = \omega^+ u_j \quad , \quad d_j^R = \omega^+ d_j \, .$$

Note that right handed neutrinos are not included in the original version of the theory. Using this notation the Lagrangian reads

$$\begin{aligned} \mathcal{L}_{\text{ferm}} \;\; = \;\; & i \sum_j \bar{L}_j^L \not{D} L_j^L \; + \; \bar{Q}_j^L \not{D} Q_j^L \\ & + i \sum_j \bar{l}_j^R \not{D} l_j^R + i \sum_j \bar{u}_j^R \not{D} u_j^R + i \sum_j \bar{d}_j^R \not{D} d_j^R \, , \end{aligned} \tag{2.33}$$

where the coupling with the gauge field is assumed to be minimal. Mass terms for the fermions will be introduced after spontaneous symmetry breaking.

Scalar Sector

The scalar sector in the Standard Model consists of a weak-isospin doublet of complex scalar fields $\Phi = (\phi_+, \phi_0)$. Conventionally, the scalar sector is assigned hypercharge $+1$. The scalar sector is responsible for gauge boson and fermion mass generation. The

scalar fields couple minimally to the gauge bosons , while they couple through Yukawa interaction to the massless fermions. The scalar sector Lagrangian can be written as

$$\mathcal{L}_{\text{scalar}} = \tag{2.34}$$
$$D_\mu^\dagger \Phi \, D^\mu \Phi - V(\phi) - \sum_{jk} \left[\bar{L}_j^L G_{jk}^l l_k^R \Phi + \bar{Q}_j^L G_{jk}^u u_k^R \Phi^c + \bar{Q}_j^L G_{jk}^d d_k^R \Phi + \text{ h.c.} \right]$$

were G_{ij}^f are the Yukawa coupling matrices, D_μ is the covariant derivative defined in eq. 2.32, and Φ^c is the charged conjugate scalar field.

In order to allow for spontaneous symmetry breaking, the scalar field self-interaction potential is chosen to be

$$V(\Phi) = \frac{\lambda}{4}(\Phi^\dagger \Phi)^2 \; - \mu^2 \Phi^\dagger \Phi \, . \tag{2.35}$$

The total Lagrangian

The total classical Lagrangian for the Electroweak Standard Model reads

$$\mathcal{L}_{\text{cl}} = \mathcal{L}_{\text{gauge}} + \mathcal{L}_{\text{ferm}} + \mathcal{L}_{\text{scalar}} \, . \tag{2.36}$$

$\mathcal{L}_{\text{cl}}$ is invariant under $\text{SU}(2)_W \times \text{U}(1)_Y$ gauge transformations. The free parameters of the theory are the two gauge couplings g_1 and g_2, the parameters of the Higgs potential μ^2 and λ and the Yukawa coupling matrices G_{ij}^f.

2.4 Electroweak Symmetry Breaking

Given the scalar fields self-interacting potential eq. 2.35, it is easily seen that the theory has a minimum stable configuration for scalar fields satisfying

$$|\langle \Phi \rangle|^2 = \frac{2\mu^2}{\lambda} \equiv \frac{v^2}{2} \, . \tag{2.37}$$

Choosing a ground state annihilated by the electric charge operator,

$$\Phi_0 = \left[0 \, , \, \frac{v}{\sqrt{2}} \right] \tag{2.38}$$

allows the theory obtained after symmetry breaking to be symmetric under $\text{U}(1)_{\text{em}}$, the electromagnetic gauge group. Finally, the doublet of charged scalar fields is rewritten as

$$\Phi = \left[\phi^+(x) \, , \, \frac{1}{\sqrt{2}}(v + \eta(x) + i\chi(x)) \right] \, . \tag{2.39}$$

The fields ϕ^+, $\phi^- = \phi^{+\dagger}$ and χ are the Goldstone bosons of the theory, while $\eta(x)$ is the physical Higgs, which has a mass $M_H = \sqrt{2}\mu$. To simplify the extraction of the physical theory one may choose to work in the unitary gauge ($\phi^\pm = 0$ and $\chi = 0$). Inserting eq. 2.39 into the total Lagrangian density, the vacuum expectation value introduces couplings with mass dimensions and mass terms for the fermions and gauge fields. To diagonalize the resulting mass matrices, the following physical fields are defined:

$$W_\mu^\pm = \frac{1}{\sqrt{2}}(W_\mu^1 \pm iW_\mu^2) \tag{2.40}$$

$$\begin{pmatrix} Z_\mu \\ A_\mu \end{pmatrix} = \begin{pmatrix} \cos(\theta_W) & \sin(\theta_W) \\ -\sin(\theta_W) & \cos(\theta_W) \end{pmatrix} \begin{pmatrix} W_\mu^3 \\ B_\mu \end{pmatrix} \tag{2.41}$$

$$f_i'^L = U_{ik}^{f,L} f_k^L \tag{2.42}$$

$$f_i'^R = U_{ik}^{f,R} f_k^R \quad , \qquad f = \nu, l, u, d, \tag{2.43}$$

where the weak mixing angle θ_W is defined as

$$\cos(\theta_W) = \frac{g_2}{\sqrt{g_1^2 + g_2^2}} . \tag{2.44}$$

With these new field definitions the corresponding masses yield

$$M_W = \frac{1}{2} g_2 v \quad , \quad M_Z = \frac{1}{2}\sqrt{g_1^2 + g_2^2} \quad , \quad \cos(\theta_W) = \frac{M_W}{M_Z} \tag{2.45}$$

$$M_\gamma = 0 \quad , \quad m_{f,i} = \frac{v}{\sqrt{2}} U_{ik}^{f,L} G_{km}^f U^{f,R\dagger}{}_{mi} . \tag{2.46}$$

The electron electric charge e and the quark mixing matrix V_{ij} can be identified from the different couplings in the physical Lagrangian as

$$e = \frac{g_1 g_2}{g_1^2 + g_2^2} \quad , \quad g_1 = \frac{e}{\cos\theta_W} \quad , \quad g_2 = \frac{e}{\sin\theta_W} \tag{2.47}$$

$$V_{ij} = U_{ik}^{u,L} \, U^{d,L\dagger}{}_{kj} . \tag{2.48}$$

Finally, the Lagrangian 2.36 can be rewritten only in terms of physical fields 2.40–2.43 and the physical parameters

$$e \; , \; M_W \; , \; M_Z \; , \; M_H \; , \; m_{f,i} \; , \; V_{ij} . \tag{2.49}$$

2.5 Quantization and Gauge fixing

Once the classical Lagrangian has been obtained, the theory should be quantized. During the quantization process a specific choice of gauge must be made. One may use the set of R_ξ gauges[25], where the gauge fixing function of the Faddeev-Popov formalism is given by

$$\mathcal{L}_{\text{gauge fix}} = -\frac{1}{2}\left[\mathcal{L}^{Z^2} + \mathcal{L}^{\gamma 2} + 2\mathcal{L}^{+}\mathcal{L}^{-}\right] \tag{2.50}$$

$$\mathcal{L}^{\pm} = \frac{1}{\sqrt{\xi_1^W}}\partial^\mu W_\mu^\pm \mp iM_W\sqrt{\xi_2^W}\phi^\pm \tag{2.51}$$

$$\mathcal{L}^{Z} = \frac{1}{\sqrt{\xi_1^Z}}\partial^\mu Z_\mu - M_Z\sqrt{\xi_2^Z}\chi \tag{2.52}$$

$$\mathcal{L}^{\gamma} = \frac{1}{\sqrt{\xi_1^\gamma}}\partial^\mu A_\mu\,. \tag{2.53}$$

One more term must be included in the Lagrangian. This term is the Lagrangian for the Faddeev-Popov ghost terms. In order to compensate the gauge fields unphysical components the following terms must be added to the classical Lagrangian:

$$\mathcal{L}_{\text{ghosts}} = \bar{u}^\alpha \frac{\delta\mathcal{L}^\alpha}{\delta\theta^\beta}u^\beta \quad , \quad \alpha = \pm, \gamma, Z\,, \tag{2.54}$$

where $\bar{u}$, u are the ghost fields, and $\frac{\delta\mathcal{L}^\alpha}{\delta\theta^\beta}$ are the variations of the gauge fixing operators under infinitesimal gauge transformations with parameters θ^β.

With the R_ξ gauges the 't Hooft gauge and the unitary gauge can be easily obtained setting particular values for the parameters ξ^α:

$$R_\xi \begin{cases} \xi^\alpha = 1 \;:\; \text{'t Hooft} - \text{Feynman gauge} \\ \xi^\alpha \to \infty \;:\; \text{Unitary gauge} \end{cases} \tag{2.55}$$

The total Lagrangian for the electroweak standard model is then obtained adding all the previous contributions

$$\mathcal{L}_{\text{SM}} = \mathcal{L}_{\text{cl}} + \mathcal{L}_{\text{gauge fix}} + \mathcal{L}_{\text{ghosts}} \tag{2.56}$$

To conclude, it can be mentioned that the renormalizability of the Standard Model of electroweak interactions is assured by the renormalizability of non-abelian gauge theories with spontaneous symmetry breaking, which was proved by 't Hooft and Veltman in refs. [26]–[28].

Further analysis on the construction of the Standard Model can be found in [24, 29, 30, 31] and references therein. The Feynman rules arising from the Lagrangian 2.56 in a general R_ξ gauge are presented in [32]. Feynman rules in the unitary gauge are also presented in [33]. Finally, Feynman rules in the 't Hooft gauge can be found in [31].

Chapter 3

Higgs boson phenomenology

In the previous chapter it was shown that the scalar sector in the Standard Model plays a fundamental rôle in the mass generation of the physical particles of the theory. The Higgs mechanism is also responsible for the appearance of a new massive scalar particle in the physical spectrum: the Higgs boson. In this chapter the phenomenological properties of the Higgs boson are briefly reviewed.

This chapter is organized as follows: in Section 3.1 the importance of the Higgs boson mass as a free parameter in the Standard Model is explained. Different constraints on its value are discussed. In Section 3.2 the different decay modes of the Higgs boson are studied. In Section 3.3, Higgs-boson production mechanisms are reviewed, with emphasis in production at hadron colliders. Finally, in Section 3.4, the the different SM Higgs boson search strategies at the Fermilab TEVATRON and the CERN LHC are analysed.

3.1 SM Higgs Mass

In Section 2.3 it was shown that, besides the physical particles masses and the electroweak couplings, there are two more parameters in the Standard Model. These parameters are related to the Higgs sector of the theory:

$$\mu \rightarrow \text{Related to Higgs boson mass}$$

$$\lambda \rightarrow \text{Related to Higgs field self} - \text{coupling}.$$

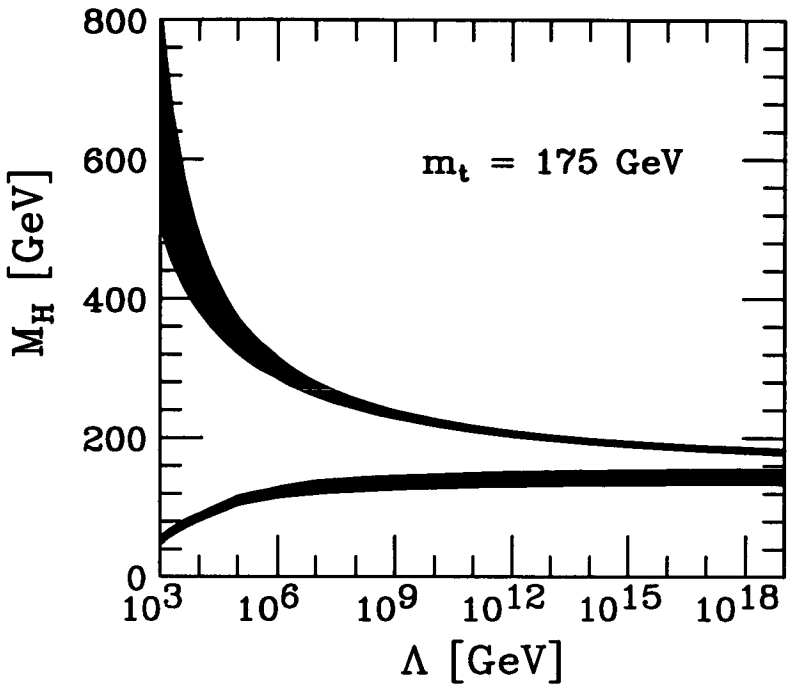

Figure 3.1: Upper and lower Higgs mass limits according to ref. [34]. The shaded regions denote theoretical uncertainties in cut-off and scale choices.

One can always choose as physical parameters the Higgs boson mass and the vacuum expectation value:

$$M_H = \sqrt{2}\,\mu \quad \text{and} \quad v = \frac{2\mu}{\sqrt{\lambda}}. \tag{3.1}$$

The vacuum expectation value v can be measured from the gauge boson mass, and it is also related to the Fermi constant G_μ:

$$v^2 = \frac{1}{\sqrt{2}\,G_\mu}.$$

On the other hand, the parameter λ is only related to the Higgs potential. Consequently, a measured value for M_H will only be available after Higgs-boson detection. As the Higgs boson has not been observed yet, no precise value for its mass is known, and all the properties of the Higgs sector are known as a function of M_H. It is worth noting that, despite the lack of direct M_H measurements, different constraints have been imposed on its value.

An important constraint on the Higgs boson mass is determined by the relation between M_H and the energy scale Λ at which the Standard Model validity breaks down.

This relation has been reviewed in ref. [34], and is shown in in figure 3.1, for a top-quark mass of $m_t = 175\,\text{GeV}$. Upper and lower limits on the Higgs mass can be derived requiring that the scalar potential self-coupling constant remains positive and finite up to the energy scale Λ. If $M_H \sim 1\,\text{TeV}$, the self-coupling constant becomes unphysically large and new physics must appear at the scale $\Lambda \sim 1\,\text{TeV}$. This constraint imposes a perturbative upper limit on M_H, see ref. [35], while lattice calculations provide a non-perturbative upper limit [36]–[39]. On the other hand, stability requirements provide a lower limit for the Higgs mass. For M_H very small, the scalar potential minima configurations become unstable, as studied in refs [40]–[42], and new physics must appear below $\Lambda \sim M_H$. Recent research on the lower mass limit of the Higgs mass as a function of Λ, see ref. [43], using non-perturbative lattice simulations suggests that the vacuum instability for a very light Higgs does not exist. What's more, it is argued that the lower mass limit is regulator dependent.

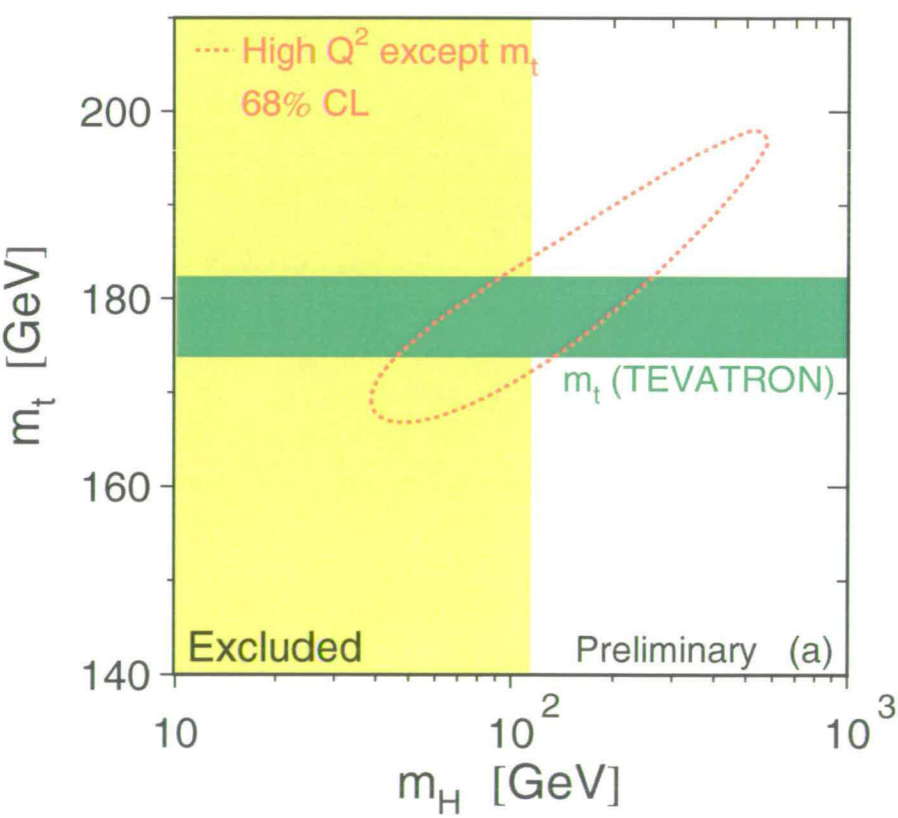

Figure 3.2: Comparison of direct and indirect measurements for m_t and M_H. The 68% CL fit countour is also shown. Plot published by [12].

The above mentioned constraints are obtained through theoretical considerations.

Experimental constraints have been obtained, too. A set of experimental constraints on the Standard Model Higgs-boson mass is obtained regularly by the LEP Electroweak Working Group (LEP EWWG). The LEP EWWG combines precision electroweak results from the four LEP experiments to produce the best LEP averages. These averages are used to analyse the validity of the Standard Model and other theories. On the other hand, assuming the Standard Model to be valid, different parameters can be fitted and compared with direct measurements. This is a powerful test of the Standard Model validity. For instance, figure 3.2[12] shows a comparison between the direct and indirect measurement of the top quark mass m_t. The vertical band shows the excluded Higgs mass range obtained by direct searches with 95% CL, see ref. [14]. The horizontal band shows the m_t direct measurement and the $\pm 1\sigma$ width. Finally, the dashed line shows the 68% CL countour in m_t and M_H for a fit to all data except the direct m_t measurement.

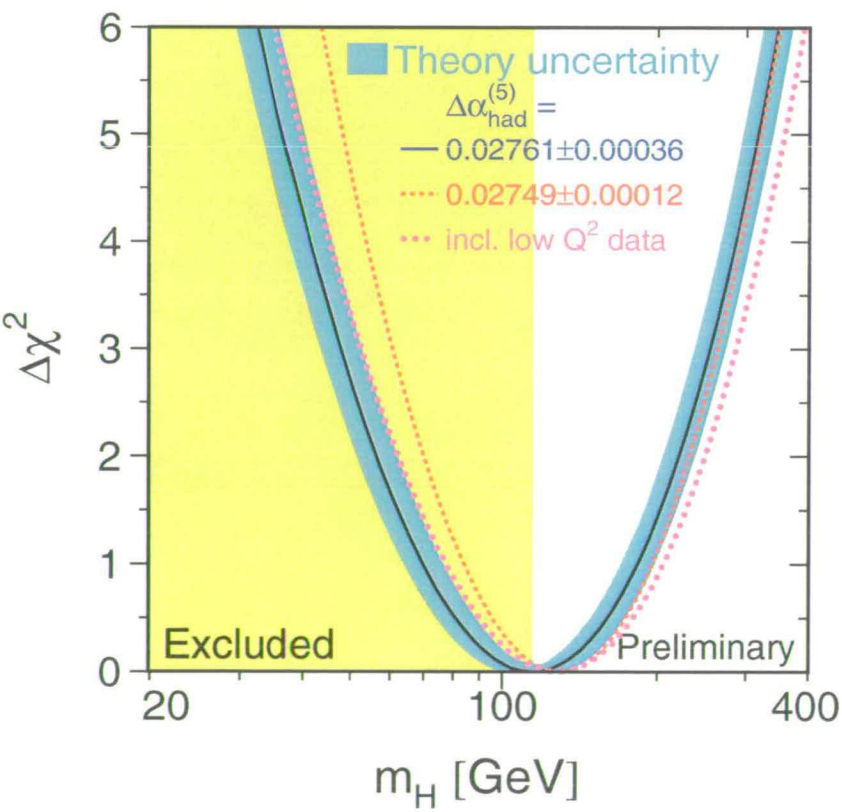

Figure 3.3: $\Delta\chi^2$ corresponding to the fit of the Higgs boson mass to the Standard Model electroweak parameters. The blue band represents the theoretical uncertainties, as explained in the text. Plot published by [12].

The most precise M_H constraints are obtained when the Higgs mass is fitted to all the available direct precision measurements. The results of this fit is shown in figure 3.3, sometimes known as the *blueband plot*[12]. The minimum χ^2 of the fit is $\chi^2_{\rm min}/df = 15.8/13$. Figure 3.3 shows the variation $\Delta\chi^2 = \chi^2 - \chi^2_{\rm min}$ as a function of the Higgs-boson mass. The vertical band shows the direct experimental lower mass limit, obtained combining the four LEP experiments, ALEPH, DELPHI, L3 and OPAL, see ref. [14]:

$$114.4\,\text{GeV} < M_H \quad (95\%\,\text{CL})\,.$$

The preferred value for M_H is

$$M_H = 114^{+69}_{-45}\,\text{GeV}$$

and an upper limit for the Higgs mass can be obtained,

$$M_H < 260\,\text{GeV} \quad (95\%\,\text{CL})\,.$$

The blueband in this plot corresponds to the theoretical uncertainties corresponding to higher order corrections. The solid line uses the value

$$\Delta\alpha^{(5)}_{\rm had}(M_Z) = 0.02761 \pm 0.00036$$

for the hadronic contribution from the light quarks to the photon vacuum polarization.

3.2 SM Higgs Decay

The Higgs boson couples to the rest of the particles of the Standard Model with a coupling constant proportional to the particle mass. Consequently, the Higgs boson tends to decay in the heaviest particle that is kinematically allowed. The coupling constants for the different Higgs boson interactions read,

$$\begin{aligned} g_{Hf\bar{f}} &= \tfrac{m_f}{v} & g_{HVV} &= \tfrac{2m_V^2}{v} & g_{HHVV} &= \tfrac{2M_V^2}{v^2} \\ g_{HHH} &= \tfrac{3m_H^2}{v} & g_{HHHH} &= \tfrac{3m_H^2}{v^2} = \tfrac{3}{2}\lambda\,. \end{aligned} \tag{3.2}$$

Figure 3.4, calculated in ref. [44], shows the total width of the Higgs boson as a function of its mass. As the Higgs boson becomes heavier, its width increases. It can be shown that if $M_H \sim 1.4\,\text{TeV}$ the Higgs width becomes larger than its mass, and the physical interpretation of the Higgs boson as a particle becomes doubtful.

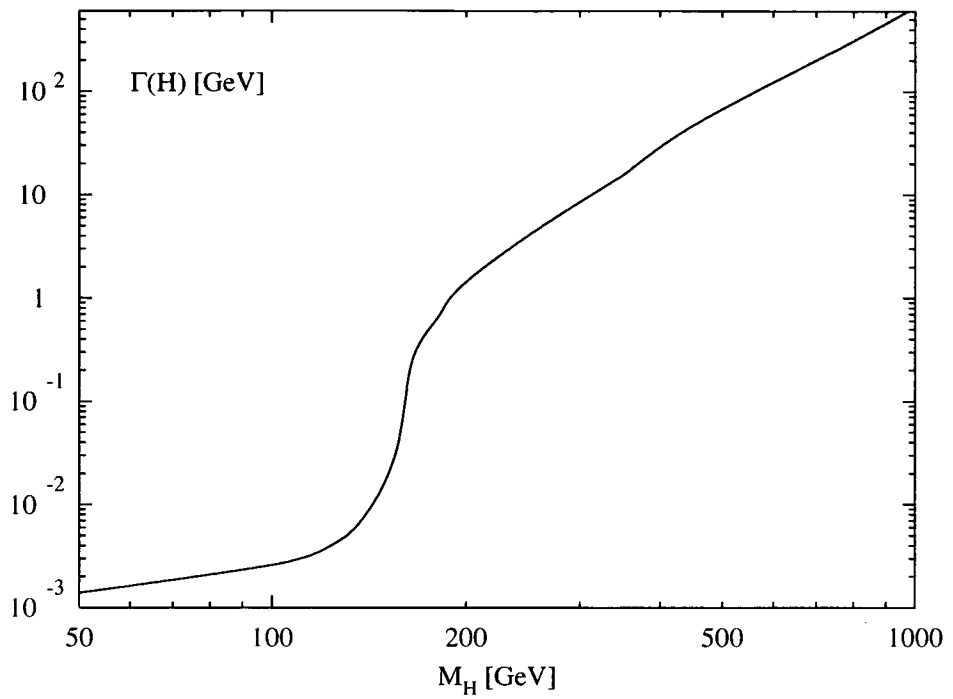

Figure 3.4: Total Higgs boson width vs. M_H. Plot taken from ref. [44].

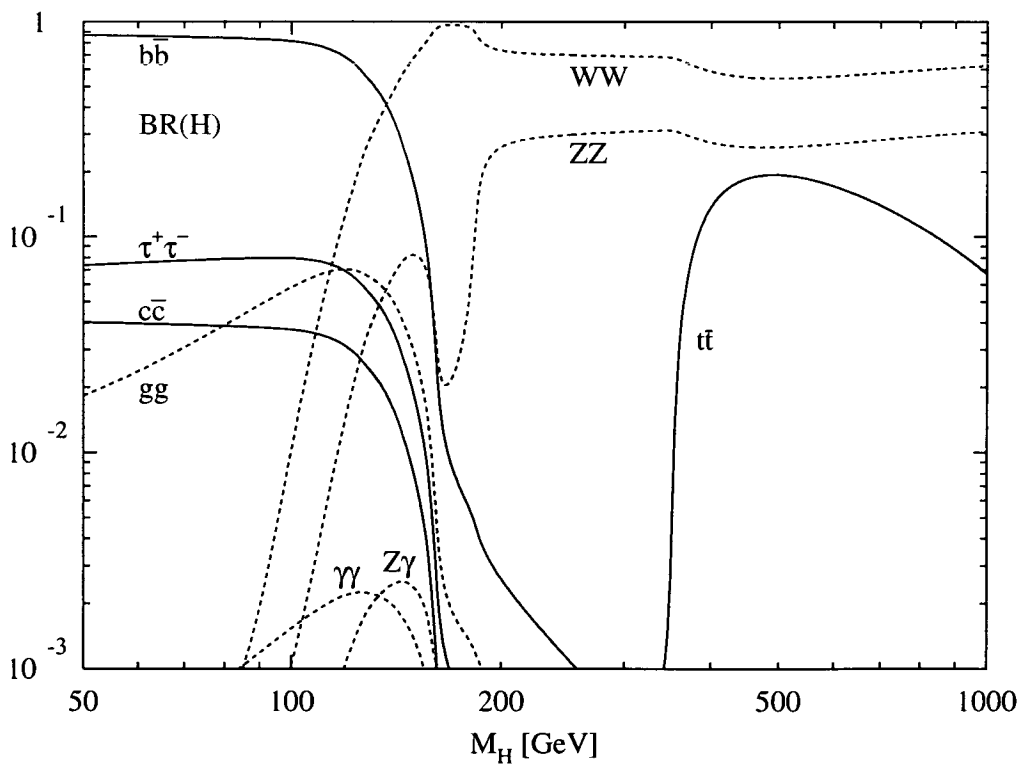

Figure 3.5: Higgs boson branching ratio vs. M_H. Figure taken from ref. [44].

As mentioned above, if kinematically possible, the Higgs boson always decays into the heaviest possible particle. This is clearly shown in figure 3.5, which depicts the branching ratio of the Higgs boson into different decay channels as a function of its mass. It can be seen that a Higgs boson of mass $M_H \lesssim 140\,\text{GeV}$ decays mainly into fermions, predominantly into a $b\bar{b}$ pair. For intermediate masses Higgs decay into a pair of photons or gluons is also significant. These decay modes are loop induced processes, where the Higgs boson couples, via a heavy fermion loop, to a $\gamma\gamma$ or gg pair. When $140\,\text{GeV} \lesssim M_H$, the decay channel into gauge bosons opens up. If the Higgs mass is less than $2M_W$ then the Higgs decays mainly into an on-shell and an off-shell W-boson. When the Higgs mass reaches the threshold $2M_W$, the decay into two on-shell W-bosons opens up. When this happens the branching ratio into an on-shell and an off-shell Z-bosons has an abrupt decrease. When $2M_Z \leq M_H$, the decay into two on-shell Z-bosons becomes important. For larger Higgs boson masses the decay into a pair of on-shell vector bosons is dominant, even after the $t\bar{t}$ channel opens up.

3.3 SM Higgs Production

In this section the different Higgs production mechanisms in the Standard Model are discussed. First, the production mechanisms at an e^+e^- collider are briefly explained. Then, production at hadron colliders, the Fermilab TEVATRON and the CERN LHC, are discussed in more detail.

Figure 3.6 show the most important Higgs boson production channels at an e^+e^- collider. The cross section for production in association with a vector boson

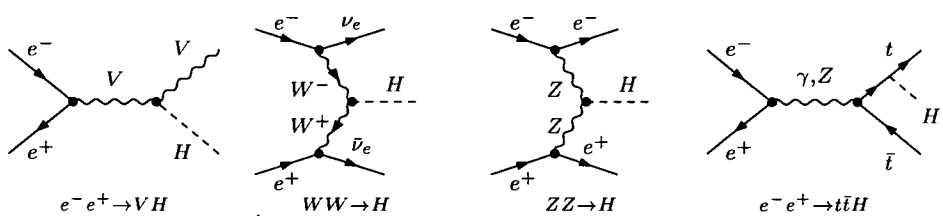

Figure 3.6: Higgs production mechanisms at an e^+e^- collider.

$e^-e^+ \to ZH$, also known as "Higgs-strahlung", scales as $1/s$, and it dominates the low energy region. Z-boson associated production was the main Higgs boson produc-

tion channel at the CERN LEP collider. Vector boson fusion, $VV \to H$, is another important production mechanism at e^+e^- colliders. Existing calculations show that the cross section for W-boson fusion processes increases logarithmically with s, so this production process is of great importance at the high energy regime. Z-boson fusion cross section is one order of magnitude smaller than for the W-fusion channel. Finally, at very high energy e^+e^- collisions, $\sqrt{s} \sim 1\,\text{TeV}$, Higgs boson production in association with a $t\bar{t}$ quark pair becomes significant.

In figure 3.7 the parton tree level Feynman diagrams for the most important Higgs boson production processes at hadron colliders are shown. At high energy colliders the

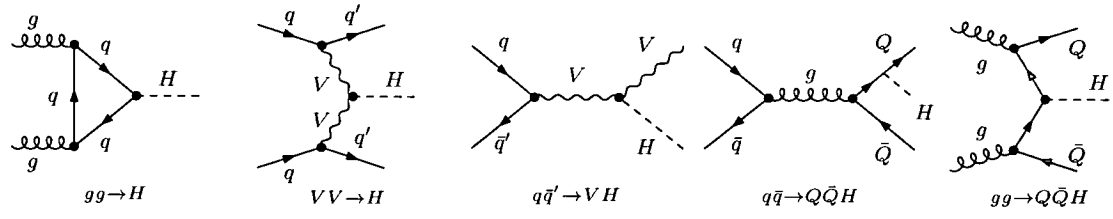

Figure 3.7: Tree level, parton Feynman diagrams for hadronic Higgs production processes.

production process with the highest cross section, due to the high gluon luminosity, is gluon fusion production $gg \to H$. Note that the Higgs boson is produced via a heavy quark loop, typically t- or b-quarks. A Higgs boson can also be produced via vector-boson fusion $VV \to H$: two quarks in the initial state radiate a vector boson pair that annihilates into a Higgs boson. Higgs boson production is also possible via associated production with $W^{\pm}$- or Z-bosons: two quarks annihilate into a vector boson that then radiates a Higgs boson. Finally, an important production mechanism is associated production with a heavy quark-antiquark pair. In this process a Higgs boson is radiated off heavy quarks in the final state.

The total Standard Model Higgs production cross section at the CERN LHC and the Fermilab TEVATRON are shown in figures 3.8 and 3.9, respectively. In these figures it can be seen that the dominant production mechanism at these hadron colliders is gluon fusion $gg \to H$, with a cross section of approx. 10pb for a Higgs-boson of mass $M_H = 200\,\text{GeV}$ at the CERN LHC and 1 pb for $M_H = 100\,\text{GeV}$ at the Fermilab

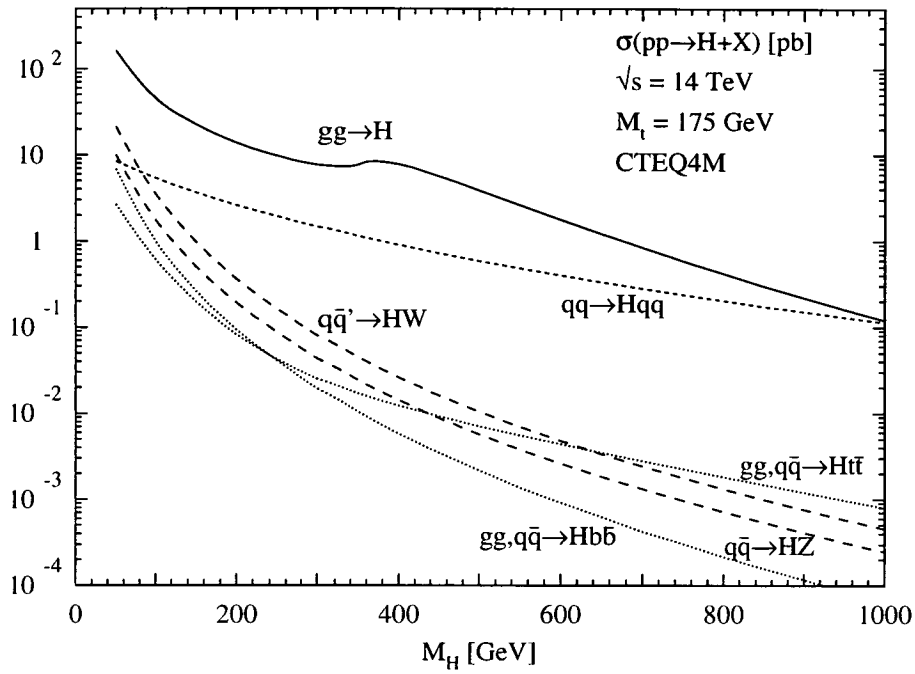

Figure 3.8: CERN LHC Higgs boson production cross sections in pb, taken from ref. [45].

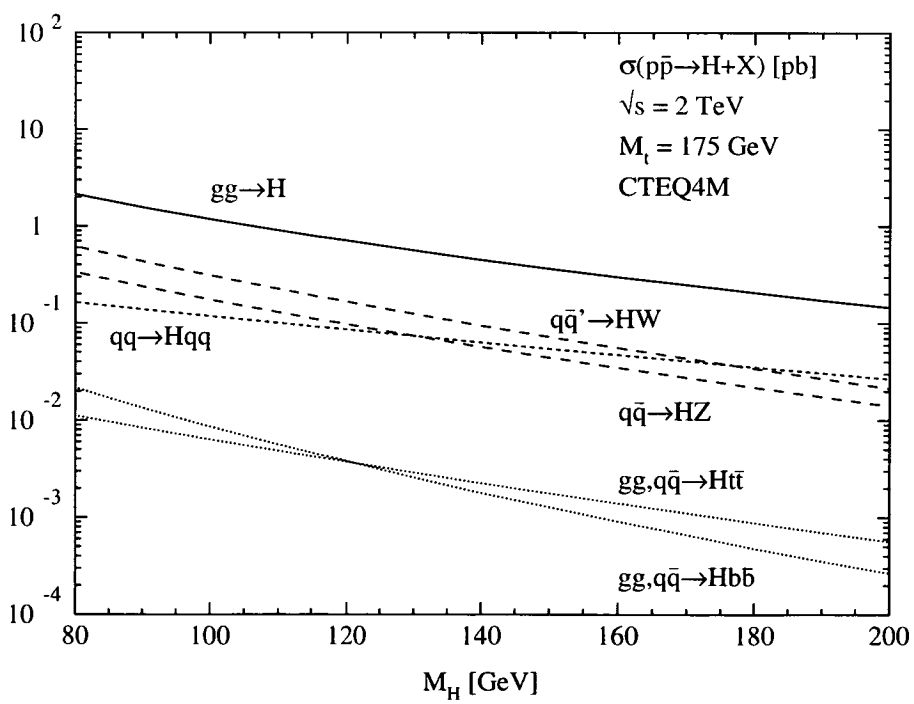

Figure 3.9: Fermilab TEVATRON Higgs-boson production cross sections in pb, taken from ref. [46].

TEVATRON.

At the LHC vector boson fusion, process $qq \to qqH$, has a cross section two orders of magnitude smaller than gluon fusion for a light Higgs boson, but it becomes the dominant production mechanism if $M_H \sim 1\,\text{TeV}$. Vector boson associated production cross sections at the LHC, $q\bar{q}' \to HW$ and $q\bar{q} \to HZ$, are of the same order as vector boson fusion for a light Higgs, but become less than two orders of magnitude smaller for a heavy Higgs. All theses cross sections are shown to next-to-leading order in α_s. Gluon fusion is also known at NNLO but only in the heavy-top-quark limit. Production in association with heavy quarks $gg, q\bar{q} \to Hb\bar{b}$ and $gg, q\bar{q} \to Ht\bar{t}$ are also shown, but these cross sections do not include the NLO corrections from [47, 48].

At the TEVATRON the process with the second largest cross section is production in association with a vector boson, $q\bar{q}' \to HW$ and $q\bar{q} \to HZ$. This cross section is one order of magnitude smaller than gluon fusion production cross section. Of approximately the same order is the cross section for vector boson fusion production, $qq \to qqH$. Less than one order of magnitude smaller is the cross section for production in association with heavy quark-antiquark pairs $gg, q\bar{q} \to Hb\bar{b}$ and $gg, q\bar{q} \to Ht\bar{t}$. All these cross sections, except for production in association with $b\bar{b}$ pairs are shown to next-to-leading order.

3.4 Higgs Boson Searches at Hadron Colliders

The search for the Higgs boson is the main objective of present and future particle accelerators. Currently, the Higgs boson is being searched for at the upgraded Tevatron proton-antiproton collider, at Fermilab. New searches will begin at the CERN Large Hadron Collider (LHC) in the near future. Consequently, it is important to understand and predict Higgs boson behaviour at hadron colliders. In this section the different Higgs boson production mechanisms at the Tevatron and the CERN LHC are reviewed. The Higgs boson different decay channels are studied and the detection strategies at these hadron colliders are discussed.

3.4.1 Higgs Boson Searches at the Fermilab TEVATRON

The Fermilab TEVATRON Higgs boson searches cover the mass region $100\,\text{GeV} \lesssim M_H \lesssim 200\,\text{GeV}$. The most important production mechanisms are, depending on the Higgs mass, vector boson associated production and gluon fusion. For a detailed analysis of Higgs boson searches see for example refs. [49] and [50].

If $M_H \lesssim 135\,\text{GeV}$ the gluon fusion channel is not accessible to the TEVATRON searches. The reason for this is that, although gluon fusion is the production process with the highest cross section, the Higgs boson decays with branching ratio $\sim 90\%$ into a $b\bar{b}$ quark pair, and the QCD background is orders of magnitude larger than the signal. Consequently, the most important discovery channel for a light Standard Model Higgs boson is vector boson associated production, where the vector boson decays leptonically, and the Higgs decays into a $b\bar{b}$-pair. The final states in these processes, $l\nu b\bar{b}$, $\nu\nu b\bar{b}$, $llb\bar{b}$, can be effectively tagged at the TEVATRON detectors through high p_T leptons or high missing transverse energy E_T.

If the Higgs boson mass is larger than 135 GeV, the decay mode into a W^+W^--pair opens up, and the gluon fusion channel becomes available to TEVATRON searches. Taking also into account vector boson associated production, the final states available for Higgs searches are WW, ZWW and WWW. The most important ingredient in these search channels is the strong angular correlation of the W-boson pair coming from the Higgs decay. Final states which can be detected at the different experiments include $l^{\pm}l^{\pm}jj$, $l^-l^+\nu\bar{\nu}$ and $l^{\pm}l^{\pm}l^{\pm}$.

Figure 3.10 shows the integrated luminosity per experiment required to either exclude a Higgs boson at 95% CL, or discover it at 3σ or 5σ statistical significance, as a function of M_H, in the range 100 GeV–140 GeV. This figure includes the results from ref. [49] and the updated analysis of ref. [50].

3.4.2 Higgs Boson Searches at the CERN LHC

The ATLAS experiment at the CERN LHC is designed to efficiently search for a Standard Model Higgs boson with masses as low as 80 GeV and as large as 1000 GeV. The different search strategies are chosen according to signal rate and signal-to-background ratio. Consequently, the search channel used depends strongly on the mass of the Higgs. In this section a brief summary of the results of ref. [15] are presented.

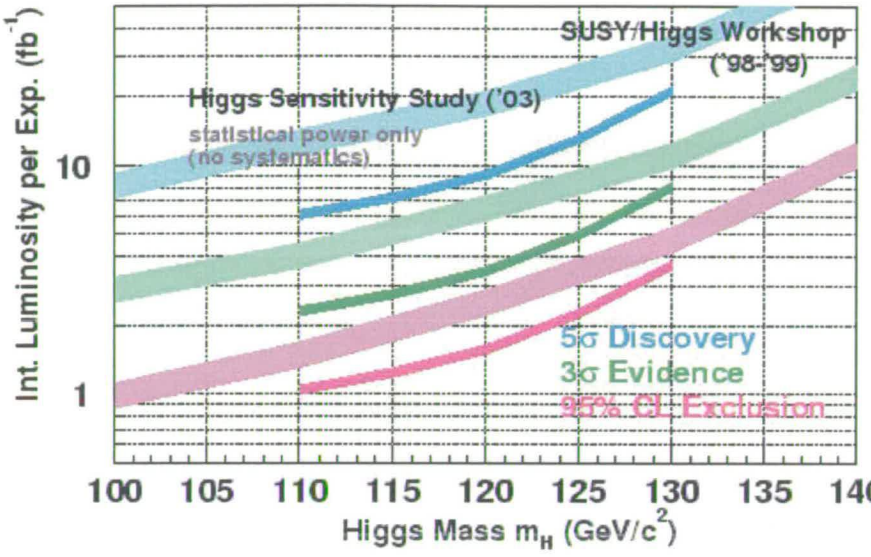

Figure 3.10: Required luminosity for Higgs boson detection with 3σ or 5σ statistical significance, or exclusion with 95 % CL, at Fermilab TEVATRON. Taken from ref. [50]

$\mathbf{H \to \gamma\gamma}$

This Higgs decay mode is important as discovery tool in the mass range 100 GeV – 150 GeV. Depending on excellent energy and angular resolution, a narrow mass peak can be observed. Excellent particle identification is also important to reject large QCD jet background and the resonant production of $Z \to ee$. The most important Higgs production processes involved are: direct production through gluon fusion, production in association with vector-boson or $t\bar{t}$ pairs, and production in association with QCD jets.

A similar detection channel, $H \to Z\gamma$, has been found to be of importance in the mass region 100 GeV – 160 GeV.

$\mathbf{H \to b\bar{b}}$

It has been shown in Section 3.2 that the branching ratio of a Higgs boson with mass $M_H < 2M_W$ decaying into $b\bar{b}$ pairs is of the order of 90%. Similarly to the Fermilab TEVATRON, QCD background to $b\bar{b}$ pair production is huge. The only way to detect this Higgs decay mode is to use associated production with a W-boson or with a $t\bar{t}$

pair, and trigger on the leptons from the W-boson leptonic decays or the semileptonic decays from the top quark. Once the Higgs event is identified, a mass peak can be measured using the invariant mass spectrum of the b-jets.

Associated production with a Z-boson is not considered in the ATLAS analysis, as the production cross section is almost one order of magnitude smaller than in the case of WH-associated production.

$\mathbf{H \to ZZ^* \to 4l}$

This detection channel is relevant for a Higgs boson with mass $120\,\text{GeV} \lesssim M_H \lesssim 2M_Z$. In the region $150\,\text{GeV} \lesssim M_H \lesssim 180\,\text{GeV}$, the branching ratio to ZZ^* has a pronounced dip, due to the opening of the decay channel $H \to WW$. It has been argued that a 5σ Higgs detection is possible with $30\,\text{fb}^{-1}$ of integrated luminosity, while $100\,\text{fb}^{-1}$ are needed for more than 5σ statistical significance with the ZZ^* channel.

$\mathbf{H \to WW^{(*)} \to \bar{l}\nu l'\bar{\nu}'}$

If the Higgs boson mass is close to 170 GeV then the decay into ZZ^* pairs is suppressed in favour of decay into WW^*, with a branching ratio almost two orders of magnitude larger than the neutral gauge boson pair decay. Using the method suggested in [108] a statistical significance of more than 5σ can be obtained with $30\,\text{fb}^{-1}$ of integrated luminosity. Information on the mass of the Higgs boson can also be obtained using the transverse mass distribution.

It is important to know that, in this search channel, the presence of a Higgs boson will not be detected as a mass peak in a mass distribution, but as an excess of events over the expected background. The method of ref. [108] to study this channel is explained in detail in Chapter 5.

$\mathbf{WH \to l\nu l\nu l\nu}$

Associated production with W-bosons with subsequent Higgs boson decay into a W-boson pair, followed by leptonic decays of the three vector bosons, represent an important possibility for enhancing Higgs boson detection in the mass range $150\,\text{GeV} \lesssim M_H \lesssim 190\,\text{GeV}$. Similarly, the search channel $WH \to WWW \to lljj$ may be considered, which is less important than the leptonic channel as the QCD back-

ground becomes more important. As explained in the previous section, this is also an important Higgs search tool at the Fermilab TEVATRON.

$\mathbf{H \to ZZ \to 4l}$ or $\mathbf{H \to ZZ \to l\nu l\nu}$

For $2M_Z \lesssim M_H \lesssim 700\,\text{GeV}$ the detection channel $H \to ZZ$ with the Z-boson pair decaying into 4 charged leptons is the most important search channel. What's more, due to the fact that for this process signal cross section is larger than background cross section, and that the lepton momenta are large enough for easy detection, this is the most reliable discovery channel for a Standard Model Higgs boson at the LHC. The discovery potential is only determined by the available luminosity.

Heavy Higgs Boson

The four lepton channel could be used efficiently up to $M_H \sim 800\,\text{GeV}$. For a heavier Higgs boson the channels $H \to ZZ \to ll\nu\nu$, $H \to ZZ \to lljj$ and $H \to WW \to l\nu jj$ would be used to probe the 1 TeV mass region.

Weak Vector Boson Fusion

Recently, a new discovery strategy for a Standard Model Higgs boson has been proposed in refs. [51]–[55]. This method assumes that the Higgs boson is produced in a vector boson fusion (VBF) process. VBF cross section is approx. 10% of the gluon fusion process cross section in the low Higgs mass region. For a heavy Higgs boson, gluon fusion and VBF cross sections are of the same order of magnitude. VBF processes are characterized by the presence of two jets in the forward-backward direction, originating from the initial quarks that emitted the gauge bosons. In addition, central jet activity is suppressed. Jet tagging in the forward-backward direction and a jet veto in the central region are very effective methods for increasing the signal-to-background ratio.

Total Signal Significance

The sensitivity for each detection channel discussed above, is shown in figures 3.11 and 3.12, for the ATLAS and CMS experiments, respectively. These figures have been taken from refs. [15] and [56]. Units of Signal/$\sqrt{\text{Backgr}}$ have been used, and an integrated luminosity of $30\,\text{fb}^{-1}$ is assumed. No K-factors have been included, as

not all the corrections for all the background processes were known at the time the signal significance studies were done. The total sensitivity for the Higgs mass range $80\,\text{GeV} \lesssim M_H \lesssim 1\,\text{TeV}$ is also shown. Clearly seen is the decrease in the $H \to ZZ^* \to 4l$ channel, caused by the opening of the $H \to WW$ decay mode. The possibility of detecting a Higgs boson using the search channel $H \to WW \to \bar{l}\nu\, l'\bar{\nu}'$ with very high statistical significance, is the main motivation to the calculation of the gluon induced contribution to off-shell W-boson pair production at hadron colliders, cf. Chapter 5.

To conclude, a 5σ signal significance is expected for Higgs-boson detection at the CERN LHC with an integrated luminosity of $30\,\text{fb}^{-1}$. This is equivalent to one year of running at the low luminosity regime. If the Standard Model Higgs boson exists, it will be detected at the LHC.

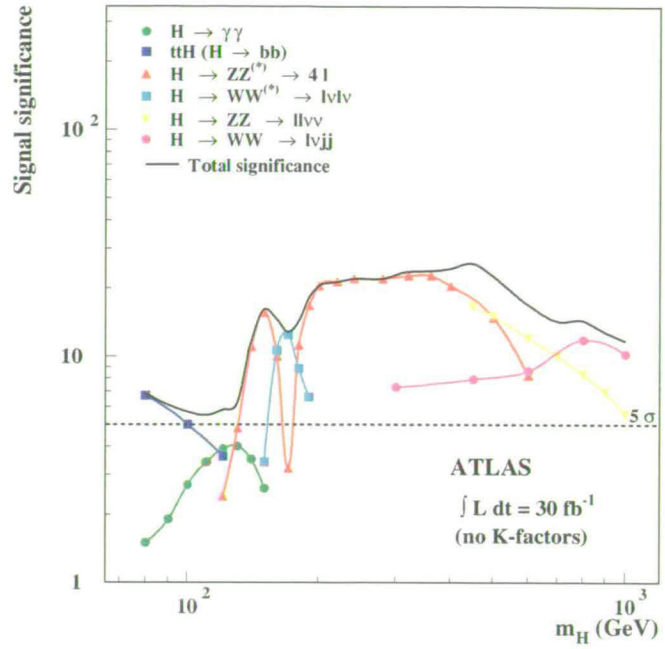

Figure 3.11: ATLAS experiment Higgs signal significance for an integrated luminosity of $30\,\mathrm{fb}^{-1}$, as a function of the Higgs boson mass. Taken from ref. [15].

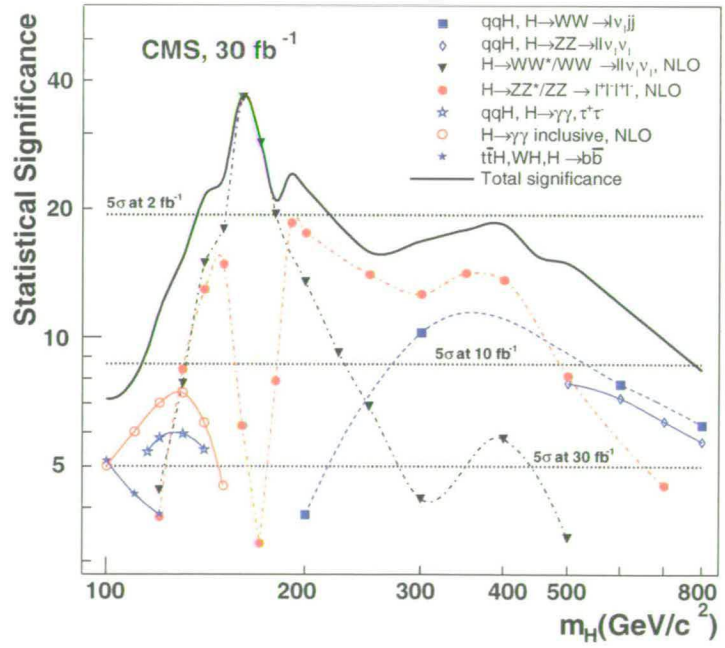

Figure 3.12: CMS experiment Higgs signal significance for an integrated luminosity of $30\,\mathrm{fb}^{-1}$, as a function of the Higgs boson mass. Taken from ref. [56].

Chapter 4

Vector Boson Associated Production

In this chapter the calculation of the electroweak $\mathcal{O}(\alpha)$ corrections to the processes $p\bar{p}/pp \to W^+H + X$ and $p\bar{p}/pp \to ZH + X$ is presented. The cross-section prediction for associated WH and ZH production at the Tevatron and at the LHC, including the NLO electroweak and QCD corrections, is updated and the residual theoretical uncertainty due to scale variation and the parton distribution functions is quantified.

This chapter is organized as follows. In Section 4.2 the computation of the $\mathcal{O}(\alpha)$ electroweak corrections is outlined. The calculation of the hadronic cross section and the treatment of the initial-state mass singularities are described in Section 4.3. In Section 4.4 numerical results for associated WH and ZH production at the Tevatron and at the LHC are presented. In Section 4.5 the $\mathcal{O}(\alpha)$ electroweak corrections are combined with the recently published[57] next-to-next-to-leading order QCD corrections. Finally, the conclusions are given in Section 4.6.

4.1 Introduction

The search for the Higgs boson continues at the upgraded proton–antiproton collider Tevatron [49] with a centre-of-mass (CM) energy of 1.96 TeV, followed in the near future by the proton–proton collider LHC [15] with 14 TeV CM energy. Various channels can be exploited at hadron colliders to search for a Higgs boson, as explained in Chapter

3. At the Tevatron, Higgs-boson production in association with W or Z bosons,

$$p\bar{p} \to WH + X \quad \text{and} \quad p\bar{p} \to ZH + X, \tag{4.1}$$

is the most promising discovery channel for a SM Higgs particle with a mass below about 135 GeV, where decays into $b\bar{b}$ final states are dominant [49].

At leading order, the production of a Higgs boson in association with a vector boson, $p\bar{p} \to VH + X, (V = W, Z)$ proceeds through $q\bar{q}$ annihilation [60],

$$q\bar{q}' \to V^* \to V + H. \tag{4.2}$$

The next-to-leading order (NLO) QCD corrections coincide with those for the Drell-Yan process and increase the cross section by about 30% [61]. Beyond NLO, the QCD corrections for VH production differ from those for the Drell-Yan process by contributions where the Higgs boson couples to a heavy fermion loop. The impact of these additional terms is, however, expected to be small in general [62], and NNLO QCD corrections should not increase the VH cross section at the Tevatron significantly, similar to the Drell-Yan cross section [63]. In Sect. 4.5 the recent NNLO QCD calculation [57] and its combination with the electroweak corrected cross section are discussed in detail. As described in in Sections 4.4 and 4.5, the renormalization and factorization scale dependence is reduced to about 10% at $\mathcal{O}(\alpha_s)$, while the uncertainty due to the parton luminosity is less than about 5%. Inclusion of NNLO QCD results further reduces these uncertainties. At this level of accuracy, the electroweak $\mathcal{O}(\alpha)$ corrections become significant and need to be included to further improve the theoretical prediction. Moreover, the QCD uncertainties may be reduced by forming the ratios of the associated Higgs-production cross section with the corresponding Drell–Yan-like W- and Z-boson production channels, i.e. by inspecting $\sigma_{p\bar{p}\to VH+X}/\sigma_{p\bar{p}\to V+X}$. In these ratios, higher-order electroweak effects should be significant. For the Drell–Yan-like W- and Z-boson production the electroweak corrections have been calculated in Refs. [64, 65] and [66], respectively. The electroweak $\mathcal{O}(\alpha)$ corrections to associated ZH production at e^+e^- colliders have been presented in Ref. [67].

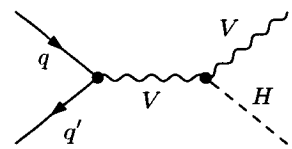

Figure 4.1: Lowest-order diagram for $q\bar{q}' \to V^* \to VH$ $(V = W, Z)$.

4.2 The Parton Cross Section

4.2.1 Conventions and lowest-order Cross Section

The parton process

$$q(p_q, \tau_q) + \bar{q}'(p_{\bar{q}'}, \tau_{\bar{q}'}) \;\to\; V(p_V, \lambda_V) + H(p_H) \;\; [+\gamma(k, \lambda)], \tag{4.3}$$

where $V = W^+, Z$, is considered. The light up- and down-type quarks are denoted by q and q', where $q = \mathrm{u}, \mathrm{c}$ and $q' = \mathrm{d}, \mathrm{s}$ for W^+H production and $q = q' = \mathrm{u}, \mathrm{d}, \mathrm{s}, \mathrm{c}, \mathrm{b}$ for ZH production. The variables within parentheses refer to the momenta and helicities of the respective particles. The Mandelstam variables are defined by

$$\hat{s} = (p_q + p_{\bar{q}'})^2, \quad \hat{t} = (p_q - p_V)^2, \quad \hat{u} = (p_{\bar{q}'} - p_V)^2, \quad s_{VH} = (p_H + p_V)^2. \tag{4.4}$$

For the non-radiative processes $q\bar{q}' \to VH$, $\hat{s} = s_{VH}$. The fermion masses m_q, $m_{\bar{q}'}$ are neglected whenever possible, i.e. these masses are only kept as regulators in the logarithmic mass singularities originating from collinear photon emission or exchange. As a consequence, the fermion helicities τ_q and $\tau_{\bar{q}'}$ are conserved in lowest order and in the virtual one-loop corrections, i.e. the matrix elements vanish unless $\tau_q = -\tau_{\bar{q}'} \equiv \tau = \pm 1/2$. For brevity the value of τ is sometimes indicated by its sign.

In lowest order only the Feynman diagram shown in Fig. 4.1 contributes to the scattering amplitude, and the corresponding Born matrix element is given by

$$\mathcal{M}_0^\tau = \frac{e^2 g_{qq'V}^\tau g_{VVH}}{\hat{s} - M_V^2}\, \bar{v}(p_{\bar{q}'})\, \not{\varepsilon}_V^*(\lambda_V)\, \omega_\tau u(p_q), \tag{4.5}$$

where $\varepsilon_V^*(\lambda_V)$ is the polarization vector of the boson V, $\bar{v}(p_{\bar{q}'})$ and $u(p_q)$ are the Dirac spinors of the quarks, and $\omega_\pm = \frac{1}{2}(1 \pm \gamma_5)$ denote the chirality projectors. The coupling factors are given by

$$g_{udW}^\tau = \frac{V_{ud}^*}{\sqrt{2} s_\mathrm{W}}\, \delta_{\tau -}, \qquad\qquad g_{WWH} = \frac{M_\mathrm{W}}{s_\mathrm{W}},$$

$$g^{\tau}_{qqZ} = -\frac{s_{\mathrm{W}}}{c_{\mathrm{W}}}Q_q + \frac{I^3_q}{c_{\mathrm{W}}s_{\mathrm{W}}}\delta_{\tau-}, \qquad g_{ZZH} = \frac{M_{\mathrm{Z}}}{c_{\mathrm{W}}s_{\mathrm{W}}}, \tag{4.6}$$

where Q_q and $I^3_q = \pm 1/2$ are the relative charge and the third component of the weak isospin of quark q, respectively. The weak mixing angle is fixed by the mass ratio $M_{\mathrm{W}}/M_{\mathrm{Z}}$, according to the on-shell condition $\sin^2\theta_W \equiv s^2_W = 1 - c^2_W = 1 - M^2_{\mathrm{W}}/M^2_{\mathrm{Z}}$. Note that the CKM matrix element for the ud transition, V_{ud}, appears only as global factor $|V_{ud}|^2$ in the cross section for WH production, since corrections to flavour mixing are negligible in the considered process. This means that the CKM matrix is set to unity in the relative corrections and, in particular, that the parameter V_{ud} need not be renormalized. The same procedure was already adopted for Drell–Yan-like W production [64, 65].

The differential lowest-order cross section is easily obtained by squaring the lowest-order matrix element $\mathcal{M}^{\tau}_0$ of (4.5),

$$\begin{aligned}\left(\frac{\mathrm{d}\hat{\sigma}_0}{\mathrm{d}\hat{\Omega}}\right) &= \frac{1}{12}\frac{1}{64\pi^2}\frac{\lambda^{1/2}(M_V^2, M_H^2, \hat{s})}{\hat{s}^2}\sum_{\text{spins}}|\mathcal{M}^{\tau}_0|^2 \\ &= \frac{\alpha^2}{48\, M_V^2\hat{s}^2}\, g^2_{VVH}\left((g^+_{qq'V})^2 + (g^-_{qq'V})^2\right)\lambda^{1/2}(M_V^2, M_H^2, \hat{s}) \\ &\quad \times \frac{(\hat{t} - M_V^2)(\hat{u} - M_V^2) + M_V^2\hat{s}}{(\hat{s} - M_V^2)^2},\end{aligned} \tag{4.7}$$

where the explicit factor $1/12$ results from the average over the quark spins and colours, and $\hat{\Omega}$ is the solid angle of the vector boson V in the parton CM frame. The total parton cross section is given by

$$\begin{aligned}\hat{\sigma}_0(q\bar{q}' \to VH) &= \frac{\alpha^2\pi}{72M_V^2\hat{s}^2}\, g^2_{VVH}\left((g^+_{qq'V})^2 + (g^-_{qq'V})^2\right) \\ &\quad \times \lambda^{1/2}(M_V^2, M_H^2, \hat{s})\,\frac{\lambda(M_V^2, M_H^2, \hat{s}) + 12M_V^2\hat{s}}{(\hat{s} - M_V^2)^2},\end{aligned} \tag{4.8}$$

where λ is the two-body phase space function $\lambda(x, y, z) = x^2 + y^2 + z^2 - 2xy - 2xz - 2yz$. The electromagnetic coupling $\alpha = e^2/(4\pi)$ can be set to different values according to different input-parameter schemes. It can be directly identified with the fine-structure constant $\alpha(0)$ or the running electromagnetic coupling $\alpha(k^2)$ at a high-energy scale k. For instance, it is possible to make use of the value of $\alpha(M^2_{\mathrm{Z}})$ that is obtained by analysing [68] the experimental ratio $R = \sigma(\mathrm{e^+e^-} \to \text{hadrons})/(\mathrm{e^+e^-} \to \mu^+\mu^-)$. These choices are called $\alpha(0)$-*scheme* and $\alpha(M^2_{\mathrm{Z}})$-*scheme*, respectively, in the following. Another value for α can be deduced from the Fermi constant G_μ, yielding $\alpha_{G_\mu} =$

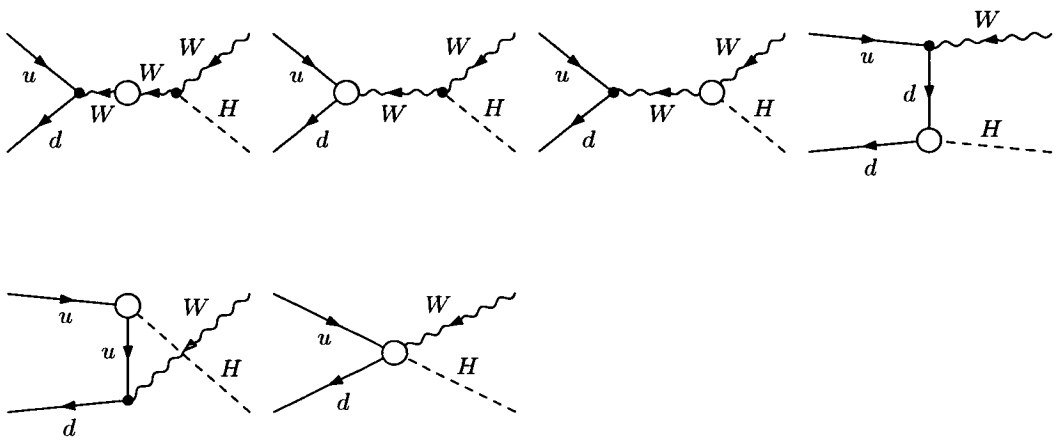

Figure 4.2: Contributions of different vertex functions to $u\bar{d} \to WH$.

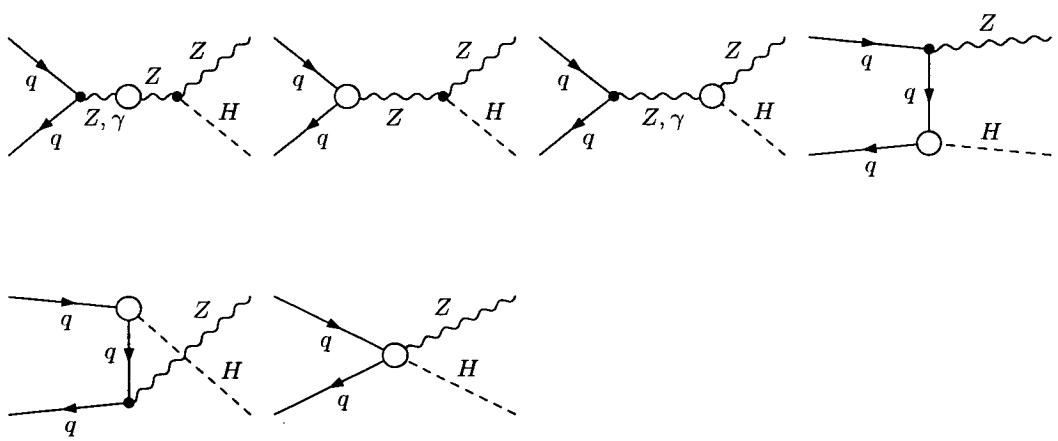

Figure 4.3: Contributions of different vertex functions to $q\bar{q} \to ZH$.

$\sqrt{2}G_\mu M_W^2 s_W^2/\pi$; this choice is referred to as G_μ-*scheme*. The differences between these schemes will become apparent in the discussion of the corresponding $\mathcal{O}(\alpha)$ corrections.

4.2.2 Virtual Corrections

One-loop Diagrams and Calculational Framework

The virtual corrections can be classified into self-energy, vertex, and box corrections. The generic contributions of the different vertex functions are shown in Figs. 4.2 and 4.3. Explicit results for the transverse parts of the WW, ZZ, and γZ self-energies (in the 't Hooft–Feynman gauge) can, e.g., be found in Ref. [31]. The diagrams for the

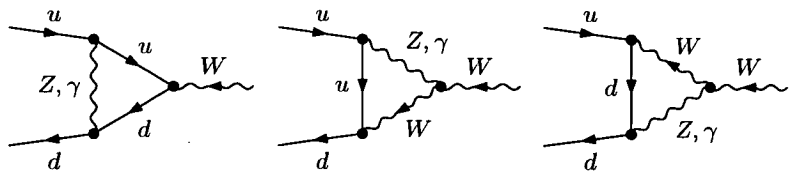

Figure 4.4: Diagrams for the corrections to the $ud\bar{W}$ vertex.

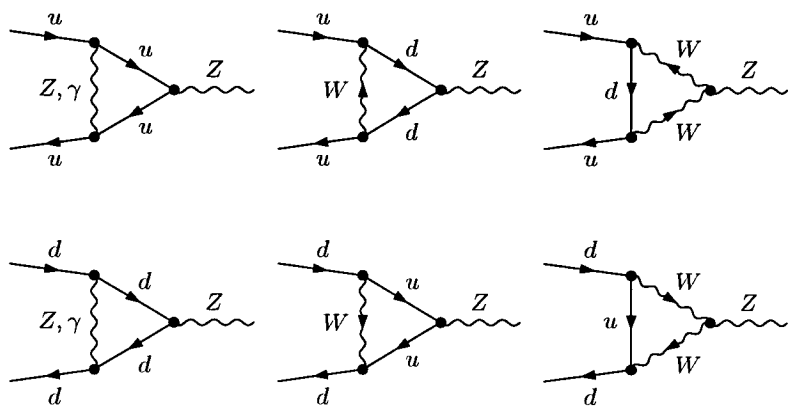

Figure 4.5: Diagrams for the corrections to the $q\bar{q}Z$ vertices.

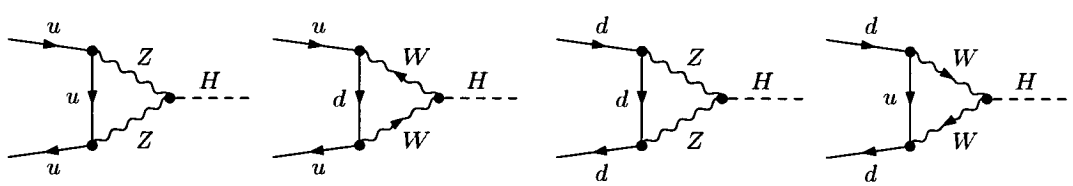

Figure 4.6: Diagrams for the corrections to the $q\bar{q}H$ vertices.

gauge-boson–fermion vertex corrections are shown in Figs. 4.4, 4.5, and 4.6.

The diagrams for the corrections to the WWH, ZZH, and γZH vertices are shown in Figs. 4.7 and 4.8. The box diagrams are depicted in Figs. 4.9 and 4.10, where φ is the would-be Goldstone partner of the W boson, χ is the Z-boson Goldstone partner and u_γ, u_Z and $u_\pm$ are the ghost fields corresponding to γ, Z and $W^\pm$ respectively.

The actual calculation of the one-loop diagrams has been carried out in the 't Hooft–Feynman gauge using standard techniques. The Feynman graphs have been generated with *FeynArts* [70, 71] and are evaluated in two completely independent ways, leading

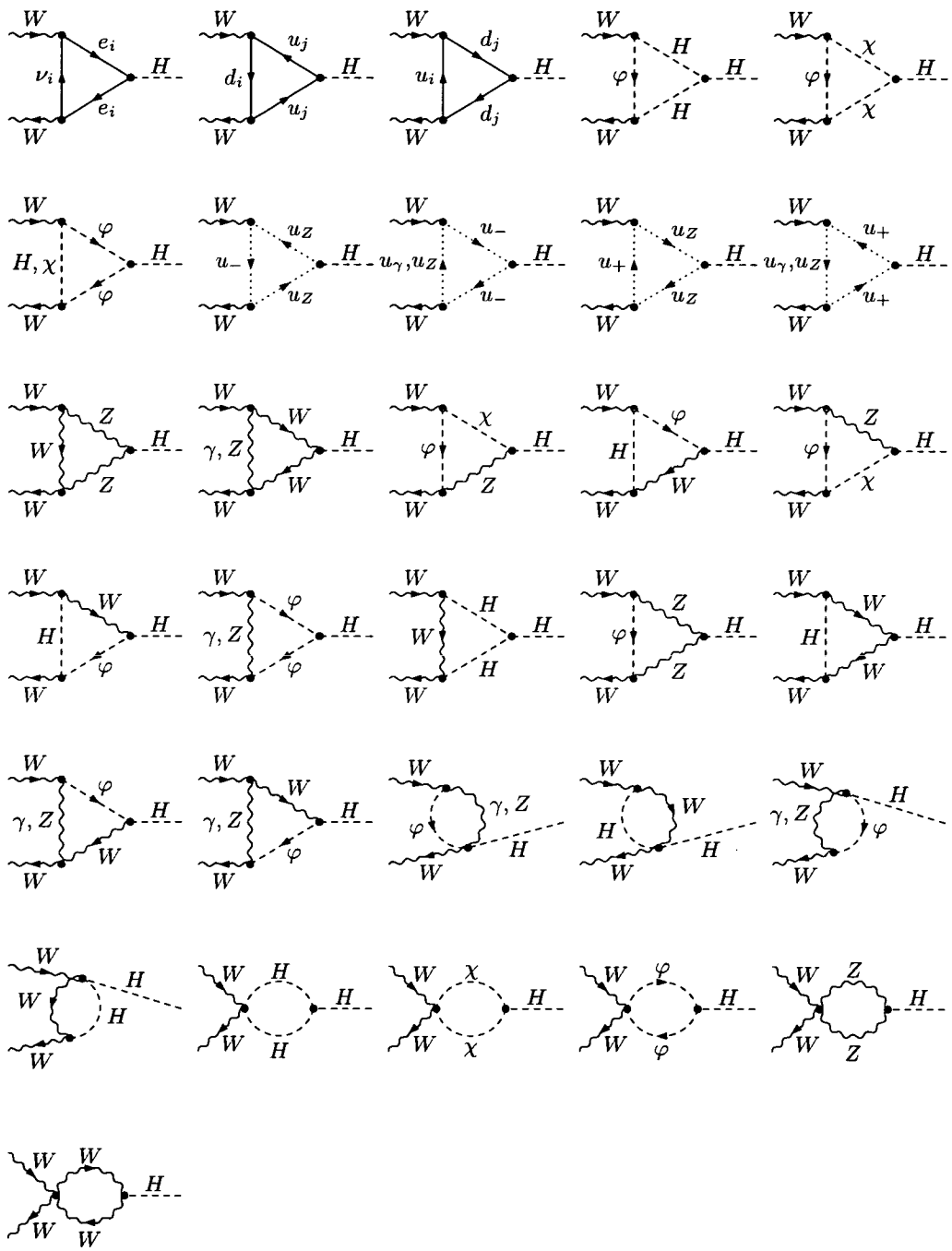

Figure 4.7: Diagrams for the corrections to the WWH vertex.

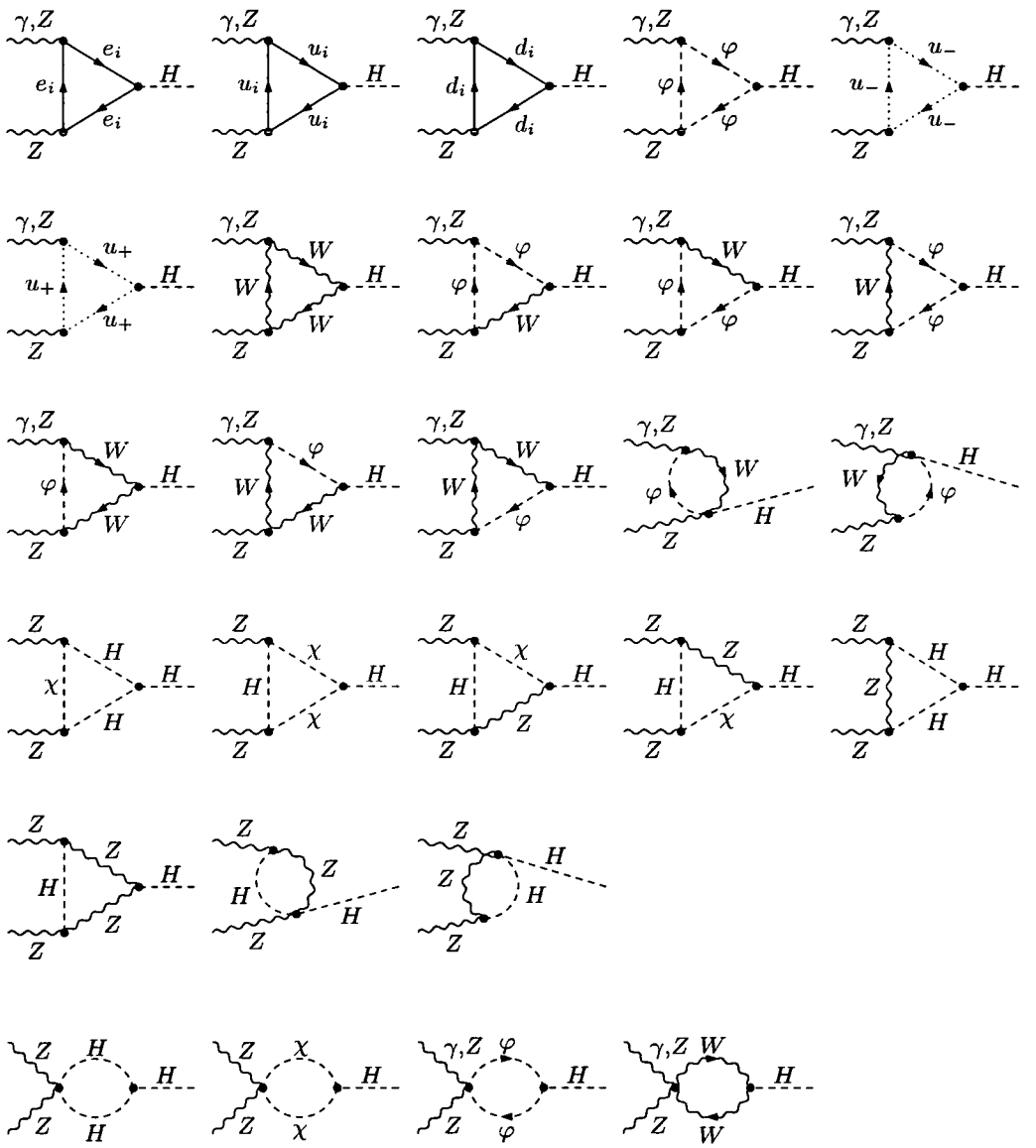

Figure 4.8: Diagrams for the corrections to the ZZH vertices.

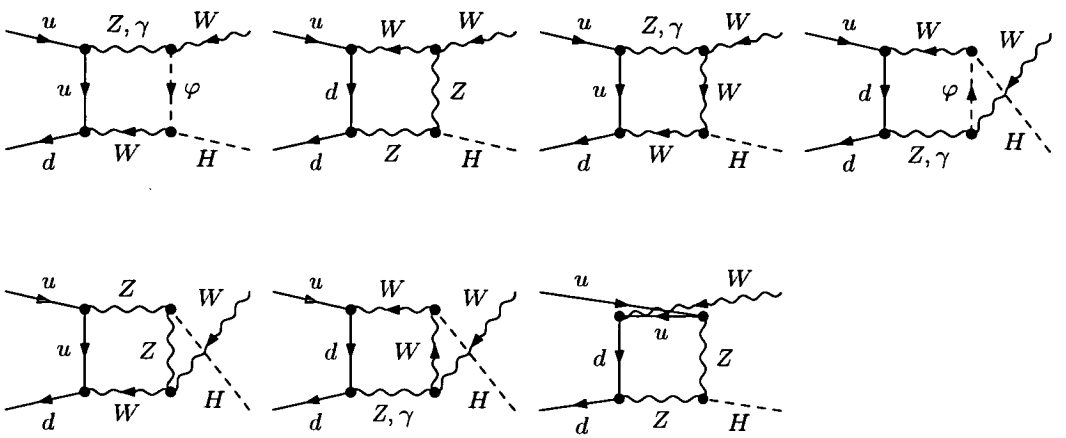

Figure 4.9: Diagrams for box corrections to $u\bar{d} \to WH$.

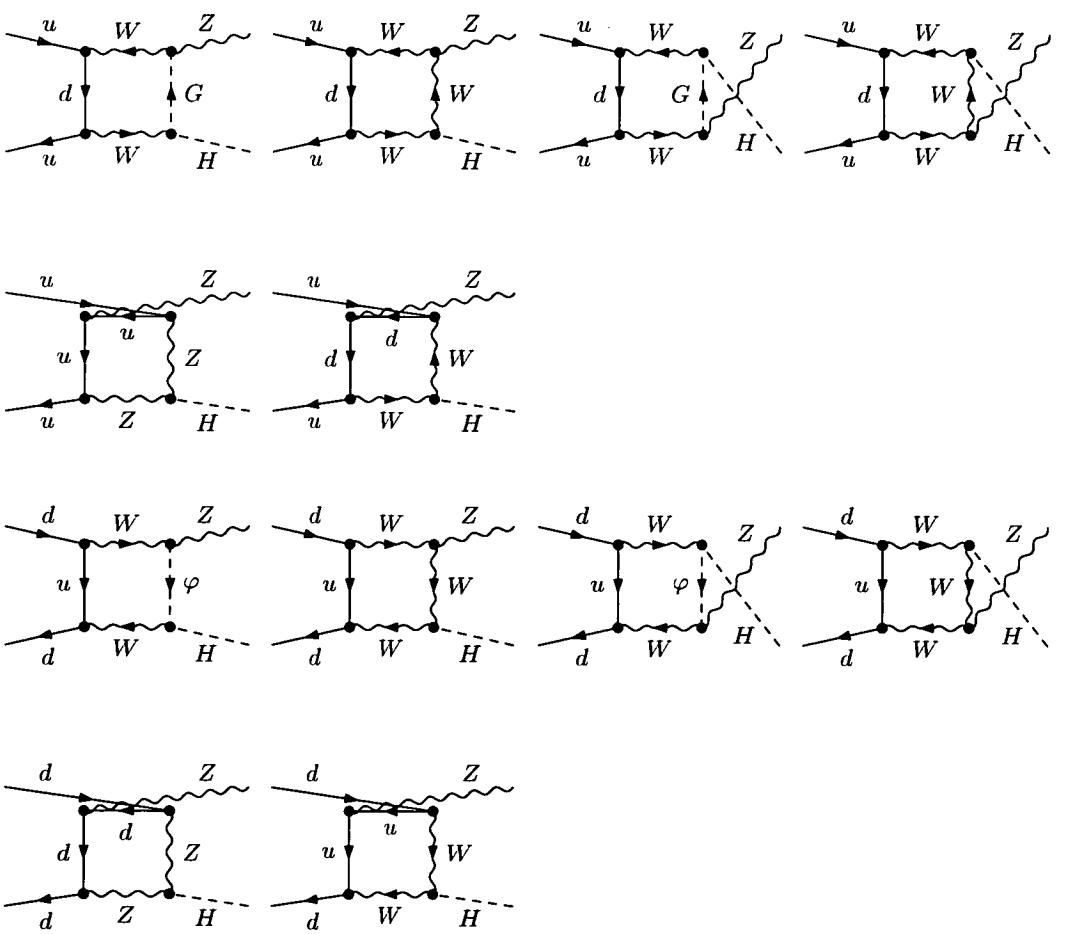

Figure 4.10: Diagrams for box corrections to $q\bar{q} \to ZH$.

to two independent computer codes. The results of the two codes are in good numerical agreement (i.e. within approximately 12 digits for non-exceptional phase-space points). In both calculations ultraviolet divergences are regulated dimensionally and IR divergences with an infinitesimal photon mass m_γ and small quark masses. The renormalization is carried out in the on-shell renormalization scheme, as e.g. described in Ref. [31].

In the first calculation, the Feynman graphs are generated with *FeynArts* version 1.0 [70]. With the help of *Mathematica* routines the amplitudes are expressed in terms of standard matrix elements, which contain the Dirac spinors and polarization vectors, and coefficients of tensor integrals. The tensor coefficients are numerically reduced to scalar integrals using the Passarino–Veltman algorithm [73]. The scalar integrals are evaluated using the methods and results of Refs. [72, 74, 31].

The second calculation has been made using *FeynArts* version 3 [71] for the diagram generation and *FeynCalc* version 4.1.0.3b [75] for the algebraic manipulations of the amplitudes, including the Passarino–Veltman reduction to scalar integrals. The latter have been numerically evaluated using the *Looptools* package [76] version 2.

Renormalization and Input-parameter Schemes

Denoting the one-loop matrix element $\mathcal{M}_1^\tau$, in $\mathcal{O}(\alpha)$ the squared matrix element reads

$$|\mathcal{M}_0^\tau + \mathcal{M}_1^\tau|^2 = |\mathcal{M}_0^\tau|^2 + 2\,\mathrm{Re}\{(\mathcal{M}_0^\tau)^* \mathcal{M}_1^\tau\} + \ldots = (1 + 2\,\mathrm{Re}\{\delta_{\mathrm{virt}}^\tau\})|\mathcal{M}_0^\tau|^2 + \ldots . \quad (4.9)$$

Substituting the r.h.s. of this equation for $|\mathcal{M}_0^\tau|^2$ in (4.7) includes the virtual corrections to the differential parton cross section. The full one-loop corrections are too lengthy and untransparent to be reported completely. Instead, the relevant counterterms are listed, all of which lead to contributions to $\mathcal{M}_1^\tau$ that are proportional to the lowest-order matrix element $\mathcal{M}_0^\tau$, $\mathcal{M}_{\mathrm{ct}}^\tau = \delta_{\mathrm{ct}}^\tau \mathcal{M}_0^\tau$. Explicitly the counterterm factors $\delta_{\mathrm{ct}}^\tau$ for the individual vertex functions read

$$\begin{aligned}
\delta_{\mathrm{ct}}^{WW} &= -\delta Z_W + \frac{\delta M_{\mathrm{W}}^2}{\hat{s} - M_{\mathrm{W}}^2}, \\
\delta_{\mathrm{ct}}^{udW,\tau} &= \left(\delta Z_e - \frac{\delta s_{\mathrm{W}}}{s_{\mathrm{W}}} + \frac{1}{2}\delta Z_W + \frac{1}{2}\delta Z_u^- + \frac{1}{2}\delta Z_d^-\right)\delta_{\tau -}, \\
\delta_{\mathrm{ct}}^{WWH} &= \delta Z_e - \frac{\delta s_{\mathrm{W}}}{s_{\mathrm{W}}} + \frac{\delta M_{\mathrm{W}}^2}{2M_{\mathrm{W}}^2} + \delta Z_W + \frac{1}{2}\delta Z_H,
\end{aligned}$$

$$
\begin{aligned}
\delta_{\mathrm{ct}}^{ZZ} &= -\delta Z_{ZZ} + \frac{\delta M_{\mathrm{Z}}^2}{\hat{s} - M_{\mathrm{Z}}^2}, \\
\delta_{\mathrm{ct}}^{\gamma Z,\tau} &= \frac{Q_q}{2g_{qqZ}^{\tau}} \left[\delta Z_{ZA} \left(1 - \frac{M_{\mathrm{Z}}^2}{\hat{s}} \right) + \delta Z_{AZ} \right], \\
\delta_{\mathrm{ct}}^{qqZ,\tau} &= \delta Z_e + \frac{\delta g_{qqZ}^{\tau}}{g_{qqZ}^{\tau}} + \frac{1}{2}\delta Z_{ZZ} + \delta Z_q^{\tau} - \frac{Q_q}{2g_{qqZ}^{\tau}} \delta Z_{AZ}, \\
\delta_{\mathrm{ct}}^{\gamma ZH,\tau} &= \frac{Q_q}{2g_{qqZ}^{\tau}} \delta Z_{ZA} \left(\frac{M_{\mathrm{Z}}^2}{\hat{s}} - 1 \right), \\
\delta_{\mathrm{ct}}^{ZZH} &= \delta Z_e + \frac{2s_{\mathrm{W}}^2 - c_{\mathrm{W}}^2}{c_{\mathrm{W}}^2} \frac{\delta s_{\mathrm{W}}}{s_{\mathrm{W}}} + \frac{\delta M_{\mathrm{W}}^2}{2M_{\mathrm{W}}^2} + \delta Z_{ZZ} + \frac{1}{2}\delta Z_H.
\end{aligned} \tag{4.10}
$$

The index τ has been suppressed for those counterterms that do not depend on the chirality. The explicit expressions for the renormalization constants can, e.g., be found in Ref. [31]. In the following only the charge renormalization constant δZ_e is analysed. In the $\alpha(0)$-scheme (i.e. the usual on-shell scheme) the electromagnetic coupling e is deduced from the fine-structure constant $\alpha(0)$, as defined in the Thomson limit. This fixes δZ_e to

$$
\delta Z_e\Big|_{\alpha(0)} = \frac{1}{2} \left. \frac{\partial \Sigma_{\mathrm{T}}^{AA}(k^2)}{\partial k^2} \right|_{k^2=0} - \frac{s_{\mathrm{W}}}{c_{\mathrm{W}}} \frac{\Sigma_{\mathrm{T}}^{AZ}(0)}{M_{\mathrm{Z}}^2}, \tag{4.11}
$$

with $\Sigma_{\mathrm{T}}^{VV'}(k^2)$ denoting the transverse part of the VV' gauge-boson self-energy with momentum transfer k. In this scheme the charge renormalization constant δZ_e contains logarithms of the light-fermion masses, inducing large corrections proportional to $\alpha \ln(m_f^2/\hat{s})$, which are related to the running of the electromagnetic coupling $\alpha(k^2)$ from $k = 0$ to a high-energy scale. In order to render these quark-mass logarithms meaningful, it is necessary to adjust these masses to the asymptotic tail of the hadronic contribution to the vacuum polarization $\Pi^{AA}(k^2) \equiv \Sigma_{\mathrm{T}}^{AA}(k^2)/k^2$ of the photon. Using $\alpha(M_{\mathrm{Z}}^2)$, as defined in Ref. [68], as input this adjustment is implicitly incorporated, and the charge renormalization constant is modified to

$$
\delta Z_e\Big|_{\alpha(M_{\mathrm{Z}}^2)} = \delta Z_e\Big|_{\alpha(0)} - \frac{1}{2}\Delta\alpha(M_{\mathrm{Z}}^2), \tag{4.12}
$$

where

$$
\Delta\alpha(k^2) = \Pi_{f\neq \mathrm{t}}^{AA}(0) - \mathrm{Re}\{\Pi_{f\neq \mathrm{t}}^{AA}(k^2)\}, \tag{4.13}
$$

with $\Pi_{f\neq \mathrm{t}}^{AA}$ denoting the photonic vacuum polarization induced by all fermions other than the top quark (see also Ref. [31]). In contrast to the $\alpha(0)$-scheme the counterterm $\delta Z_e|_{\alpha(M_{\mathrm{Z}}^2)}$, and thus the whole relative $\mathcal{O}(\alpha)$ correction in the $\alpha(M_{\mathrm{Z}}^2)$-scheme,

does not involve logarithms of light quark masses, since all corrections of the form $\alpha^n \ln^n(m_f^2/\hat{s})$ are absorbed in the lowest-order cross section parametrized by $\alpha(M_Z^2) = \alpha(0)/[1 - \Delta\alpha(M_Z^2)]$. In the G_μ-scheme, the transition from $\alpha(0)$ to G_μ is ruled by the quantity Δr [77, 31], which is deduced from muon decay,

$$\alpha_{G_\mu} = \frac{\sqrt{2} G_\mu M_W^2 s_W^2}{\pi} = \alpha(0)(1 + \Delta r) + \mathcal{O}(\alpha^3). \tag{4.14}$$

Therefore, the charge renormalization constant reads

$$\delta Z_e\Big|_{G_\mu} = \delta Z_e\Big|_{\alpha(0)} - \frac{1}{2}\Delta r. \tag{4.15}$$

Since $\Delta\alpha(M_Z^2)$ is explicitly contained in Δr, the large fermion-mass logarithms are also resummed in the G_μ-scheme. Moreover, the lowest-order cross section in G_μ-parametrization absorbs large universal corrections to the SU(2) gauge coupling e/s_W induced by the ρ-parameter.

Finally, the universal corrections related to the ρ-parameter, or more generally, the leading corrections induced by heavy top quarks in the loops are considered. To this end, all terms in the corrections that are enhanced by a factor m_t^2/M_W^2 have been extracted. These contributions are conveniently expressed in terms of

$$\Delta\rho_t = \frac{3\alpha}{16\pi s_W^2}\frac{m_t^2}{M_W^2}, \tag{4.16}$$

which is the leading contribution to the ρ parameter. For the various channels the following correction factors to the cross sections in the G_μ-scheme have been obtained,

$$\begin{aligned}
\delta^{\text{top}}_{q\bar{q}'\to WH}\Big|_{G_\mu} &= 2\delta^{\text{top}}_{WWH}\Big|_{G_\mu}, \\
\delta^{\text{top}}_{q\bar{q}\to ZH}\Big|_{G_\mu} &= 2\delta^{\text{top}}_{ZZH}\Big|_{G_\mu} + \Delta\rho_t\left[1 - \frac{2Q_q c_W (g^+_{qqZ} + g^-_{qqZ})}{s_W[(g^+_{qqZ})^2 + (g^-_{qqZ})^2]}\right],
\end{aligned} \tag{4.17}$$

with

$$\delta^{\text{top}}_{WWH}\Big|_{G_\mu} = \delta^{\text{top}}_{ZZH}\Big|_{G_\mu} = -\frac{5}{6}\Delta\rho_t, \tag{4.18}$$

in agreement with the results of Ref. [78]. As mentioned before, for WH production the only effect of $\Delta\rho_t$ is related to the WWH vertex correction in the G_μ-scheme, while such corrections to the $q\bar{q}'W$ coupling are entirely absorbed into the renormalized coupling e/s_W.

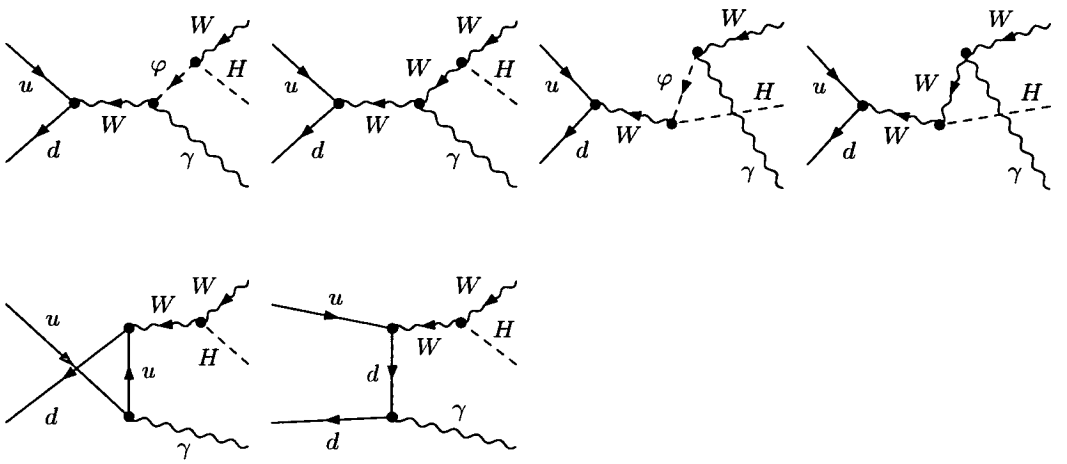

Figure 4.11: Bremsstrahlung diagrams for $u\bar{d} \to WH + \gamma$.

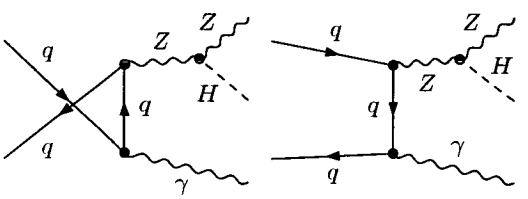

Figure 4.12: Bremsstrahlung diagrams for $q\bar{q} \to ZH + \gamma$.

4.2.3 Real-photon Emission

Real-photonic corrections are induced by the diagrams shown in Figs. 4.11 and 4.12. Helicity amplitudes for the processes $q\bar{q}' \to VH + \gamma$ ($V = W, Z$) have been generated and evaluated using the program packages *MadGraph* [79] and *HELAS* [80]. The result has been verified by an independent calculation based on standard trace techniques. The contribution $\hat{\sigma}_\gamma$ of the radiative process to the parton cross section is given by

$$\hat{\sigma}_\gamma = \frac{1}{12}\frac{1}{2\hat{s}} \int \mathrm{d}\Gamma_\gamma \sum_{\text{spins}} |\mathcal{M}_\gamma|^2, \tag{4.19}$$

where the phase-space integral is defined by

$$\int \mathrm{d}\Gamma_\gamma = \int \frac{\mathrm{d}^3\mathbf{p}_H}{(2\pi)^3 2p_{H,0}} \int \frac{\mathrm{d}^3\mathbf{p}_V}{(2\pi)^3 2p_{V,0}} \int \frac{\mathrm{d}^3\mathbf{k}}{(2\pi)^3 2k_0} (2\pi)^4 \delta(p_q + p_{\bar{q}'} - p_H - p_V - k). \tag{4.20}$$

4.2.4 Treatment of Soft and Collinear Singularities

The phase-space integral (4.19) diverges in the soft ($k_0 \to 0$) and collinear ($p_q k, p_{\bar{q}'} k \to 0$) regions logarithmically if the photon and fermion masses are set to zero. For the

treatment of the soft and collinear singularities the phase-space slicing method has been applied. In addition, for associated ZH production the dipole subtraction method has also been applied. In the following these two approaches are briefly described.

Phase-space Slicing

Firstly, phase-space slicing is used, excluding the soft-photon and collinear regions in the integral (4.19).

In the soft-photon region $m_\gamma < k_0 < \Delta E \ll \sqrt{\hat{s}}$ the bremsstrahlung cross section factorizes into the lowest-order cross section and a universal eikonal factor that depends on the photon momentum k (see e.g. Ref. [31]). Integration over k in the partonic CM frame yields a simple correction factor δ_{soft} to the partonic Born cross section $\mathrm{d}\hat{\sigma}_0$. For ZH production this factor is

$$\begin{aligned}\delta_{\text{soft}} &= -\frac{\alpha}{\pi}Q_q^2\left\{2\ln\left(\frac{2\Delta E}{m_\gamma}\right)\ln\left(\frac{m_q^2}{\hat{s}}\right)\right. \\ &\quad \left. + 2\ln\left(\frac{2\Delta E}{m_\gamma}\right) + \frac{1}{2}\ln^2\left(\frac{m_q^2}{\hat{s}}\right) + \ln\left(\frac{m_q^2}{\hat{s}}\right) + \frac{\pi^2}{3}\right\}. \end{aligned} \tag{4.21}$$

For WH production the soft factor is

$$\begin{aligned}\delta_{\text{soft}} &= -\frac{\alpha}{2\pi}\left\{Q_q^2\left[2\ln\left(\frac{2\Delta E}{m_\gamma}\right)\ln\left(\frac{m_q^2}{\hat{s}}\right) + 2\ln\left(\frac{2\Delta E}{m_\gamma}\right) + \frac{1}{2}\ln^2\left(\frac{m_q^2}{\hat{s}}\right) + \ln\left(\frac{m_q^2}{\hat{s}}\right) + \frac{\pi^2}{3}\right]\right. \\ &\quad + Q_{q'}^2\left[2\ln\left(\frac{2\Delta E}{m_\gamma}\right)\ln\left(\frac{m_{q'}^2}{\hat{s}}\right) + 2\ln\left(\frac{2\Delta E}{m_\gamma}\right) + \frac{1}{2}\ln^2\left(\frac{m_{q'}^2}{\hat{s}}\right)\right. \\ &\quad \left. + \ln\left(\frac{m_{q'}^2}{\hat{s}}\right) + \frac{\pi^2}{3}\right] \\ &\quad + \left[2\ln\left(\frac{2\Delta E}{m_\gamma}\right)\ln\left(\frac{M_{\mathrm{W}}^2}{\hat{s}}\right) + 2\ln\left(\frac{2\Delta E}{m_\gamma}\right) + \frac{1}{2}\ln^2\left(\frac{M_{\mathrm{W}}^2}{(p_W^0 + |\mathbf{p}_W|)^2}\right)\right. \\ &\quad \left. + \frac{p_W^0}{|\mathbf{p}_W|}\ln\left(\frac{M_{\mathrm{W}}^2}{(p_W^0 + |\mathbf{p}_W|)^2}\right)\right] \\ &\quad + 2Q_q\left[2\ln\left(\frac{\hat{s}}{M_{\mathrm{W}}^2 - \hat{t}}\right)\ln\left(\frac{2\Delta E}{m_\gamma}\right) + \mathrm{Li}_2\left(1 + \frac{\sqrt{\hat{s}}}{\hat{t} - M_{\mathrm{W}}^2}(p_W^0 - |\mathbf{p}_W|)\right)\right. \\ &\quad \left. + \mathrm{Li}_2\left(1 + \frac{\sqrt{\hat{s}}}{\hat{t} - M_{\mathrm{W}}^2}(p_W^0 + |\mathbf{p}_W|)\right)\right] \\ &\quad - 2Q_{q'}\left[2\ln\left(\frac{\hat{s}}{M_{\mathrm{W}}^2 - \hat{u}}\right)\ln\left(\frac{2\Delta E}{m_\gamma}\right) + \mathrm{Li}_2\left(1 + \frac{\sqrt{\hat{s}}}{\hat{u} - M_{\mathrm{W}}^2}(p_W^0 - |\mathbf{p}\mathbf{w}|)\right)\right. \\ &\quad \left.\left. + \mathrm{Li}_2\left(1 + \frac{\sqrt{\hat{s}}}{\hat{u} - M_{\mathrm{W}}^2}(p_W^0 + |\mathbf{p}\mathbf{w}|)\right)\right]\right\}, \end{aligned} \tag{4.22}$$

where Li_2 is the dilogarithm function and $Q_q - Q_{q'} = +1$. The difference between ZH and WH production is due to the soft photons emitted by the W boson.

The factor δ_{soft} can be added directly to the virtual correction factor $2\,\mathrm{Re}\{\delta^{\tau}_{\mathrm{virt}}\}$ defined in (4.9). It has been checked that the photon mass m_γ cancels in the sum $2\,\mathrm{Re}\{\delta^{\tau}_{\mathrm{virt}}\} + \delta_{\mathrm{soft}}$.

The remaining phase-space integration in (4.19) with $k_0 > \Delta E$ still contains the collinear singularities in the regions in which $(p_q k)$ or $(p_{\bar{q}'} k)$ is small. Defining $\theta_{f\gamma} = \angle(\mathbf{p}_f, \mathbf{k})$ as the angle of the photon emission off $f = q, \bar{q}'$, the collinear regions are excluded by the angular cuts $\theta_{f\gamma} < \Delta\theta \ll 1$ in the integral (4.19).

In the collinear cones the photon emission angles $\theta_{f\gamma}$ can be integrated out. The resulting contribution to the bremsstrahlung cross section has the form of a convolution of the lowest-order cross section,

$$\begin{aligned} \hat{\sigma}_{\mathrm{coll}} &= \hat{\sigma}_{\mathrm{coll},q} + \hat{\sigma}_{\mathrm{coll},\bar{q}'}, \\ \hat{\sigma}_{\mathrm{coll},f}(p_f) &= \frac{Q_f^2 \alpha}{2\pi} \int_0^{1-2\Delta E/\sqrt{\hat{s}}} \mathrm{d}z \left[\ln\left(\frac{\Delta\theta^2 \hat{s}}{4m_f^2}\right) - \frac{2z}{1+z^2} \right] P_{ff}(z) \hat{\sigma}_0(z p_f), \qquad f = q, \bar{q}' \end{aligned} \tag{4.23}$$

with the splitting function

$$P_{ff}(z) = \frac{1+z^2}{1-z}. \tag{4.24}$$

Note that the quark momentum p_f is reduced by the factor z so that the partonic CM frame for the hard scattering receives a boost.

Subtraction Method

Alternatively, for ZH production, the subtraction method presented in Ref. [81] is applied, where the so-called "dipole formalism", originally introduced by Catani and Seymour [82] within massless QCD, was applied to photon radiation and generalized to massive fermions. The general idea of a subtraction method is to subtract and to add a simple auxiliary function from the singular integrand. This auxiliary function has to be chosen such that it cancels all singularities of the original integrand so that the phase-space integration of the difference can be performed numerically. Moreover, the auxiliary function has to be simple enough so that it can be integrated over the singular regions analytically, when the subtracted contribution is added again.

The dipole subtraction function consists of contributions labelled by all ordered pairs of charged external particles, one of which is called *emitter*, the other one *spectator*. For $q\bar{q} \to ZH$ there are, thus, two different emitter/spectator cases ff': $q\bar{q}$, $\bar{q}q$. The subtraction function that is subtracted from $\sum_{\text{spins}} |\mathcal{M}_\gamma|^2$ is given by

$$\begin{aligned} |\mathcal{M}_{\text{sub}}|^2 &= Q_q^2 e^2 \Big[g_{q\bar{q}}(p_q, p_{\bar{q}}, k) \sum_{\text{spins}} |\mathcal{M}_0^\tau(x_{q\bar{q}} p_q, p_{\bar{q}}, k_{Z,q\bar{q}})|^2 \\ &\quad + g_{\bar{q}q}(p_{\bar{q}}, p_q, k) \sum_{\text{spins}} |\mathcal{M}_0^\tau(p_q, x_{q\bar{q}} p_{\bar{q}}, k_{Z,\bar{q}q})|^2 \Big] \end{aligned} \tag{4.25}$$

with the functions

$$\begin{aligned} g_{q\bar{q}}(p_q, p_{\bar{q}}, k) &= \frac{1}{(p_q k) x_{q\bar{q}}} \left[\frac{2}{1 - x_{q\bar{q}}} - 1 - x_{q\bar{q}} \right], \\ g_{\bar{q}q}(p_{\bar{q}}, p_q, k) &= \frac{1}{(p_{\bar{q}} k) x_{q\bar{q}}} \left[\frac{2}{1 - x_{q\bar{q}}} - 1 - x_{q\bar{q}} \right], \end{aligned} \tag{4.26}$$

and the auxiliary variable

$$x_{q\bar{q}} = \frac{p_q p_{\bar{q}} - p_q k - p_{\bar{q}} k}{p_q p_{\bar{q}}}, \tag{4.27}$$

For the evaluation of $|\mathcal{M}_{\text{sub}}|^2$ in (4.25) the Z-boson momenta $k_{Z,ff'}$ still have to be specified. They are given by

$$k_{Z,q\bar{q}}^\mu = \Lambda(p_q, p_{\bar{q}})^\mu{}_\nu k_Z^\nu, \qquad k_{Z,\bar{q}q}^\mu = \Lambda(p_{\bar{q}}, p_q)^\mu{}_\nu k_Z^\nu, \tag{4.28}$$

with the Lorentz transformation matrix

$$\Lambda(p_1, p_2)^\mu{}_\nu = g^\mu{}_\nu - \frac{(P + \tilde{P})^\mu (P + \tilde{P})_\nu}{P^2 + P\tilde{P}} + \frac{2\tilde{P}^\mu P_\nu}{P^2}, \qquad P^\mu = k_Z^\mu + k_H^\mu, \quad \tilde{P}^\mu = x_{q\bar{q}} p_1^\mu + p_2^\mu. \tag{4.29}$$

The modified Z-boson momenta $k_{Z,ff'}$ still obey the on-shell condition $k_{Z,ff'}^2 = M_Z^2$, and the same is true for the corresponding Higgs-boson momenta that result from momentum conservation. It is straightforward to check that all collinear and soft singularities cancel in $\sum_{\text{spins}} |\mathcal{M}_\gamma|^2 - |\mathcal{M}_{\text{sub}}|^2$ so that this difference can be integrated numerically over the entire phase space (4.20).

The contribution of $|\mathcal{M}_{\text{sub}}|^2$, which has been subtracted by hand, has to be added again. This is done after the singular degrees of freedom in the phase space (4.20) are integrated out analytically, keeping an infinitesimal photon mass m_γ and small fermion masses m_f as regulators [81]. The resulting contribution is split into two parts: one that factorizes from the lowest-order cross section $\hat{\sigma}_0$ and another part that has the

form of a convolution integral over $\hat{\sigma}_0$ with reduced CM energy. The first part is given by

$$\hat{\sigma}_{\mathrm{sub},1} = Q_q^2 \frac{\alpha}{2\pi} \left[2\mathcal{L}(\hat{s}, m_q^2) + 3 - \frac{2\pi^2}{3} \right] \hat{\sigma}_0 \tag{4.30}$$

with the auxiliary function

$$\mathcal{L}(r, m_q^2) = \ln\left(\frac{m_q^2}{r}\right) \ln\left(\frac{m_\gamma^2}{r}\right) + \ln\left(\frac{m_\gamma^2}{r}\right) - \frac{1}{2} \ln^2\left(\frac{m_q^2}{r}\right) + \frac{1}{2} \ln\left(\frac{m_q^2}{r}\right). \tag{4.31}$$

The IR and fermion-mass singularities contained in $\mathrm{d}\hat{\sigma}_{\mathrm{sub},1}$ exactly cancel those of the virtual corrections. The second integrated subtraction contribution is given by

$$\begin{aligned} \hat{\sigma}_{\mathrm{sub},2}(p_q, p_{\bar{q}}) = {} & Q_q^2 \frac{\alpha}{2\pi} \int_0^1 \mathrm{d}x \left\{ \left[\mathcal{G}_{q\bar{q}}(\hat{s}, x)\right]_+ \hat{\sigma}_0(x p_q, p_{\bar{q}}) + \left[\mathcal{G}_{\bar{q}q}(\hat{s}, x)\right]_+ \hat{\sigma}_0(p_q, x p_{\bar{q}}) \right\} \Big|_{\hat{s}=(p_q+p_{\bar{q}})^2} \\ & + Q_q^2 \frac{\alpha}{2\pi} \int_0^1 \mathrm{d}x \, (1-x) \left\{ \hat{\sigma}_0(x p_q, p_{\bar{q}}) \Big|_{\tau_q \to -\tau_q} + \hat{\sigma}_0(p_q, x p_{\bar{q}}) \Big|_{\tau_{\bar{q}} \to -\tau_{\bar{q}}} \right\}, \end{aligned} \tag{4.32}$$

where the usual $[\ldots]_+$ prescription,

$$\int_0^1 \mathrm{d}x \left[f(x)\right]_+ g(x) = \int_0^1 \mathrm{d}x \, f(x) \left[g(x) - g(1)\right], \tag{4.33}$$

is applied to the integration kernels

$$\mathcal{G}_{q\bar{q}}(r, x) = \mathcal{G}_{\bar{q}q}(r, x) = P_{ff}(x) \left[\ln\left(\frac{r}{m_q^2}\right) - 1 \right]. \tag{4.34}$$

In (4.32) it is indicated explicitly how the Mandelstam variable r has to be chosen in terms of the momenta in the evaluation of the part containing $[\mathcal{G}_{ff'}(r, x)]_+$. Note, however, that in (4.32) the variable $\hat{s}$ that is implicitly used in the calculation of $\hat{\sigma}_0(\ldots)$ is reduced to $2x p_q p_{\bar{q}} = x\hat{s}$.

In summary, within the subtraction approach the real correction reads

$$\hat{\sigma}_\gamma = \frac{1}{12} \frac{1}{2\hat{s}} \int \mathrm{d}\Gamma_\gamma \left[\sum_{\text{spins}} |\mathcal{M}_\gamma|^2 - |\mathcal{M}_{\mathrm{sub}}|^2 \right] + \hat{\sigma}_{\mathrm{sub},1} + \hat{\sigma}_{\mathrm{sub},2}. \tag{4.35}$$

It should be realized that in $\hat{\sigma}_{\mathrm{sub},1}$ and $\hat{\sigma}_{\mathrm{sub},2}$ the full photonic phase space is integrated over. This does, however, not restrict the subtraction approach to observables that are fully inclusive with respect to emitted photons, but rather to observables that are inclusive with respect to photons that are soft or collinear to any charged external fermion (see discussions in Sect. 6.2 of Ref. [81] and Sect. 7 of Ref. [82]).

4.3 The Hadron Cross Section

The proton–(anti-)proton cross section σ is obtained from the parton cross sections $\hat{\sigma}^{(q_1q_2)}$ by convolution with the corresponding parton distribution functions $q_{1,2}(x)$,

$$\mathrm{d}\sigma(s) = \sum_{q_1q_2} \int_0^1 \mathrm{d}x_1 \int_0^1 \mathrm{d}x_2\, q_1(x_1) q_2(x_2)\, \mathrm{d}\hat{\sigma}^{(q_1q_2)}(p_{q_1}, p_{q_2}), \tag{4.36}$$

where $x_{1,2}$ are the respective momentum fractions carried by the partons $q_{1,2}$. In the sum $\sum_{q_1q_2}$ the quark pairs q_1q_2 run over all possible combinations $q\bar{q}'$ and $\bar{q}'q$ where $q = \mathrm{u}, \mathrm{c}$ and $q' = \mathrm{d}, \mathrm{s}$ for WH production and $q = q' = \mathrm{u}, \mathrm{d}, \mathrm{s}, \mathrm{c}, \mathrm{b}$ for ZH production. The squared CM energy s of the pp ($\mathrm{p\bar{p}}$) system is related to the squared parton CM energy $\hat{s}$ by $\hat{s} = x_1x_2s$.

The $\mathcal{O}(\alpha)$-corrected parton cross section $\hat{\sigma}^{(q_1q_2)}$ contains mass singularities of the form $\alpha \ln(m_q)$, which are due to collinear photon radiation off the initial-state quarks. In complete analogy to the $\overline{\mathrm{MS}}$ factorization scheme for next-to-leading order QCD corrections, these collinear singularities are absorbed into the quark distributions. This is achieved by replacing $q(x)$ in (4.36) according to

$$\begin{aligned} q(x) \;\to\; & q(x, M^2) \\ & - \int_x^1 \frac{\mathrm{d}z}{z}\, q\left(\frac{x}{z}, M^2\right) \frac{\alpha}{2\pi}\, Q_q^2 \left\{ \ln\left(\frac{M^2}{m_q^2}\right) \Big[P_{ff}(z)\Big]_+ - \Big[P_{ff}(z)\Big(2\ln(1-z)+1\Big)\Big]_+ \right\}, \end{aligned} \tag{4.37}$$

where M is the factorization scale (see Ref. [65]). This replacement defines the same finite parts in the $\mathcal{O}(\alpha)$ correction as the usual $\overline{\mathrm{MS}}$ factorization in D-dimensional regularization for exactly massless partons, where the $\ln(m_q)$ terms appear as $1/(D-4)$ poles. In (4.37) the soft-photon pole has been regularized by using the $[\ldots]_+$ prescription. This procedure is fully equivalent to the application of a soft-photon cutoff ΔE (see Ref. [64]) where

$$\begin{aligned} q(x) \;\to\; & q(x, M^2) \left[1 - \frac{\alpha}{\pi}\, Q_q^2 \left\{ 1 - \ln(2\Delta E/\sqrt{\hat{s}}) - \ln^2(2\Delta E/\sqrt{\hat{s}}) \right.\right. \\ & \left.\left. + \left(\ln(2\Delta E/\sqrt{\hat{s}}) + \frac{3}{4}\right) \ln\left(\frac{M^2}{m_q^2}\right) \right\} \right] \\ & - \int_x^{1-2\Delta E/\sqrt{\hat{s}}} \frac{dz}{z}\, q\left(\frac{x}{z}, M^2\right) \frac{\alpha}{2\pi}\, Q_q^2\, P_{ff}(z) \left\{ \ln\left(\frac{M^2}{m_q^2} \frac{1}{(1-z)^2}\right) - 1 \right\} \end{aligned} \tag{4.38}$$

The absorption of the collinear singularities of $\mathcal{O}(\alpha)$ into quark distributions, as a matter of fact, requires also the inclusion of the corresponding $\mathcal{O}(\alpha)$ corrections

into the DGLAP evolution of these distributions and into their fit to experimental data. At present, this full incorporation of $\mathcal{O}(\alpha)$ effects in the determination of the quark distributions has not yet been performed. However, an approximate inclusion of the $\mathcal{O}(\alpha)$ corrections to the DGLAP evolution shows [83] that the impact of these corrections on the quark distributions in the $\overline{\text{MS}}$ factorization scheme is well below 1%, at least in the x range that is relevant for associated VH production at the Tevatron and the LHC. Therefore, the neglect of these corrections to the parton distributions is justified for the following numerical study.

4.4 Numerical Results

4.4.1 Input Parameters

For the numerical evaluation the following set of input parameters has been used [84],

$$\begin{aligned}
\alpha(0) &= 1/137.03599976, & G_\mu &= 1.16639 \times 10^{-5}\,\text{GeV}^{-2},\\
\alpha(M_Z) &= 1/128.930, & M_\text{W} &= 80.423\,\text{GeV},\\
M_\text{Z} &= 91.1876\,\text{GeV}, & m_\text{e} &= 0.510998902\,\text{MeV},\\
m_\mu &= 105.658357\,\text{MeV}, & m_\tau &= 1.77699\,\text{GeV},\\
m_\text{u} &= 66\,\text{MeV}, & m_\text{c} &= 1.2\,\text{GeV},\\
m_\text{t} &= 174.3\,\text{GeV}, & m_\text{d} &= 66\,\text{MeV},\\
m_\text{s} &= 150\,\text{MeV}, & m_\text{b} &= 4.3\,\text{GeV}\\
|V_\text{ud}| &= 0.975, & |V_\text{us}| &= 0.222,\\
|V_\text{cd}| &= 0.222, & |V_\text{cs}| &= 0.975.
\end{aligned} \tag{4.39}$$

The masses of the light quarks are adjusted such as to reproduce the hadronic contribution to the photonic vacuum polarization of Ref. [68]. They are relevant only for the evaluation of the charge renormalization constant δZ_e in the $\alpha(0)$-scheme. For the calculation of the pp and $\text{p}\bar{\text{p}}$ cross sections the CTEQ6L1 and CTEQ6M [85] parton distribution functions at LO and $\mathcal{O}(\alpha_\text{s})$, have been adopted corresponding to $\Lambda_5^\text{LO} = 165\,\text{MeV}$ and $\Lambda_5^{\overline{\text{MS}}} = 226\,\text{MeV}$ at the one- and two-loop level of the strong coupling $\alpha_\text{s}(\mu)$, respec-

tively. The top quark is decoupled from the running of $\alpha_s(\mu)$. If not stated otherwise the factorization scale M is set to the invariant mass of the Higgs–vector-boson pair, $M = \sqrt{s_{VH}}$. For the treatment of the soft and collinear singularities the phase-space slicing method as described in Sect. 4.2.4 has been applied. It has been verified that the results are independent of the slicing parameters $2\Delta E/\sqrt{\hat{s}}$ and $\Delta\theta$ when these parameters are varied within the range $10^{-2} - 10^{-4}$. In the case of associated ZH production the dipole subtraction method was also applied. The results agree with those obtained using phase-space slicing. It has been observed that the integration error of the subtraction method is smaller than that of the slicing method by at least a factor of two.

4.4.2 Electroweak Corrections

The impact of the electroweak $\mathcal{O}(\alpha)$ corrections on the cross section predictions for the processes $p\bar{p}/pp \to W^+H + X$ and $p\bar{p}/pp \to ZH + X$ at the Tevatron and the LHC are presented. Figures 4.13 and 4.14 show the relative size of the $\mathcal{O}(\alpha)$ corrections as a function of the Higgs-boson mass for $p\bar{p} \to W^+H + X$ and $p\bar{p} \to ZH + X$ at the Tevatron. Results are presented for the three different input-parameter schemes. The corrections in the G_μ- and $\alpha(M_Z^2)$-schemes are significant and reduce the cross section by 5–9% and by 10–15%, respectively. The corrections in the $\alpha(0)$-scheme differ from those in the G_μ-scheme by $2\Delta r \approx 6\%$ and from those in the $\alpha(M_Z^2)$-scheme by $2\Delta\alpha(M_Z^2) \approx 12\%$. The fact that the relative corrections in the $\alpha(0)$-scheme are rather small results from accidental cancellations between the running of the electromagnetic coupling, which leads to a contribution of about $2\Delta\alpha(M_Z^2) \approx +12\%$, and other (negative) corrections of non-universal origin. Thus, corrections beyond $\mathcal{O}(\alpha)$ in the $\alpha(0)$-scheme cannot be expected to be suppressed as well. In all schemes, the size of the corrections does not depend strongly on the Higgs-boson mass. The unphysical singularities at the thresholds $M_H = 2M_W$ and $2M_Z$ can be removed by taking into account the finite widths of the unstable particles, see e.g. Refs. [86]. Representative results for the leading-order cross section and the electroweak $\mathcal{O}(\alpha)$ corrections are collected in Tables 4.1 and 4.2.

Figures 4.15 and 4.16 and Tables 4.3 and 4.4 show the corresponding results for $pp \to W^+H + X$ and $pp \to ZH + X$ at the LHC. The corrections are similar in size to those at the Tevatron and reduce the cross section by 5–10% in the G_μ-scheme and by

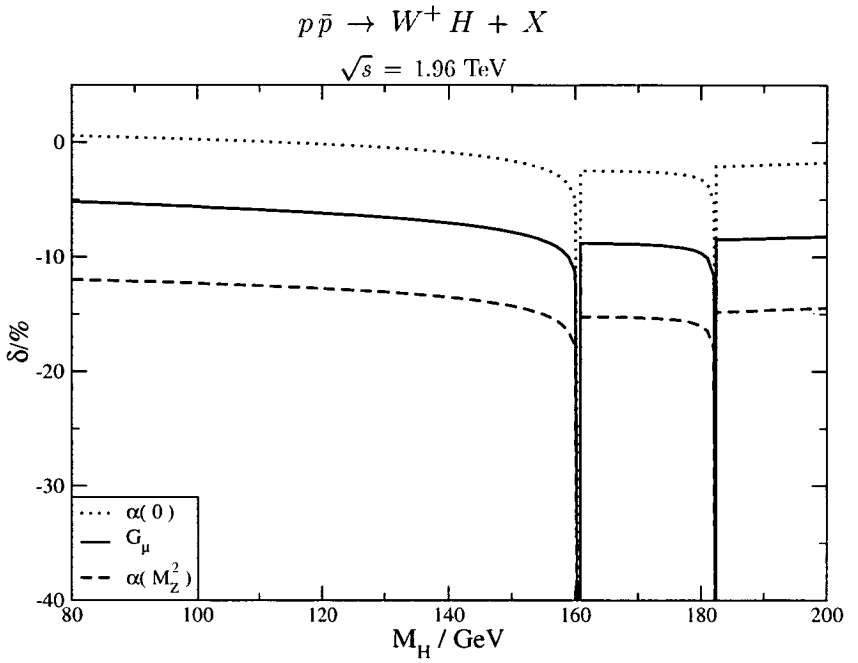

Figure 4.13: Relative electroweak correction δ as a function of the Higgs-boson mass for the total cross section $p\bar{p} \to W^+H + X$ ($\sqrt{s} = 1.96$ TeV). Results are presented for the $\alpha(0)$-, $\alpha(M_Z^2)$-, and G_μ-schemes.

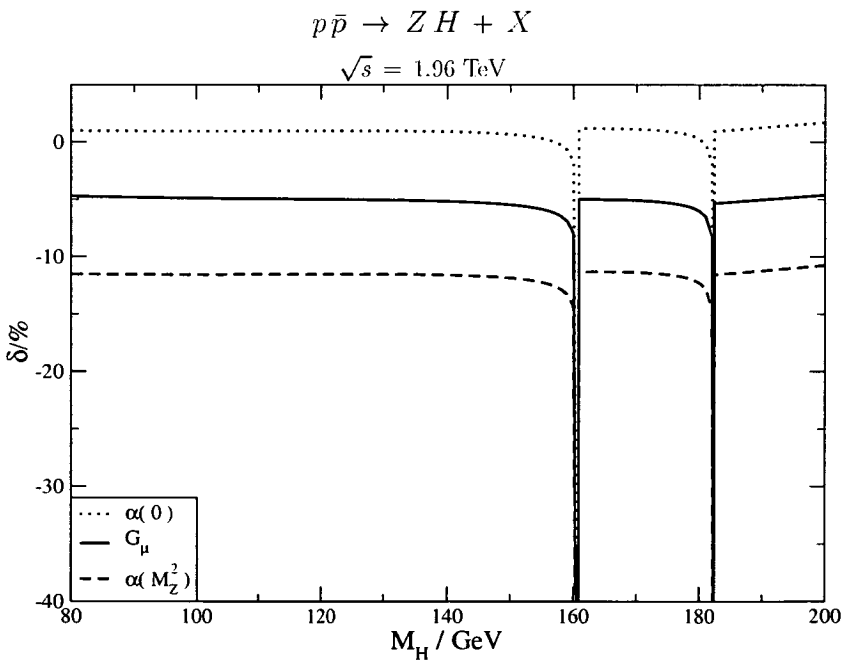

Figure 4.14: Relative electroweak correction δ as a function of the Higgs-boson mass for the total cross section $p\bar{p} \to ZH + X$ ($\sqrt{s} = 1.96$ TeV).

M_H/GeV	$\sigma_0\|_{\alpha(0)}$/pb	$\delta\|_{\alpha(0)}$/%	$\sigma_0\|_{\alpha(M_Z^2)}$/pb	$\delta\|_{\alpha(M_Z^2)}$/%	$\sigma_0\|_{G_\mu}$/pb	$\delta\|_{G_\mu}$/%
80.00	0.1926(1)	0.57(1)	0.2175(1)	−11.99(1)	0.2058(1)	−5.17(1)
100.00	0.09614(1)	0.25(1)	0.1086(1)	−12.29(1)	0.1028(1)	−5.61(1)
120.00	0.05176(1)	−0.17(1)	0.05846(1)	−12.75(1)	0.05532(1)	−6.19(1)
140.00	0.02945(1)	−0.89(1)	0.03327(1)	−13.53(1)	0.03149(1)	−7.05(1)
170.00	0.01367(1)	−2.55(1)	0.01544(1)	−15.30(1)	0.01461(1)	−8.90(1)
190.00	0.008517(1)	−1.97(1)	0.009624(1)	−14.66(1)	0.009106(1)	−8.38(1)

Table 4.1: Total lowest-order hadronic cross section $\sigma_0(p\bar{p} \to W^+ H + X)$ and corresponding relative electroweak correction δ ($\sqrt{s} = 1.96$ TeV). Results are presented for the $\alpha(0)$-, $\alpha(M_Z^2)$-, and G_μ-schemes. The integration error is given in brackets.

M_H/GeV	$\sigma_0\|_{\alpha(0)}$/pb	$\delta\|_{\alpha(0)}$/%	$\sigma_0\|_{\alpha(M_Z^2)}$/pb	$\delta\|_{\alpha(M_Z^2)}$/%	$\sigma_0\|_{G_\mu}$/pb	$\delta\|_{G_\mu}$/%
80.00	0.2199(1)	0.99(1)	0.2484(1)	−11.52(1)	0.2350(1)	−4.73(1)
100.00	0.1142(1)	0.95(1)	0.1290(1)	−11.57(1)	0.1221(1)	−4.91(1)
120.00	0.06358(1)	0.97(1)	0.07182(1)	−11.55(1)	0.06796(1)	−5.01(1)
140.00	0.03727(1)	0.91(1)	0.04211(1)	−11.61(1)	0.03984(1)	−5.18(1)
170.00	0.01799(1)	1.12(1)	0.02032(1)	−11.38(1)	0.01922(1)	−5.10(1)
190.00	0.01148(1)	1.26(1)	0.01297(1)	−11.24(1)	0.01227(1)	−5.04(1)

Table 4.2: Total lowest-order hadronic cross section $\sigma_0(p\bar{p} \to Z H + X)$ and corresponding relative electroweak correction δ ($\sqrt{s} = 1.96$ TeV).

12–17% in the $\alpha(M_Z^2)$-scheme. It is important to note that the electroweak corrections to $pp \to W^-H + X$ at the LHC differ from those to $pp \to W^+H + X$ by less than about 2%.

In order to unravel the origin of the electroweak corrections we display the contributions of individual gauge-invariant building blocks. Figure 4.17 separates the fermionic corrections (comprising all diagrams with closed fermion loops) from the remaining bosonic contributions to $p\bar{p} \to W^+H + X$ at the Tevatron in the G_μ-scheme. It can be seen that the bosonic corrections are dominant and that bosonic and fermionic contributions partly compensate each other. A similar result is found for the $p\bar{p} \to ZH + X$ cross section, where the gauge-invariant contributions from (photonic) QED corrections, fermionic corrections, and weak bosonic corrections are displayed in Fig. 4.18. Note that large logarithmic corrections from initial-state photon radiation have been absorbed into the quark distribution functions. The remainder of the QED corrections turns out to be strongly suppressed with respect to the fermionic and weak bosonic corrections. A similar pattern is observed for the $pp \to W^+H + X$ and $pp \to ZH + X$ cross sections at the LHC, see Figs. 4.19 and 4.20.

At first sight, the large size of the non-universal corrections, i.e. corrections that are not due to the running of $\alpha(k^2)$, photon radiation, or other universal effects, might be surprising. However, a similar pattern has already been observed in the electroweak corrections to the processes $e^+e^- \to ZH$ [67] and $e^+e^- \to Z^*H \to \nu\bar{\nu}H$ [87, 69]. Also there large non-universal fermionic and bosonic corrections of opposite sign occur. It was also observed that the corrections cannot be approximated by simple formulae resulting from appropriate asymptotic limits.[1] For instance, taking the large top-mass limit ($m_t \to \infty$) in the fermionic corrections to WH production in the G_μ-scheme (see Sect. 4.2.2), the leading term in the relative correction is given by $\delta^{\text{top}}_{q\bar{q}'\to WH}\big|_{G_\mu} \approx -1.6\%$, which even differs in sign from the full result (see Fig. 4.17). The reason for this failure is that the relevant scale in the WWH vertex, from which the leading m_t^2 term in the limit

[1] In Ref. [88] the part of the fermion-loop correction that is enhanced by an explicit factor $\alpha m_t^2/M_W^2$ was calculated. Moreover, in the second paper of Ref. [88] also diagrams with internal Higgs bosons were taken into account. Using $\alpha = 1/128$, which roughly corresponds to the $\alpha(M_Z^2)$-scheme, these authors find about -1% to -2% for the sum of these corrections, which were assumed to be the leading ones. This has to be compared with our result of about -12% for the full $\mathcal{O}(\alpha)$ corrections in the $\alpha(M_Z^2)$-scheme.

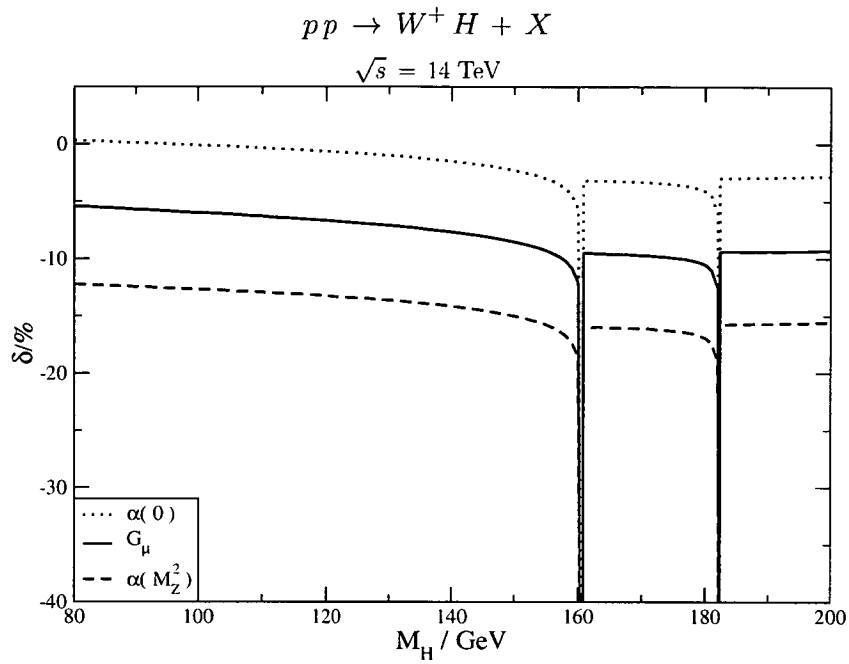

Figure 4.15: Relative electroweak correction δ as a function of the Higgs-boson mass for the total cross section $pp \to W^+H + X$ ($\sqrt{s} = 14$ TeV).

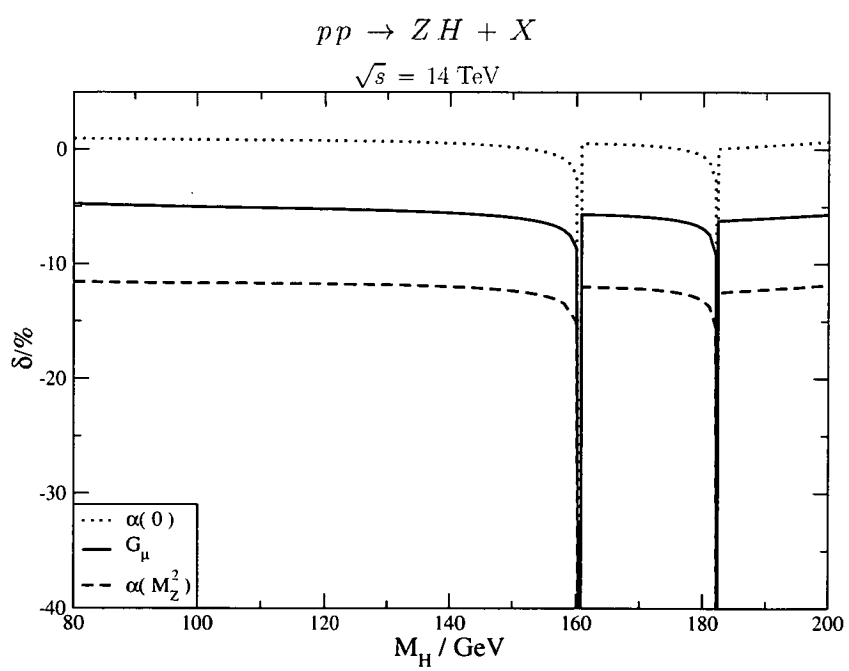

Figure 4.16: Relative electroweak correction δ as a function of the Higgs-boson mass for the total cross section $pp \to ZH + X$ ($\sqrt{s} = 14$ TeV).

M_H/GeV	$\sigma_0\|_{\alpha(0)}$/pb	$\delta\|_{\alpha(0)}$/%	$\sigma_0\|_{\alpha(M_Z^2)}$/pb	$\delta\|_{\alpha(M_Z^2)}$/%	$\sigma_0\|_{G_\mu}$/pb	$\delta\|_{G_\mu}$/%
80.00	2.660(1)	0.31(1)	3.005(1)	−12.22(2)	2.844(1)	−5.43(1)
100.00	1.410(1)	−0.11(1)	1.594(1)	−12.67(2)	1.508(1)	−5.99(1)
120.00	0.8114(2)	−0.65(1)	0.9166(2)	−13.24(2)	0.8673(2)	−6.67(1)
140.00	0.4967(1)	−1.49(1)	0.5610(1)	−14.16(2)	0.5309(1)	−7.68(1)
170.00	0.2605(1)	−3.33(1)	0.2942(1)	−16.12(2)	0.2784(1)	−9.72(2)
190.00	0.1776(1)	−2.92(1)	0.2007(1)	−15.67(2)	0.1899(1)	−9.36(1)

Table 4.3: Total lowest-order hadronic cross section $\sigma_0(pp \to W^+ H + X)$ and corresponding relative electroweak correction δ ($\sqrt{s} = 14$ TeV).

M_H/GeV	$\sigma_0\|_{\alpha(0)}$/pb	$\delta\|_{\alpha(0)}$/%	$\sigma_0\|_{\alpha(M_Z^2)}$/pb	$\delta\|_{\alpha(M_Z^2)}$/%	$\sigma_0\|_{G_\mu}$/pb	$\delta\|_{G_\mu}$/%
80.00	2.299(1)	0.95(1)	2.595(1)	−11.56(1)	2.457(1)	−4.77(1)
100.00	1.232(1)	0.83(1)	1.392(1)	−11.68(1)	1.317(1)	−5.03(1)
120.00	0.7134(1)	0.76(1)	0.8058(1)	−11.77(1)	0.7630(1)	−5.22(1)
140.00	0.4381(1)	0.54(1)	0.4950(1)	−12.01(1)	0.4684(1)	−5.56(1)
170.00	0.2297(1)	0.37(1)	0.2595(1)	−12.18(1)	0.2456(1)	−5.88(1)
190.00	0.1563(1)	0.32(1)	0.1765(1)	−12.23(1)	0.1670(1)	−6.01(1)

Table 4.4: Total lowest-order hadronic cross section $\sigma_0(pp \to Z H + X)$ and corresponding relative electroweak correction δ ($\sqrt{s} = 14$ TeV).

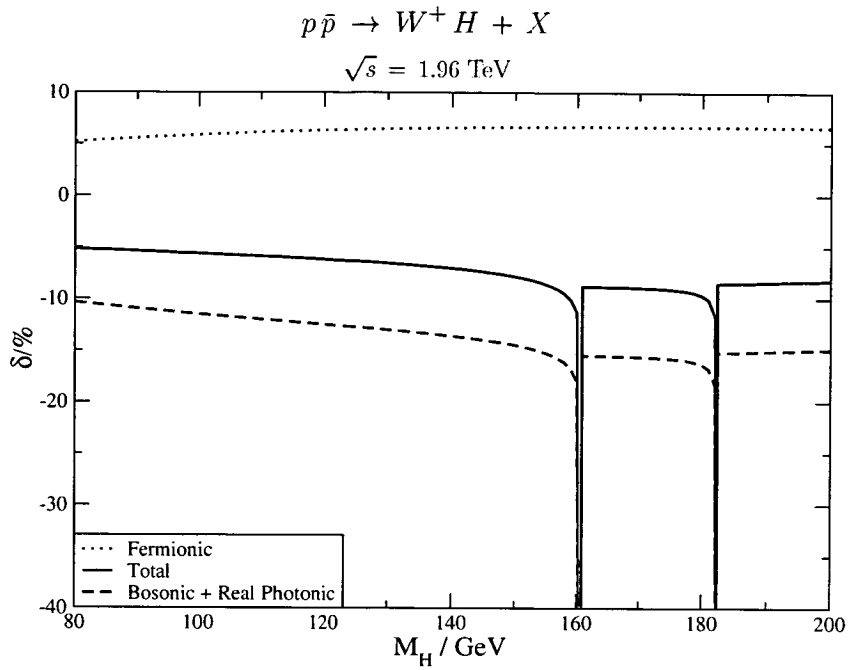

Figure 4.17: Different contributions to the relative electroweak correction δ in the G_μ-scheme as a function of the Higgs-boson mass for the total cross section $p\bar{p} \to W^+H+X$ ($\sqrt{s} = 1.96$ TeV).

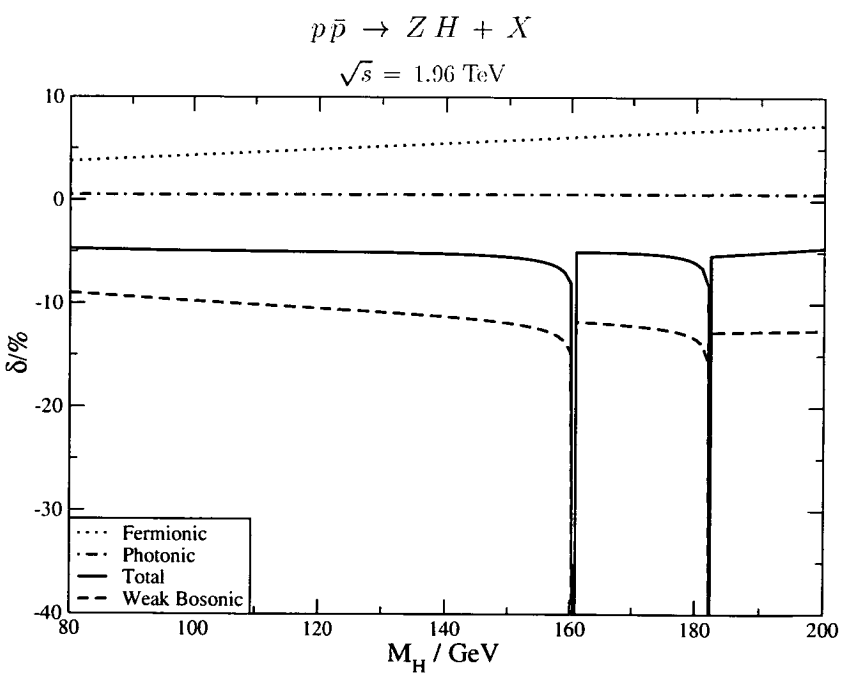

Figure 4.18: Different contributions to the relative electroweak correction δ in the G_μ-scheme as a function of the Higgs-boson mass for the total cross section $p\bar{p} \to ZH + X$ ($\sqrt{s} = 1.96$ TeV).

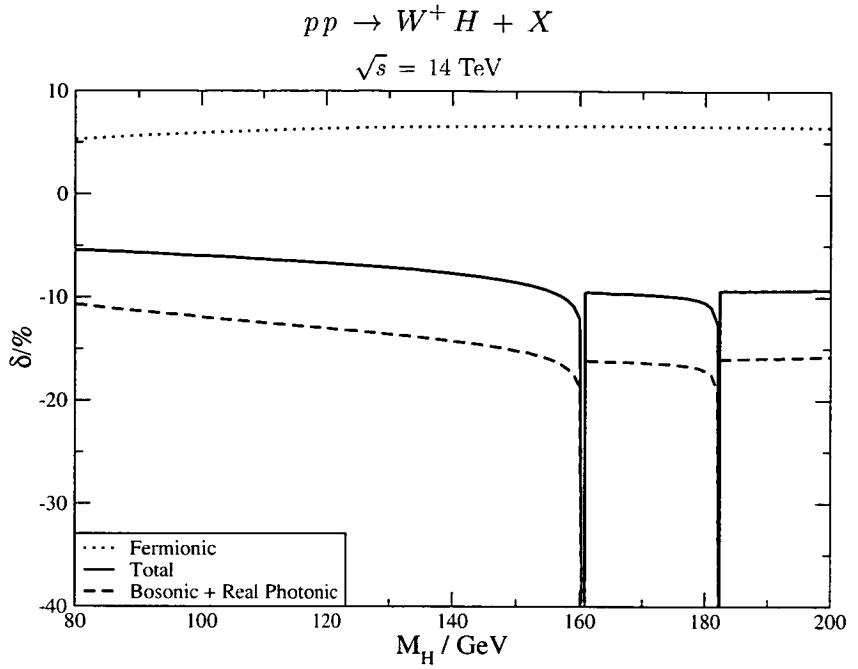

Figure 4.19: Different contributions to the relative electroweak correction δ in the G_μ-scheme as a function of the Higgs-boson mass for the total cross section $pp \to W^+H+X$ ($\sqrt{s} = 14$ TeV).

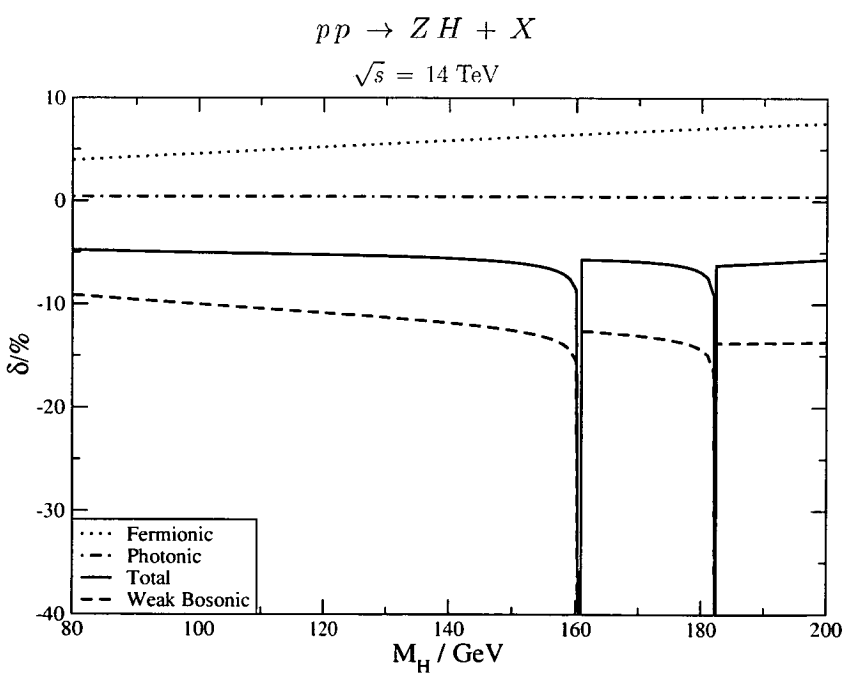

Figure 4.20: Different contributions to the relative electroweak correction δ in the G_μ-scheme as a function of the Higgs-boson mass for the total cross section $pp \to ZH + X$ ($\sqrt{s} = 14$ TeV).

$m_t \to \infty$ results, is set by the variable $\hat{s}$ which is not much smaller than but rather of the same order as m_t^2. For the ZH channel, $\delta^{\text{top}}_{u\bar{u}\to ZH}\big|_{G_\mu} \approx \delta^{\text{top}}_{d\bar{d}\to ZH}\big|_{G_\mu} \approx -1\%$ is obtained, again reflecting the failure of the heavy-top limit as a suitable approximation. Concerning the weak bosonic corrections, large negative contributions are expected in the high-energy limit owing to the occurrence of Sudakov logarithms of the form $-\alpha/\pi \log^2(\hat{s}/M_W^2)$. However, the relevant partonic CM energies $\sqrt{\hat{s}}$ are not yet large enough for the Sudakov logarithms to provide a good approximation for the full corrections.

4.4.3 The Cross Section at NLO

In this subsection the cross section prediction for associated WH and ZH production at the Tevatron and at the LHC, including the NLO electroweak and QCD corrections, is presented. The residual theoretical uncertainty due to scale variation and the parton distribution functions is quantified.

As explained in Sect. 4.2.2, different input parameter schemes can be chosen to evaluate the electroweak corrections. However, only when using the G_μ-scheme the large corrections associated with the running of $\alpha(Q^2)$ from $Q^2 = 0$ to the electroweak scale and those proportional to m_t^2/M_W^2 in the weak couplings are absorbed in the lowest order cross section. Note also that in the G_μ-scheme the results do not suffer from the uncertainties arising from the hadronic vacuum polarization at low energies. For these reasons this scheme is used in the following.

The total cross sections for the processes $p\bar{p}/pp \to W^\pm H + X$ (sum of W^+H and W^-H) and $p\bar{p}/pp \to ZH + X$ at the Tevatron and the LHC are displayed in Figs. 4.21–4.24. Representative results are listed in Tables 4.5–4.8. For the central renormalization and factorization scale $\mu = \mu_0 = \sqrt{s_{VH}}$ the NLO QCD corrections increase the LO cross section by typically 20–25%. As discussed in detail in Sect. 4.4.2, the NLO electroweak corrections are sizeable and decrease the cross section by 5–10% in the G_μ-scheme. The size of the $\mathcal{O}(\alpha_s)$ and $\mathcal{O}(\alpha)$ corrections does not depend strongly on the Higgs-boson mass.

The NLO prediction is very stable under variation of the QCD renormalization and factorization scales. Both scales have been varied independently in the range $\mu_0/5 < \mu < 5\mu_0$. For both the Tevatron and the LHC, the cross section increases

M_H/GeV	$\sigma_0\|_{G_\mu}$/pb	$\sigma_{\text{NLO}}^{\text{QCD}}$/pb	$\sigma_{\text{NLO}}^{\text{QCD+EW}}$/pb	$\sigma_{\text{NLO}}^{\text{QCD+EW}}$/pb	
				$\mu_R = 5\mu_0$ $\mu_F = 5\mu_0$	$\mu_R = \mu_0/5$ $\mu_F = \mu_0/5$
80.00	0.4117(1)	0.5616(2)	0.5404(2)	0.5033(1)	0.5838(1)
100.00	0.2056(1)	0.2801(1)	0.2685(1)	0.2482(1)	0.2911(1)
120.00	0.1106(1)	0.1504(1)	0.1436(1)	0.1318(1)	0.1562(1)
140.00	0.06297(1)	0.08536(1)	0.08092(1)	0.07377(1)	0.08833(1)
170.00	0.02921(1)	0.03940(1)	0.03679(1)	0.03318(1)	0.04037(1)
190.00	0.01821(1)	0.02446(1)	0.02294(1)	0.02056(1)	0.02525(1)

Table 4.5: Total cross section for $p\bar{p} \to W^{\pm}H + X$ (sum of W^+H and W^-H) at the Tevatron ($\sqrt{s} = 1.96$ TeV) in LO, NLO QCD, and including NLO QCD and electroweak corrections in the G_μ-scheme. The renormalization scale (μ_R) and the factorization scale (μ_F) have been set to the invariant mass of the Higgs–vector-boson pair, $\mu = \mu_0 = \sqrt{s_{VH}}$. CTEQ6L1 and CTEQ6M [85] parton distribution functions have been adopted at LO and $\mathcal{O}(\alpha_s)$, respectively. The last two columns show the minimal and maximal cross section prediction obtained from varying the QCD renormalization and factorization scales independently in the range $\mu_0/5 < \mu < 5\mu_0$.

M_H/GeV	$\sigma_0\|_{G_\mu}$/pb	$\sigma_{\text{NLO}}^{\text{QCD}}$/pb	$\sigma_{\text{NLO}}^{\text{QCD+EW}}$/pb	$\sigma_{\text{NLO}}^{\text{QCD+EW}}$/pb	
				$\mu_R = 5\mu_0$ $\mu_F = 5\mu_0$	$\mu_R = \mu_0/5$ $\mu_F = \mu_0/5$
80.00	0.2350(1)	0.3181(1)	0.3070(1)	0.2858(1)	0.3317(1)
100.00	0.1221(1)	0.1649(1)	0.1589(1)	0.1470(1)	0.1722(1)
120.00	0.06796(1)	0.09160(1)	0.08820(1)	0.08111(2)	0.09575(1)
140.00	0.03984(1)	0.05354(1)	0.05148(1)	0.04706(2)	0.05604(1)
170.00	0.01922(1)	0.02570(1)	0.02472(1)	0.02242(1)	0.02701(1)
190.00	0.01227(1)	0.01635(1)	0.01573(1)	0.01418(1)	0.01722(1)

Table 4.6: Total cross section for $p\bar{p} \to ZH+X$ at the Tevatron ($\sqrt{s} = 1.96$ TeV) in LO, NLO QCD, and including NLO QCD and electroweak corrections in the G_μ-scheme.

M_H/GeV	$\sigma_0\|_{G_\mu}$/pb	$\sigma_{\text{NLO}}^{\text{QCD}}$/pb	$\sigma_{\text{NLO}}^{\text{QCD+EW}}$/pb	$\sigma_{\text{NLO}}^{\text{QCD+EW}}$/pb	
				$\mu_R = 5\mu_0$ $\mu_F = \mu_0/5$	$\mu_R = \mu_0/5$ $\mu_F = 5\mu_0$
80.00	4.679(2)	5.676(2)	5.423(2)	4.875(2)	5.749(5)
100.00	2.462(1)	3.005(1)	2.859(1)	2.606(2)	3.033(2)
120.00	1.405(1)	1.726(1)	1.633(1)	1.505(1)	1.731(1)
140.00	0.8537(2)	1.054(1)	0.9892(3)	0.9204(3)	1.050(1)
170.00	0.4434(1)	0.5504(1)	0.5078(1)	0.4782(1)	0.5388(3)
190.00	0.3003(1)	0.3745(1)	0.3466(1)	0.3285(1)	0.3675(2)

Table 4.7: Total cross section for $pp \to W^{\pm}H + X$ at the LHC ($\sqrt{s} = 14$ TeV) in LO, NLO QCD, and including NLO QCD and electroweak corrections in the G_μ-scheme.

M_H/GeV	$\sigma_0\|_{G_\mu}$/pb	$\sigma_{\text{NLO}}^{\text{QCD}}$/pb	$\sigma_{\text{NLO}}^{\text{QCD+EW}}$/pb	$\sigma_{\text{NLO}}^{\text{QCD+EW}}$/pb	
				$\mu_R = 5\mu_0$ $\mu_F = \mu_0/5$	$\mu_R = \mu_0/5$ $\mu_F = 5\mu_0$
80.00	2.457(1)	2.974(1)	2.857(1)	2.578(2)	3.018(3)
100.00	1.317(1)	1.605(1)	1.539(1)	1.407(1)	1.629(1)
120.00	0.7630(1)	0.9346(3)	0.8947(3)	0.8271(2)	0.9462(6)
140.00	0.4684(2)	0.5768(2)	0.5508(2)	0.5138(1)	0.5830(3)
170.00	0.2456(1)	0.3045(1)	0.2900(1)	0.2736(1)	0.3068(2)
190.00	0.1670(1)	0.2078(1)	0.1978(1)	0.1879(1)	0.2094(1)

Table 4.8: Total cross section for $pp \to ZH + X$ at the LHC ($\sqrt{s} = 14$ TeV) in LO, NLO QCD, and including NLO QCD and electroweak corrections in the G_μ-scheme.

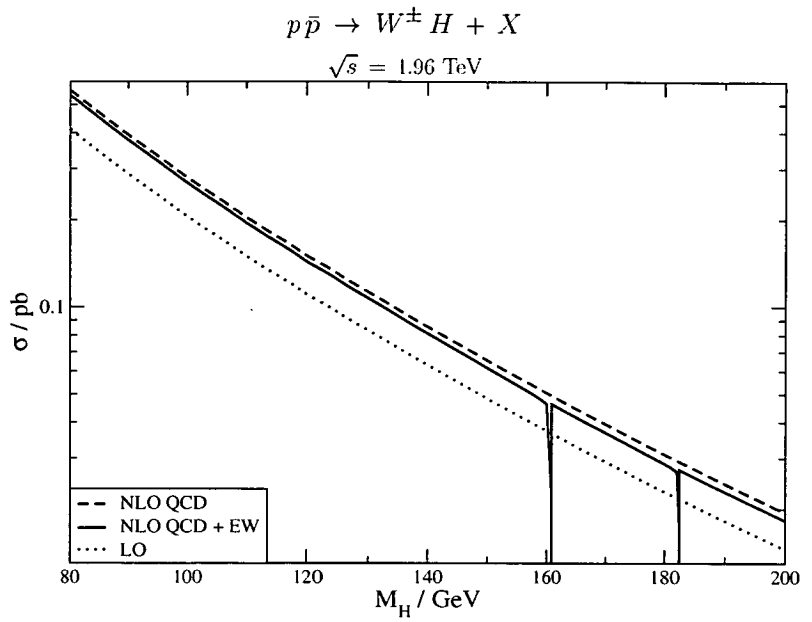

Figure 4.21: Total cross section for $p\bar{p} \to W^{\pm}H + X$ (sum of $W^{+}H$ and $W^{-}H$) at the Tevatron ($\sqrt{s} = 1.96$ TeV) in LO, NLO QCD, and including NLO QCD and electroweak corrections in the G_{μ}-scheme. The renormalization and factorization scales have been set to the invariant mass of the Higgs–vector-boson pair, $\mu = \sqrt{s_{VH}}$. CTEQ6L1 and CTEQ6M [85] parton distribution functions have been adopted at LO and $\mathcal{O}(\alpha_s)$, respectively.

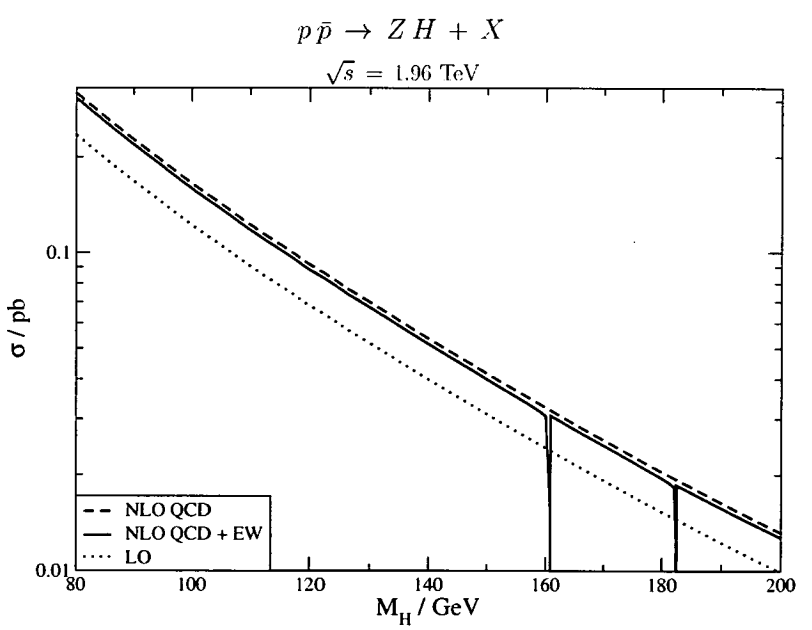

Figure 4.22: Total cross section for $p\bar{p} \to ZH + X$ at the Tevatron ($\sqrt{s} = 1.96$ TeV) in LO, NLO QCD, and including NLO QCD and electroweak corrections in the G_{μ}-scheme.

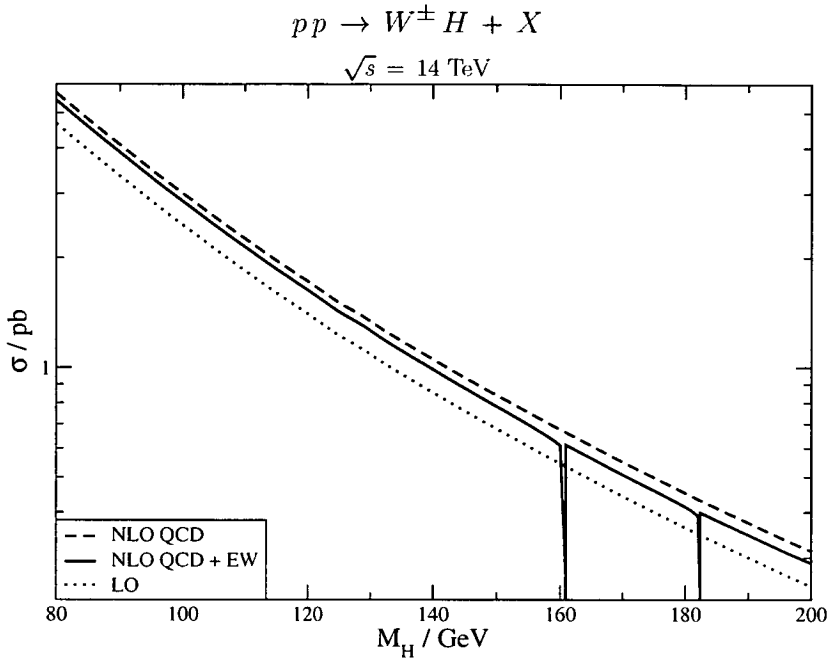

Figure 4.23: Total cross section for $pp \to W^{\pm}H + X$ at the LHC ($\sqrt{s} = 14$ TeV) in LO, NLO QCD, and including NLO QCD and electroweak corrections in the G_{μ}-scheme.

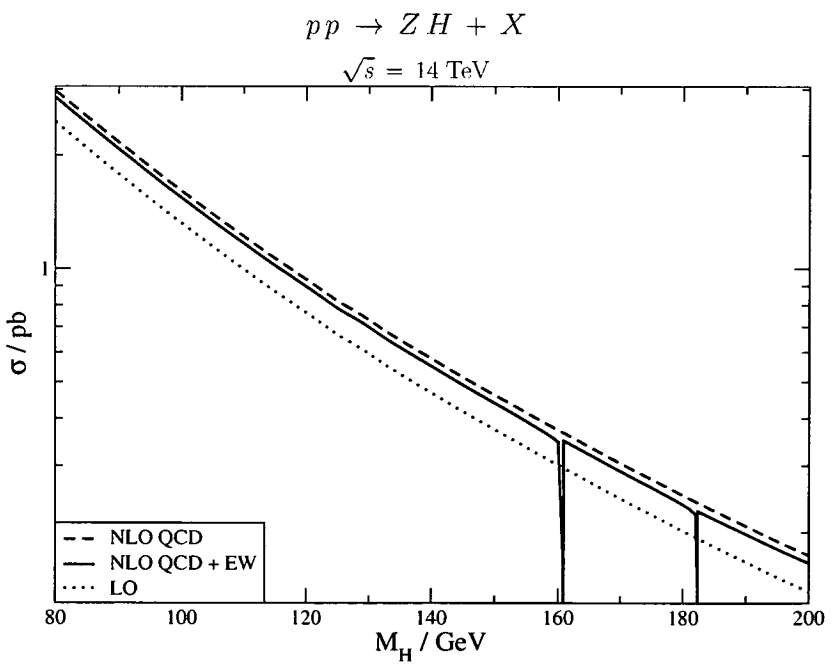

Figure 4.24: Total cross section for $pp \to ZH + X$ at the LHC ($\sqrt{s} = 14$ TeV) in LO, NLO QCD, and including NLO QCD and electroweak corrections in the G_{μ}-scheme.

M_H/GeV	CTEQ6M [85]	MRST2001 [89]
80.00	0.5404(2) ± 0.021	0.5448(2) ± 0.0097
100.00	0.2685(1) ± 0.011	0.2698(1) ± 0.0052
120.00	0.1436(1) ± 0.0060	0.1437(1) ± 0.0030
140.00	0.08092(1) ± 0.0035	0.08065(1) ± 0.0018
170.00	0.03679(1) ± 0.0017	0.03644(1) ± 0.00091
190.00	0.02294(1) ± 0.0011	0.02262(1) ± 0.00060

Table 4.9: Parton distribution function (PDF) uncertainties: Total cross section for $p\bar{p} \to W^{\pm}H + X$ at the Tevatron ($\sqrt{s} = 1.96$ TeV) including NLO QCD and electroweak corrections in the G_{μ}-scheme for different sets of parton distribution functions. The results include an estimate of the uncertainty due to the parametrization of the parton densities as obtained with the CTEQ6 [85] and MRST2001 [89] eigenvector sets (columns 2 and 3, respectively). The renormalization and the factorization scales have been set to the invariant mass of the Higgs–vector-boson pair, $\mu = \mu_0 = \sqrt{s_{VH}}$.

M_H/GeV	CTEQ6M [85]	MRST2001 [89]
80.00	0.3070(1) ± 0.012	0.3090(1) ± 0.0039
100.00	0.1589(1) ± 0.0064	0.1596(1) ± 0.0020
120.00	0.08820(1) ± 0.0036	0.08840(1) ± 0.0011
140.00	0.05148(1) ± 0.0021	0.05151(1) ± 0.00066
170.00	0.02472(1) ± 0.0010	0.02469(1) ± 0.00033
190.00	0.01573(1) ± 0.00068	0.01568(1) ± 0.00021

Table 4.10: PDF uncertainties: Total cross section for $p\bar{p} \to ZH + X$ at the Tevatron ($\sqrt{s} = 1.96$ TeV) including NLO QCD and electroweak corrections in the G_{μ}-scheme for different sets of parton distribution functions.

M_H/GeV	CTEQ6M [85]	MRST2001 [89]
80.00	5.423(2) ± 0.18	5.509(2) ± 0.071
100.00	2.859(1) ± 0.096	2.910(1) ± 0.035
120.00	1.633(1) ± 0.055	1.664(1) ± 0.021
140.00	0.9892(3) ± 0.034	1.010(1) ± 0.012
170.00	0.5078(1) ± 0.018	0.5193(1) ± 0.0063
190.00	0.3466(1) ± 0.012	0.3547(2) ± 0.0043

Table 4.11: PDF uncertainties: Total cross section for $pp \to W^{\pm}H + X$ at the LHC ($\sqrt{s} = 14$ TeV) including NLO QCD and electroweak corrections in the G_{μ}-scheme for different sets of parton distribution functions.

M_H/GeV	CTEQ6M [85]	MRST2001 [89]
80.00	2.857(1) ± 0.095	2.936(1) ± 0.036
100.00	1.539(1) ± 0.051	1.583(1) ± 0.019
120.00	0.8947(3) ± 0.030	0.9217(3) ± 0.011
140.00	0.5508(2) ± 0.019	0.5681(2) ± 0.0067
170.00	0.2900(1) ± 0.010	0.2994(1) ± 0.0036
190.00	0.1978(1) ± 0.0069	0.2045(1) ± 0.0025

Table 4.12: PDF uncertainties: Total cross section for $pp \to ZH + X$ at the LHC ($\sqrt{s} = 14$ TeV) including NLO QCD and electroweak corrections in the G_{μ}-scheme for different sets of parton distribution functions.

monotonically with decreasing renormalization scale. At the Tevatron, the maximal (minimal) cross section is obtained choosing both the renormalization and factorization scales small (large). At the LHC, in contrast, the maximal (minimal) cross section corresponds to choosing a large (small) factorization scale. From the numbers listed in Tables 4.5–4.8 one can conclude that the theoretical uncertainty introduced by varying the QCD scales in the range $\mu_0/5 < \mu < 5\mu_0$ is less than approximately 10%. It has been verified that the QED factorization-scale dependence of the $\mathcal{O}(\alpha)$-corrected cross section is below 1% and thus negligible compared to the other theoretical uncertainties. The QED scale dependence should be reduced further when using QED-improved parton densities.

The uncertainty in the cross-section prediction due to the error in the parametrization of the parton densities has also been studied. To this end the NLO cross section evaluated using the default CTEQ6 [85] parametrization with the cross section evaluated using the MRST2001 [89] parametrization have been compared. The results are collected in Tables 4.9–4.12. Both the CTEQ and MRST parametrizations include parton-distribution-error packages which provide a quantitative estimate of the corresponding uncertainties in the cross sections.[2] Using the parton-distribution-error packages and comparing the CTEQ and MRST2001 parametrizations, it was found that the uncertainty in predicting the processes $p\bar{p}/pp \to W^{\pm}H + X$ and $p\bar{p}/pp \to ZH + X$ at the Tevatron and the LHC due to the parametrization of the parton densities is less than approximately 5%.

4.5 Electroweak NLO and QCD NNLO Corrections

In this section the electroweak $\mathcal{O}(\alpha)$ corrections to Higgs boson production in association with a vector boson and the NNLO QCD corrections recently presented in ref. [57], are combined to obtain the most precise value currently available for this process cross section.

Beyond NLO, the QCD corrections to VH production differ from those to the Drell-Yan process by contributions where the Higgs boson couples to a heavy fermion loop.

[2] In addition, the MRST [90] parametrization allows to study the uncertainty of the NLO cross section due to the variation of α_s. For associated WH and ZH hadroproduction, the sensitivity of the theoretical prediction to the variation of α_s ($\alpha_s(M_Z^2) = 0.119 \pm 0.02$) turns out to be below 2%.

The impact of these additional terms is, however, expected to be small in general [62]. Moreover, for ZH production the one-loop-induced process $gg \to ZH$ contributes at next-to-next-to-leading order (NNLO). The NNLO corrections corresponding to the Drell-Yan mechanism as well as the $gg \to ZH$ contribution have been calculated in Ref. [57]. These NNLO corrections further increase the cross section by the order of 5–10%. Most important, a successive reduction of the renormalization and factorization scale dependence is observed when going from LO to NLO to NNLO.

The NNLO corrections to the Drell-Yan process $p\bar{p}/pp \to V^* + X$ consist of the following set of radiative corrections:

- two-loop corrections to $q\bar{q} \to V^*$, which have to be multiplied by the Born term,
- one-loop corrections to the processes $qg \to qV^*$ and $q\bar{q} \to gV^*$, which have to be multiplied by the tree-level gq and $q\bar{q}$ terms,
- tree-level contributions from $q\bar{q}, qq, qg, gg \to V^* + 2$ partons in all possible ways; the sums of these diagrams for a given initial and final state have to be squared and added.

These corrections have been calculated a decade ago in Ref. [92] and have recently been updated [94]. They represent a basic building block in the NNLO corrections to VH production. There are, however, two other sources of $\mathcal{O}(\alpha_s^2)$ corrections:

- irreducible two-loop boxes for $q\bar{q}' \to VH$ where the Higgs boson couples via heavy-quark loops to two gluons that are attached to the q line,
- the gluon–gluon-initiated mechanism $gg \to ZH$ [95] at one loop; it is mediated by closed quark loops which induce ggZ and $ggZH$ couplings and contributes only to ZH but not to WH production.

In Ref. [57] the NNLO corrections to VH production have been calculated from the results [94] on Drell-Yan production and completed by the (recalculated) contribution of $gg \to ZH$. The two-loop contributions with quark-loop-induced ggZ or ggH couplings are expected to be very small and have been neglected.

K-factors for the LO, NLO and NNLO QCD corrected cross section for WH production at the Fermilab Tevatron and the CERN LHC are depicted in figures 4.25 and 4.26

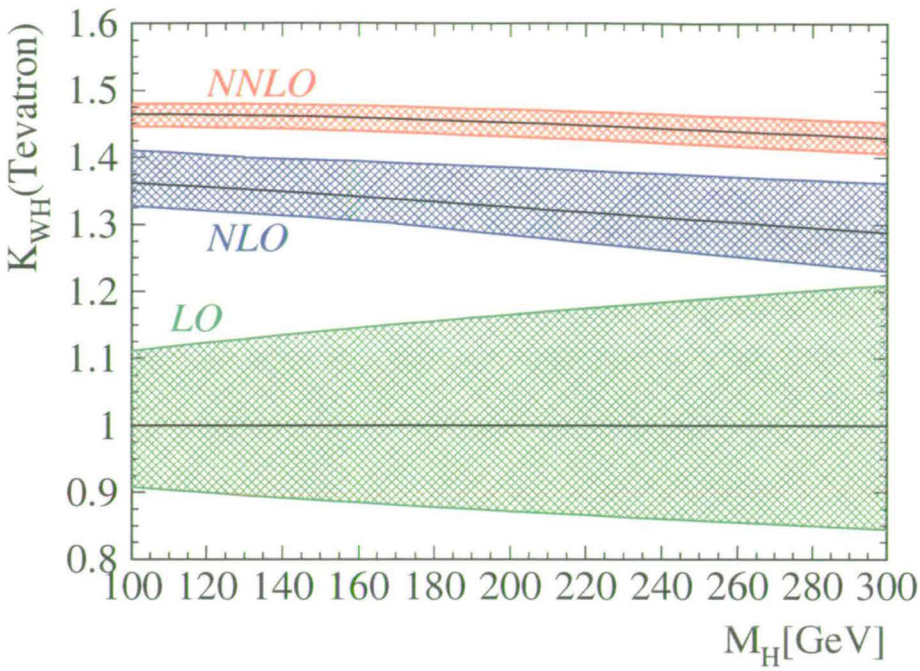

Figure 4.25: K-factor for the LO, NLO and NNLO QCD corrected cross section for $p\bar{p} \to WH + X$ at the Fermilab Tevatron. The shaded regions correspond to the uncertainty due to scale variation, as explained in the text (Taken from ref. [57].)

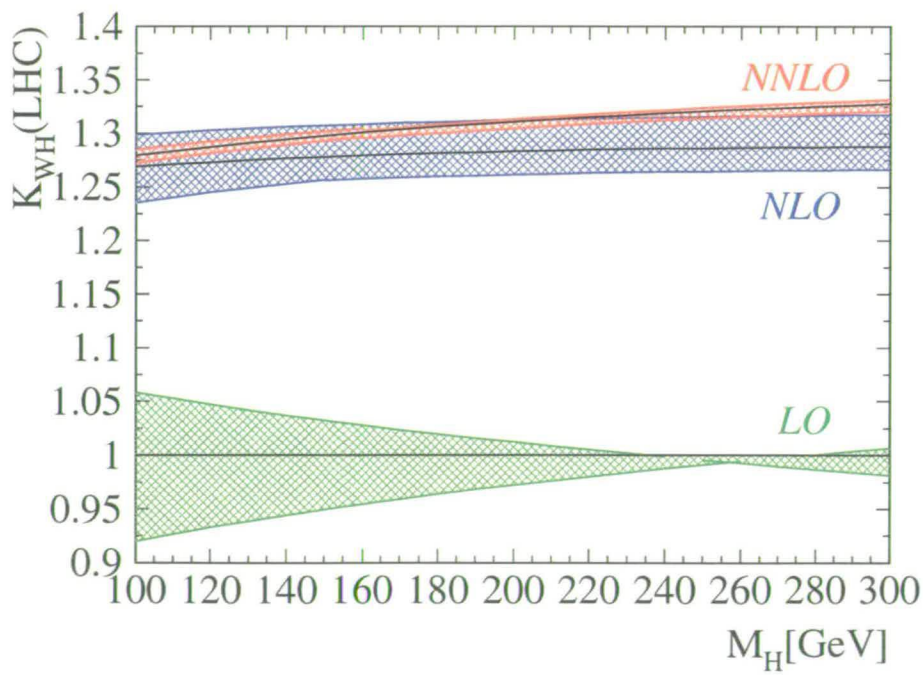

Figure 4.26: K-factor for the LO, NLO and NNLO QCD corrected cross section for $pp \to WH + X$ at the CERN LHC. The shaded regions correspond to the uncertainty due to scale variation, as explained in the text (Taken from ref. [57].)

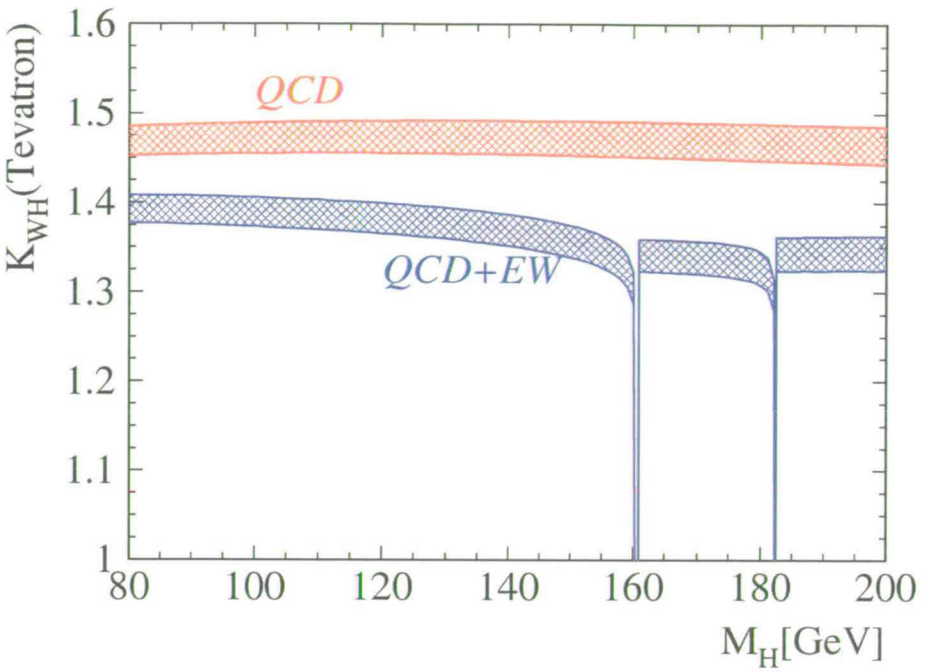

Figure 4.27: K-factor for the NNLO QCD corrected cross section, before and after including the NLO electroweak corrections, for $p\bar{p} \to WH+X$ at the Fermilab Tevatron. The shaded regions correspond to the uncertainty due to scale variation, as explained in the text.

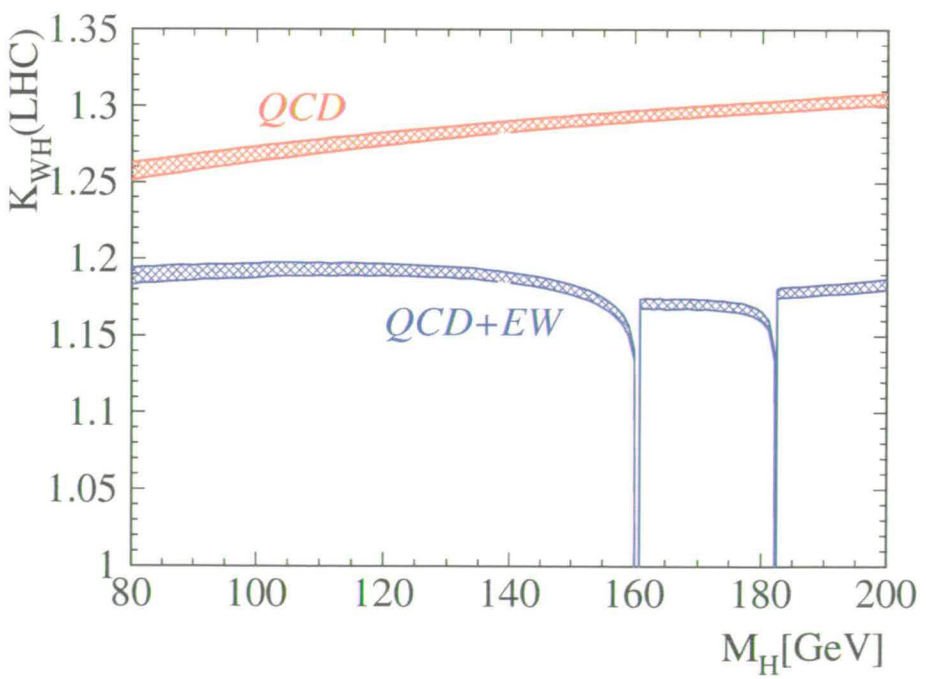

Figure 4.28: K-factor for the NNLO QCD corrected cross section, before and after including the NLO electroweak corrections, for $pp \to WH + X$ at the CERN LHC.

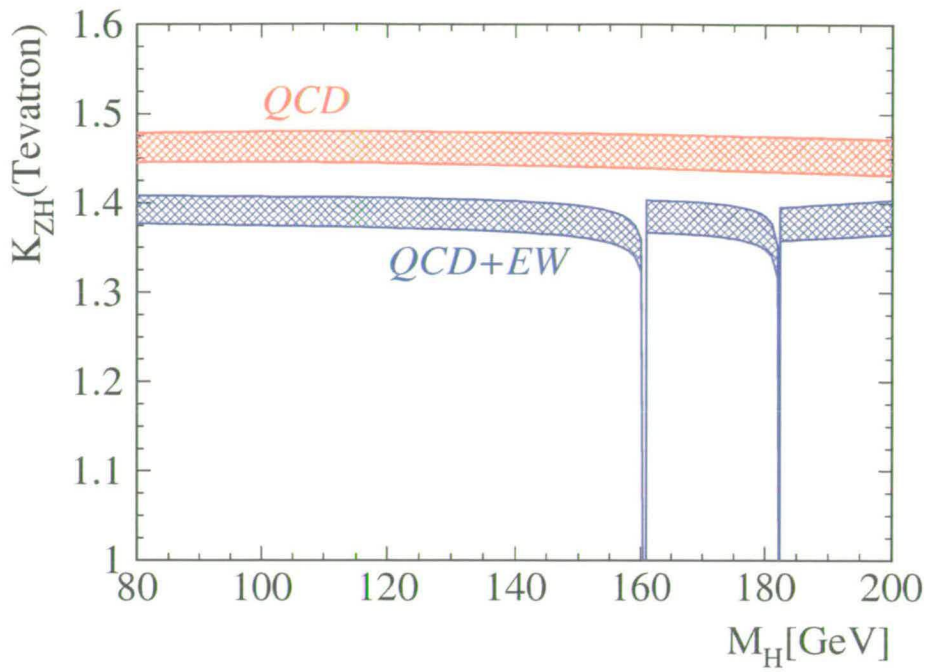

Figure 4.29: K-factor for the NNLO QCD corrected cross section, before and after including the NLO electroweak corrections, for $p\bar{p} \to ZH+X$ at the Fermilab Tevatron. The shaded regions correspond to the uncertainty due to scale variation, as explained in the text.

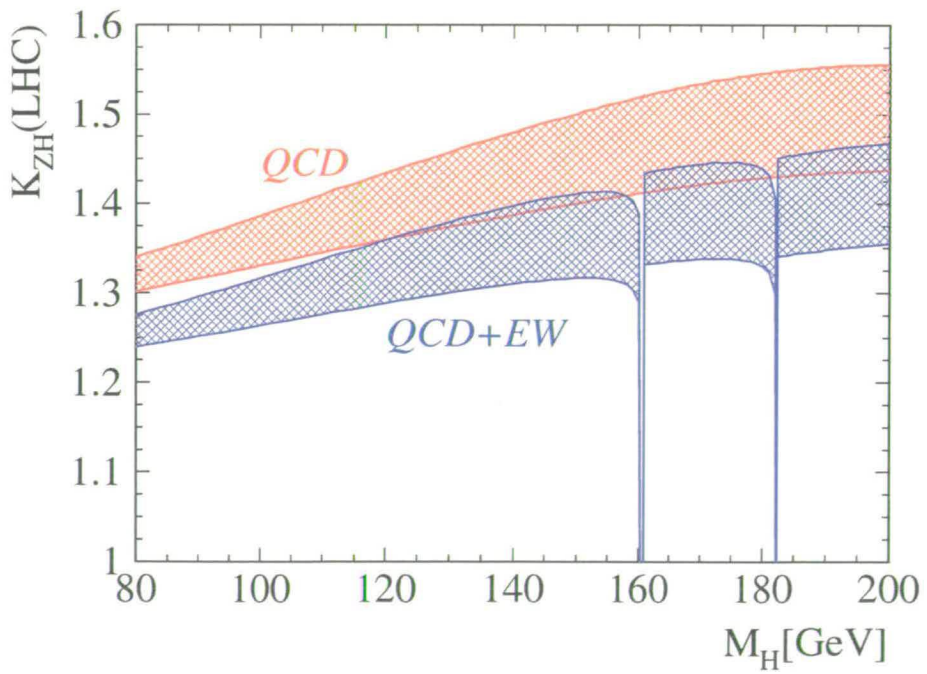

Figure 4.30: K-factor for the NNLO QCD corrected cross section, before and after including the NLO electroweak corrections, for $pp \to ZH + X$ at the CERN LHC.

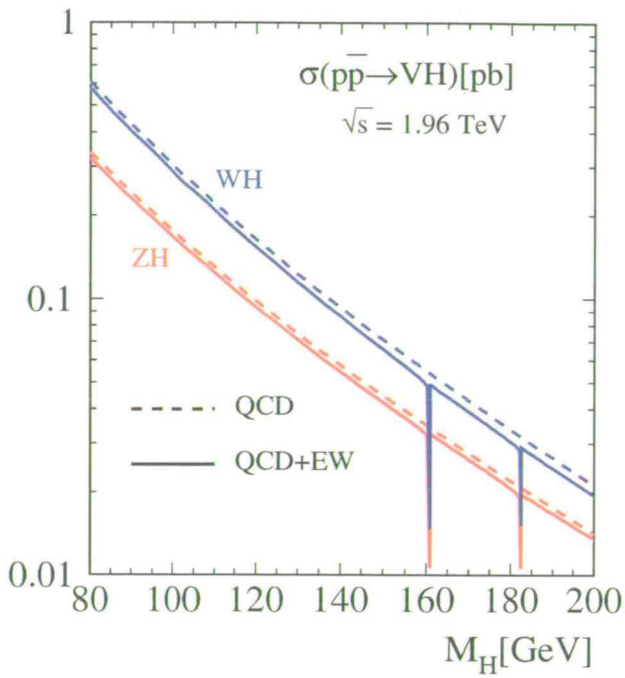

Figure 4.31: Total cross section, calculated in the G_μ scheme, for ZH and WH production at the Fermilab Tevatron, including NNLO QCD and electroweak corrections.

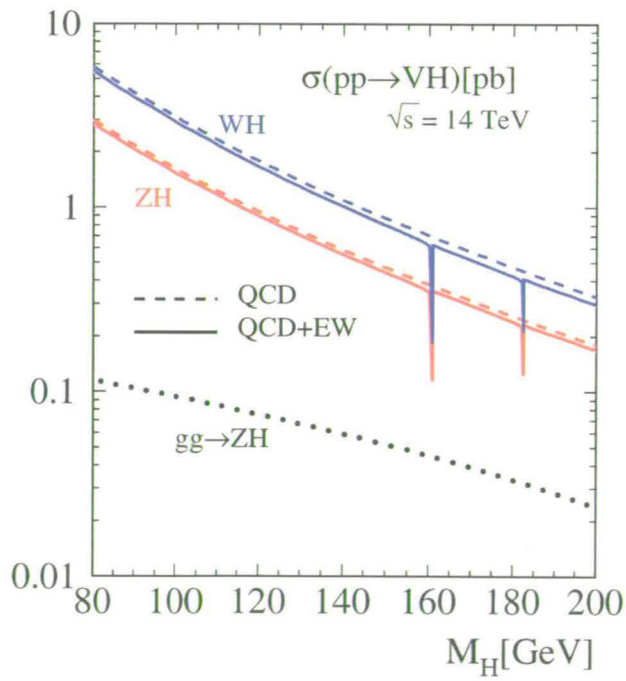

Figure 4.32: Total cross section, calculated in the G_μ scheme, for ZH and WH production at the CERN LHC, including NNLO QCD and electroweak corrections. The contribution from the process $gg \to ZH$ is also shown.

$M_H = 120\,\text{GeV}$	LO	NLO	NNLO
Tevatron	20%	7%	3%
LHC	10%	5%	2%

Table 4.13: VH production cross section uncertainty due to renormalization and factorization scale dependence for a Higgs boson of mass 120 GeV, in the LO, NLO and NNLO calculations.

(solid black lines). An important reduction on the factorization and renormalization scale dependence is observed when going from LO to NLO to NNLO. The uncertainty due to scale dependence can be calculated by fixing either the factorization scale μ_F or the renormalization scale μ_R to the central value $\mu_{R(F)} = \sqrt{s_{VH}}$, and varying the other scale in the range $\frac{1}{3}\sqrt{s_{VH}} \leq \mu_{F(R)} \leq 3\sqrt{s_{VH}}$. The effect of scale variation is included in the shaded areas of figures 4.25 and 4.26, while numerical values for the uncertainty at LO, NLO and NNLO, assuming a Higgs-boson mass of 120 GeV, are also shown in table 4.13. The uncertainty at the LHC in the NNLO calculation is only 2%.

At this level of accuracy electroweak $\mathcal{O}(\alpha)$ corrections become significant. The results obtained in this chapter have been combined with the cross section values from [57]. The results are depicted in figures 4.28–4.32. Figures 4.27 and 4.28 show the K-factors, after inclusion of electroweak and NNLO QCD corrections, for WH production[3] as a function of the Higgs boson mass at the Tevatron and the LHC. The shaded areas show the effect of factorization and renormalization scale dependence. In figures 4.29 and 4.30 the K-factors for ZH production as a function of M_H at the Tevatron and the LHC are shown. In this case the uncertainty band is larger than for WH production. This is due to the inclusion of the $gg \to ZH$ contribution, which is only relevant for ZH production. Finally, figures 4.31 and 4.32 show the total cross section for ZH and WH production at the Tevatron and the LHC, as a function of the Higgs-boson mass. At the LHC, due to the large gluon luminosity, the $gg \to ZH$ contribution is important, being of order 10% of the total cross section. This contribution is shown in figure 4.32.

[3] As in previous sections, WH production means the sum of the W^+H and W^-H production cross sections.

On the other hand, the contribution from this process at the Tevatron is negligible.

4.6 Conclusions

The electroweak $\mathcal{O}(\alpha)$ corrections to Higgs-boson production in association with W or Z bosons at hadron colliders have been calculated. In the G_μ-scheme these corrections decrease the theoretical prediction by up to 5–10%, depending in detail on the Higgs-boson mass[4]. The cross section prediction for associated WH and ZH production at the Tevatron and at the LHC, including the next-to-leading order electroweak and QCD corrections, have been updated. The remaining theoretical uncertainty has been studied by varying the renormalization and factorization scales and by taking into account the uncertainties in the parton distribution functions. It was found that the scale dependence is reduced to about 10% at next-to-leading order, while the uncertainty due to the parton densities is less than about 5%.

Finally, the electroweak $\mathcal{O}(\alpha)$ corrected cross section and the next-to-next-to-leading order QCD results from [57] were combined, yielding the most precise cross section prediction for a Higgs production process at hadron colliders. Both corrections are of order 5% – 10%, but have opposite signs. The theoretical uncertainties are dominated by scale dependence and parton distribution functions uncertainties, which are of order 3% and 5%, respectively. Calculating the ratios of the Higgs production cross section with the corresponding Drell-Yan-like vector boson production process $\sigma_{p\bar{p}/pp\to VH+X}/\sigma_{p\bar{p}/pp\to V+X}$ may further reduce these uncertainties.

[4]Choosing other input parameter schemes shifts the corrections by approx. ±5%. In the $\alpha(0)$-scheme the absolute value of the electroweak corrections is always less than 5%, while in the $\alpha(M_Z^2)$-scheme these corrections decrease the theoretical prediction by 10–15%.

Chapter 5

Gluon induced $W^{\pm}$ boson pair production

At the CERN LHC the process

$$g\,g \;\rightarrow\; H \;\rightarrow\; W^{+}W^{-} \;\rightarrow\; l\,\bar{\nu}_{l}\,\bar{l}'\,\nu_{l'} \tag{5.1}$$

will be one of the most important search channels for a light SM Higgs boson. After production via gluon fusion, the Higgs boson decays into a W-boson pair which then decays leptonically. The main background for this process is vector boson pair production. Contributions of the form $q\bar{q}' \rightarrow VV'$ to this background, including leptonic decays in the narrow width approximation, are known to next-to-leading order in α_s, see ref. [99]. The gluon induced, one loop contributions to on-shell vector boson pair production are also known, see for instance refs. [101]–[103].

There have been different analyses of the feasibility of the process in eq. 5.1 as a Higgs boson search tool, see refs. [104]–[112]. In particular in refs. [108]–[112] a set of experimental cuts has been proposed that allows for an important separation between signal and background. However, none of these analyses includes the contributions from gluon initiated processes to the background. Given the importance of the Higgs detection channel eq. 5.1, it is of utmost priority to have a detailed knowledge of all the backgrounds involved. This is of particular importance in the case of the gluon induced contributions. The reason for this is twofold. Firstly, at high energy hadron colliders in general, and the LHC in particular, the gluon luminosity is very high. Consequently, despite the fact that the parton cross section is suppressed by α_s^2 the total contribution

could be rather large. Secondly, the set of cuts introduced in [108]–[112] rely strongly on the fact that the signal is gluon induced while the background is originated from quarks in the initial states. The inclusion of the gluon induced background is very important in this analysis.

In this chapter the first calculation of the full analytic expression for the invariant amplitude for gluon induced off-shell $W^{+*}W^{-*}$ production is presented. The methods of refs. [72, 73] were used to algebraically reduce the amplitudes to a combination of rational functions of the kinematic invariants and a set of one-loop scalar integrals. This amplitude was used to calculate the gluon induced contribution to W-boson pair production at hadron colliders, including leptonic decays using the narrow width approximation. Finally, this contribution was also studied using the set of cuts proposed in [112].

This chapter is organized as follows: In Section 5.1.1 the latest analyses of the search channel eq. 5.1 are reviewed. The method suggested in refs. [108]–[112] to improve the signal to background ratio is explained, including the most important experimental cuts. In Section 5.1.2 a brief review of previous calculations of vector boson pair production at hadron colliders is given, with special emphasis on the calculations of the gluon initiated contributions. In Section 5.2 the analytic calculation of the invariant amplitudes for off-shell W-boson pair production via gluon fusion is explained in detail. In Section 5.3 these invariant amplitudes are used to calculate the cross section for off-shell W-boson pair production with leptonic decays. In Section 5.4 the case of massless quarks circulating the loops is analysed. In Section 5.5 the numerical evaluation method is explained, and numerical values for the cross sections are presented in Section 5.5.4, where the effect of the experimental cuts proposed to enhance the signal eq. 5.1 is also studied. Finally, the conclusion are presented in Section 5.6.

5.1 Introduction

5.1.1 Searching for a SM Higgs with $155\,\mathrm{GeV} < M_H < 180\,\mathrm{GeV}$

The CERN LHC is considered to be the most promising Higgs boson discovery machine, and the different experiments are expected to be able to probe the Higgs boson mass region in the range $100\,\mathrm{GeV} - 1\,\mathrm{TeV}$ [15, 16]. In Section 3.4.2 the different Higgs boson

discovery channels at the CERN LHC have been reviewed. It was shown that the Higgs boson search is usually split into three mass regions, namely:

1. $90\,\text{GeV} < M_H < 130\,\text{GeV}$: The highest significance detection channel is given by the process $gg \to H \to \gamma\gamma$, where a narrow mass peak would be observed. As mentioned in Section 3.4.2, W-boson fusion also plays an important role in this mass region.

2. $130\,\text{GeV} < M_H < 2M_Z$: In this mass range, assuming excellent energy and momentum measurements of the leptonic decay products, a mass peak from the channel $H \to ZZ^* \to 2l^+2l^-$ can be obtained.

3. $2M_Z < M_H < 800\,\text{GeV}$: A narrow mass peak can be obtained using the detection channel $H \to ZZ \to 2l^+2l^-$, which allows Higgs boson detection with a high statistical significance.

Within the mass range 2 above, there is a problematic region, though. The Standard Model Higgs boson, in the mass range $155\,\text{GeV} < M_H < 180\,\text{GeV}$, decays with a branching ratio of almost one to a pair of on-shell W bosons, as can be seen in figure 3.5 in Section 3.2. Consequently, if the four lepton signal is to be used, an integrated luminosity of the order of $100\,\text{fb}^{-1}$ is needed to obtain a sizeable significance, see figure 3.11. More important, the W-boson pair channel can not be used, unless further analysis is carried out. The reason for this is that the typical mass peaks of other Higgs detection channels are not present in this case, as the W-boson pair decays leptonically and the neutrinos carry away missing energy and momenta.

Early analyses of the use of the search channel eq. 5.1 as a possible SM Higgs discovery tool can be found in refs. [104, 105]. Although these studies do not take into account W-boson pair spin-angle correlation in their proposed experimental cuts, they agree that this detection channel should provide a reasonable possibility of Higgs boson detection. In refs. [108, 109] a new method for detecting a SM Higgs boson with mass in the range $155\,\text{GeV} - 180\,\text{GeV}$ was proposed. The Higgs boson decay modes

$$H \to W^+W^- \to (l^+\nu)(l'^-\bar{\nu}'), \tag{5.2}$$

with

$$l, l' = e, \mu, \tau(\to l\nu\bar{\nu}),$$

were considered. The final state of a Higgs production event was defined to be two charged leptons and missing energy. Improvements with respect to the analyses in refs. [104, 105] include: considering the contribution where the W-bosons may decay into τ leptons, which then decay leptonically, and the contribution of the process $gg \to Wtb$. In this analysis the PYTHIA[113] Monte Carlo program was used, including hadronization in the results. On the other hand, no K-factors were taken into account, as the NLO corrections for all the studied processes were not known at the time. However, it was argued that these corrections would improve the signal significance.

In order to compensate for the lack of a narrow mass peak, the significance is increased applying a set of signal-enhancing experimental cuts[108]. These cuts can be divided into two subsets. The first subset, similar to the cuts proposed in refs [104, 105], involves selecting relatively central events with two identified oppositely charged leptons, with large missing energy due to the two neutrinos.

1. Both leptons should have a minimum transverse momentum of 10 GeV, and their pseudorapidity should be $|\eta| < 2$ GeV.

2. The electromagnetic and hadronic energy in a cone with half angle 20° around each lepton should be less than 5 GeV.

3. At least one lepton should have transverse momenta 20 GeV $< p_T$.

4. The jet veto 20 GeV $< p_T^{\text{jet}}$ and $|\eta^{\text{jet}}| < 2.4$ GeV is applied.

5. The invariant mass of the dilepton system should be $M_{ll} < 80$ GeV and the missing transverse momentum $\not{p}_T(ll) > 20$ GeV.

6. The transverse opening angle between leptons should satisfy $\phi_\perp(ll) < 135°$.

These cuts select mostly events with $W^+W^- + X$, the most important background coming from the contribution $q\bar{q} \to W^+W^- \to l^-\bar{\nu}_l l'^+\nu'_l$. Note that the first two cuts select two isolated leptons according to Atlas and CMS capabilities.

The second subset is responsible for differentiating between $W^+W^- + X$ events coming from the background and signal. These cuts take advantage of the spin angle correlation of the W-boson pair coming from the Higgs-boson decay and the relative boost of the background with respect to the signal. The cuts can be summarized as follows:

7. The dilepton system polar angle θ_{ll} must satisfy $\cos(\theta_{ll}) < 0.8$

8. The transverse opening angle must satisfy $10° < \phi_{\perp}(ll) < 45°$

9. The estimated W-boson pair mass should be $M^{*}_{WW} > 140\,\mathrm{GeV}$

10. The opening angle θ^{*} between the lepton with the largest p_T boosted to the dilepton rest frame and the momentum vector of the dilepton system must satisfy $0 < \cos(\theta^{*}) < 0.3$

Cut number 7 is based on the fact that the signal events are more central than the background. This is a result of the different peak structure of the parton distribution functions. Once the parton cross section $\hat{\sigma}$ for a given process is calculated, it must be convoluted with the parton distribution functions $f_i(x)$ to obtain the hadron cross section σ:

$$\sigma = \int dx_1 dx_2 f_1(x_1) f_2(x_2) \hat{\sigma}(x_1, x_2)\,,$$

where x_i is the proton momentum fraction carried away by a parton. The momentum fractions satisfy $x_1\, x_2\, s = \hat{s}$. In the case of the signal $\hat{s} = M_H$, while for the background $\hat{s} = M_{VV}$, the invariant mass of the vector boson pair. In the mass region of interest $\hat{s}/s \sim 10^{-4}$. In figure 5.1 the product $f_1(x_1) f_2(x_2)$ is plotted for a fixed $\hat{s}/s$ value, as a function of x_1, for different parton sets. It can be seen that the distribution functions product corresponding to $q\bar{q}$ pairs has a maximum at approximately $x_1 = 0.1$. On the other hand, the product of gluon distribution functions has a maximum at approximately $x_1 = 0.01$. Given x_1 one can obtain x_2 and the partons centre-of-mass velocity v in the laboratory frame[1]:

$$\begin{aligned} x_2 &= \frac{1}{x_1}\frac{\hat{s}}{s}\,, \\ v &= \frac{|x_1 - x_2|}{x_1 + x_2}\,. \end{aligned}$$

Then, the $f_q f_{\bar{q}}$ maximum occurs at $v = 0.98$, while the $f_g f_g$ maximum occurs at $v = 0$. This means that the W-boson pair coming from quarks in the initial state, the background, will be mostly emitted in the beam direction. As the detectors will trigger on the final leptons, it is sensible to introduce a cut that will reject events with leptons folded in the beam direction.

[1] In this case the lab. frame is the initial hadrons centre-of-mass frame.

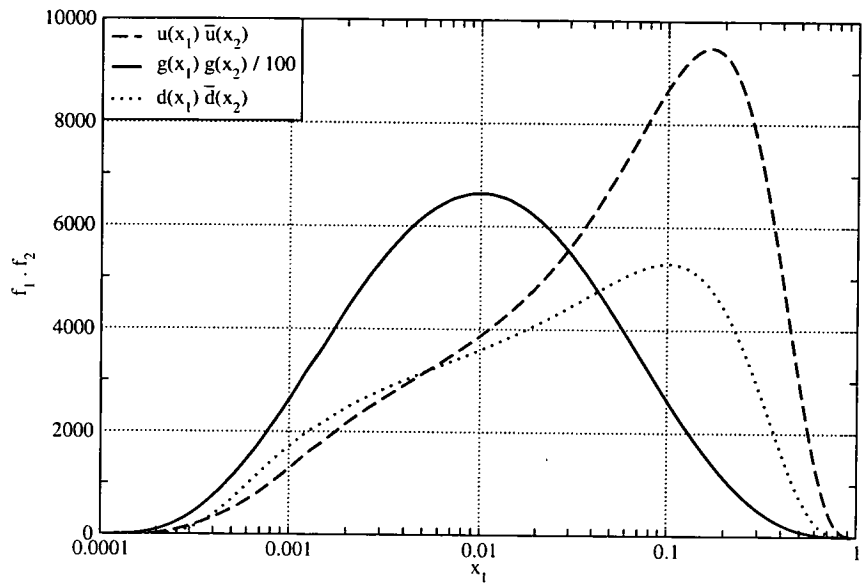

Figure 5.1: Parton distribution functions products as a function of parton momentum fraction. The CTQ6M[85] set of parton distribution functions was used, with a scale $Q = 100\,\text{GeV}$. It was assumed that $x_1\ x_2 = 10^{-4}$.

Cut number 8 uses the spin angle correlation between the W-boson pair coming from the Higgs boson decay. The use of the spin correlation between both W-bosons as a discriminating tool in Higgs boson searches has been mentioned in [114]. As the W-bosons originate from a Higgs boson (scalar particle) decay, they must have opposite spin orientations. Then, the W-bosons must be either both transversely or both longitudinally polarized. For transversely polarized W-bosons the l^- lepton is emitted opposite to the W^- spin, while the right-handed l^+ is emitted along the W^+ spin. As the W-bosons have opposite spin orientations, the leptons must be emitted with a small opening angle. For longitudinally polarized gauge bosons it can be shown[104] that the leptons are emitted perpendicularly to the W-bosons, in opposite directions. This means that leptons originated from the signal are emitted with a small opening angle. On the other hand leptons emitted in background processes are distributed more or less symmetrically.

In ref. [110] an update to the results of refs. [108, 109] can be found. More background processes were included and the latest Higgs production cross section estimates

were used in this analysis. This extended the mass range over which the search method is valid to 120 GeV – 400 GeV. More importantly, it was recognized that there exists a jacobian peak-like structure on the leptons transverse momenta (p_T) distribution, highly dependent on the Higgs boson mass. An improvement of the signal to background ratio was obtained by updating the original set of cuts and imposing further cuts on the leptons p_T spectra.

An update to the method presented in refs. [108]–[110] for Higgs-boson detection via the process in eq. 5.2 has been recently published in [112]. Event rates obtained with the PYTHIA Monte Carlo program were reweighted with the most up-to-date theoretical predictions for the Higgs signal p_T spectrum and for the non-resonant W-boson pair production, using a technique known as "effective" K-factor calculations. After taking into account higher-order QCD corrections the discovery potential for the channel 5.2 was found to be significantly increased. The integrated luminosity needed for a SM Higgs boson discovery with five standard deviations of statistical significance was found to be $\sim 0.4\text{fb}^{-1}$, provided the systematic uncertainties can be controlled better than about 10% – 20%. The following is the updated set of experimental cuts:

1. Both leptons should have a minimum transverse momentum 20 GeV $< p_T$ and a maximum pseudorapidity $|\eta| < 2$ GeV.

2. Lepton isolation cut: the sum of transverse energy from detectable particles inside a cone of size $\Delta R < 0.5$ around the lepton direction should be less than 10% of the lepton energy. The invariant mass of all the particles inside the cone should be less than 2 GeV, and only one extra particle is allowed inside a cone of $\Delta R < 0.15$.

3. The dilepton invariant mass should be $M_{ll} < 80$ GeV.

4. The missing transverse momentum should satisfy 20 GeV $< \not{p}_T(ll)$.

5. The transverse opening angle between leptons should be $\phi_\perp(ll) < 135°$.

6. The transverse opening angle of the dilepton system must satisfy $\phi_\perp(ll) < 45°$ and the dilepton system invariant mass should be $M_{ll} < 35$ GeV.

7. The jet veto 20 GeV $< p_T^{\text{jet}}$ and $|\eta^{\text{jet}}| < 4.5$ is applied.

8. The p_T spectrum of the charged leptons is exploited. On table 5.1 the lepton spectra cuts are shown as a function of the Higgs boson mass. In this table $p_{T\text{min}}$ and $p_{T\text{max}}$ denote the largest and smallest lepton transverse momenta, respectively.

M_H	$p_{T\text{min}}$ cut	$p_{T\text{max}}$ cut
165 GeV	25 GeV $< p_{T\text{min}}$	35 GeV $< p_{T\text{max}} <$ 50 GeV
140 GeV	20 GeV $< p_{T\text{min}}$	20 GeV $< p_{T\text{max}}$
180 GeV	25 GeV $< p_{T\text{min}}$	45 GeV $< p_{T\text{max}}$

Table 5.1: Leptons spectra cuts from ref. [112]

5.1.2 Vector Boson pair Production at Hadron Colliders

Parton processes contributing to vector boson pair production at hadron colliders can be divided into two main categories: quark induced and gluon induced processes. The one loop QCD corrected helicity amplitudes for the processes $q\bar{q} \to W^+W^-$, ZZ, $W^{\pm}Z$, $W^{\pm}\gamma$, $Z\gamma$ and tree-level amplitudes with an additional gluon radiated off the quark line were presented in ref. [99], where vector bosons leptonic decays were also taken into account. These results allowed the calculation of the next-to-leading order, in α_s, cross section for electroweak vector boson pair production at hadron colliders, presented in ref. [100]. These calculations included the vector bosons' leptonic decays in the narrow-width approximation, retaining all the spin-angle correlation information. In ref. [107] the amplitudes of [99] were used for the calculation of the cross section of hadronic production of vector boson pairs, including all spin correlations in the bosons leptonic decays. These results were obtained with a new Monte Carlo program: MCFM. This calculation goes beyond [100] in that the authors include single resonant diagrams when taking into account the vector bosons leptonic decays. As will be explained in Section 5.3, single-resonant diagrams are needed to maintain gauge invariance. A detailed study of the $H \to W^*W^*$ signal at the Fermilab TEVATRON can be found in ref. [106], in which the PYTHIA Monte Carlo program was used interfaced with a detector simulator. For the dilepton plus missing transverse energy signal they implemented a set of cuts

that included the cuts proposed in ref. [109].

The gluon fusion processes involve the production of vector bosons through one-loop diagrams, and as a result the cross section is suppressed by a factor α_s^2. This is the reason why there has not been as much thorough research in this process, as in processes with quarks in the initial state. The imaginary part of the $gg \to ZZ$ longitudinal amplitude was first evaluated in ref. [115]. The first complete $gg \to ZZ$ calculation can be found in ref. [101]. Using the technique described in ref. [73] the contribution to $pp \to ZZ$ from $gg \to ZZ$ was calculated. Values for the cross section as a function of the invariant mass of the Z-boson pair were obtained using the rapidity cut $|y_Z| < 2.5$. The results were compared with the $q\bar{q} \to ZZ$ contribution cross section. It was found that for low invariant mass and small top-quark mass the gluon contributions are larger than the quark antiquark contributions to $pp \to ZZ$, a behaviour already seen in other processes, eg. [116], where $gg \to \gamma\gamma$ was studied. In ref. [117] the $gg \to ZZ$ contribution to $pp \to ZZ$, including gluon-fusion Higgs production diagrams, was calculated. This result was combined with the contributions from $q\bar{q} \to ZZ$, $qq \to W^+W^-qq \to ZZqq$ and $qq \to ZZqq \to ZZqq$ taken from [118], obtaining the total Higgs signal and background cross section from $pp \to ZZ + X$ processes. The interference terms between the Higgs-boson signal and the $gg \to ZZ$ background were also studied. It was found that, although a mass peak was observed for the Higgs boson signal, the number of events above background was small.

Z-boson pair production at hadron colliders through gluon fusion via internal quark loops of arbitrary mass, including processes involving a Higgs boson, was studied in refs. [103, 119]. The calculation was done analytically using the methods of [73] to algebraically reduce the invariant amplitudes to the set of one-loop scalar integrals described in [72]. This algebraic reduction allowed better control of numerical instabilities found in [101, 117]. The invariant mass distribution of Z-boson pairs, with and without a Higgs boson, was studied for different centre-of-mass energies and different top quark masses. The result was compared to the $qq \to ZZ$ contributions and it was found that this latest contributions are dominant: the $gg \to ZZ/q\bar{q} \to ZZ$ ratio was found to be $35-45\%$ at $\sqrt{s} = 16\,\text{TeV}$. A detailed study of the interference between the Higgs production signal and the gluon fusion background showed that signal and background interfere destructively for Z-boson pair invariant mass larger than the Higgs

mass. These two results are opposed to findings in refs. [117, 101]. Finally, using the $gg \to ZZ$ result the contribution for $gg \to WW$ in the case of massless degenerate quarks was calculated. In this limit, the two contributions are related by a simple change in the coupling constant.

Ref. [102] is the first complete calculation of the contribution to $pp \to W^+W^- + X$ from the gluon fusion process $gg \to W^+W^-$ including the top-bottom massive quark loop. Invariant mass distributions were calculated with and without a Higgs boson. Different Higgs boson masses were used and the appearance of an invariant mass distribution peak was observed. Contributions from different W-boson polarization states were also analysed for different values of the top quark mass and it was concluded that W^+W^- on-shell pair production from gluon fusion could be used as a good Higgs boson search channel.

More recently, gluon induced production of off-shell Z-boson pairs with subsequent decay into charged lepton pairs was studied in ref. [120], where it was found that, in the lower half of the intermediate Higgs boson mass region, the background from gluon and quark induced processes with Z-boson pairs as intermediate states is not severe. Gluon induced gauge boson pair production has also been studied in refs. [121, 122], where the contributions of the partonic processes $gg \to WZq\bar{q}$, $gg \to W\gamma q\bar{q}$, $gg \to Z\gamma q\bar{q}$ and $gg \to Z\gamma$ to WZ, $W\gamma$ and $Z\gamma$ hadronic production were calculated. Using the narrow width approximation the leptonic decays of W and Z bosons have been taken into account. The gluon induced process through one loop boxes was recalculated and found to be smaller than the contributions calculated in refs. [103, 119], something which was attributed to the use of different parton distribution functions. In all cases it was found that the gluon induced contributions to hadronic production of gauge boson pairs are not very large.

5.2 The $gg \to W^{+*}W^{-*}$ Invariant Amplitude

The invariant amplitude for gluon-induced off-shell W-boson pair production

$$g(p_1)\, g(p_2) \;\to\; W^{-*}(p_3)\, W^{+*}(p_4) \tag{5.3}$$

has been calculated. This amplitude was used to calculate the amplitudes for the processes

$$g(p_1)\, g(p_2) \;\rightarrow\; W^{-*}(p_3)\, W^{+*}(p_4) \;\rightarrow\; l(p_5)\, \bar{\nu}_l(p_6)\, \bar{l}'(p_7)\, \nu_{l'}(p_8) \tag{5.4}$$

$$g(p_1)\, g(p_2) \;\rightarrow\; W^{-}(p_3)\, W^{+}(p_4)\,. \tag{5.5}$$

All the calculations were done in the unitary gauge, to avoid having to include the unphysical Goldstone bosons. The Feynman diagrams contributing to the amplitude 5.3 are shown in figure 5.2. As will be explained in detail in Section 5.3, if the process in eq 5.4 is being calculated, the double-resonant diagrams of figure 5.2 do not form a gauge invariant set and extra single-resonant diagrams must be included.

The invariant amplitude, without polarization vectors for the external particles, can be written as

$$\begin{aligned}\mathcal{M}^{\mu_1\mu_2\mu_3\mu_4}(p_1,p_2,p_3,p_4;m_u,m_d) \;&=\; \sum_{i=1}^{6} \mathcal{D}^{\mu_1\mu_2\mu_3\mu_4}_{\mathrm{box_i}}(p_1,p_2,p_3,p_4;m_u,m_d) \\ &\quad + \sum_{i=1}^{12} \mathcal{D}^{\mu_1\mu_2\mu_3\mu_4}_{\mathrm{tri_i}}(p_1,p_2,p_3,p_4;m_f) \quad , \; f=u,d \;,\end{aligned} \tag{5.6}$$

where $\mathcal{D}_{\mathrm{box_i}}$ and $\mathcal{D}_{\mathrm{tri_i}}$ denote the contributions from the i^{th} box and triangle diagrams, respectively. $m_{u,d}$ are the masses of up- and down-type quarks and the tensor index μ_i corresponds to the leg carrying a momentum p_i. Explicitly, the $\mathrm{box_1}$ diagram contribution can be written as

$$\mathcal{D}^{\mu_1\mu_2\mu_3\mu_4}_{\mathrm{box_1}}(p_1,p_2,p_3,p_4;m_u,m_d) = \frac{\mu^{2\epsilon}}{(2\pi)^{4-2\epsilon}} \int d^{4-2\epsilon}k\; \tilde{\mathcal{D}}^{\mu_1\mu_2\mu_3\mu_4}_{\mathrm{box_1}}(p_1,p_2,p_3,p_4;m_u,m_d)\,,$$

with

$$\begin{aligned}&\tilde{\mathcal{D}}^{\mu_1\mu_2\mu_3\mu_4}_{\mathrm{box_1}}(p_1,p_2,p_3,p_4;m_u,m_d) = \\ &= \mathrm{Tr}\left\{ \frac{i}{\not{k}-m_u}\gamma^{\mu_3}\omega^{-} \frac{i}{\not{k}+\not{p}_3-m_d}\gamma^{\mu_1} \frac{i}{\not{k}+\not{p}_3-\not{p}_1-m_d}\gamma^{\mu_2} \frac{i}{\not{k}-\not{p}_4-m_d}\gamma^{\mu_4}\omega^{-} \right\} \\ &= \frac{\mathrm{Tr}\left\{(\not{k}+m_u)\gamma^{\mu_3}\omega^{-}(\not{k}+\not{p}_3+m_d)\gamma^{\mu_1}(\not{k}+\not{p}_3-\not{p}_1+m_d)\gamma^{\mu_2}(\not{k}-\not{p}_4+m_d)\gamma^{\mu_4}\omega^{-}\right\}}{(k^2-m_u^2)\left((k+p_3)^2-m_d^2\right)\left((k+p_3-p_1)^2-m_d^2\right)\left((k-p_4)^2-m_d^2\right)}\,.\end{aligned} \tag{5.7}$$

In eq. 5.7 the chirality projector $\omega^{-} = \frac{1-\gamma_5}{2}$ introduces the gamma matrix $\gamma_5 = i\gamma^0\gamma^1\gamma^2\gamma^3$. In order to consistently apply the dimensional regularization formalism to this calculation, special care must be taken when working with γ_5, which is inherently a four-dimensional object. One way of treating γ_5 in a consistent way is to use the Breitenlohner-Maison formalism [123]–[125].

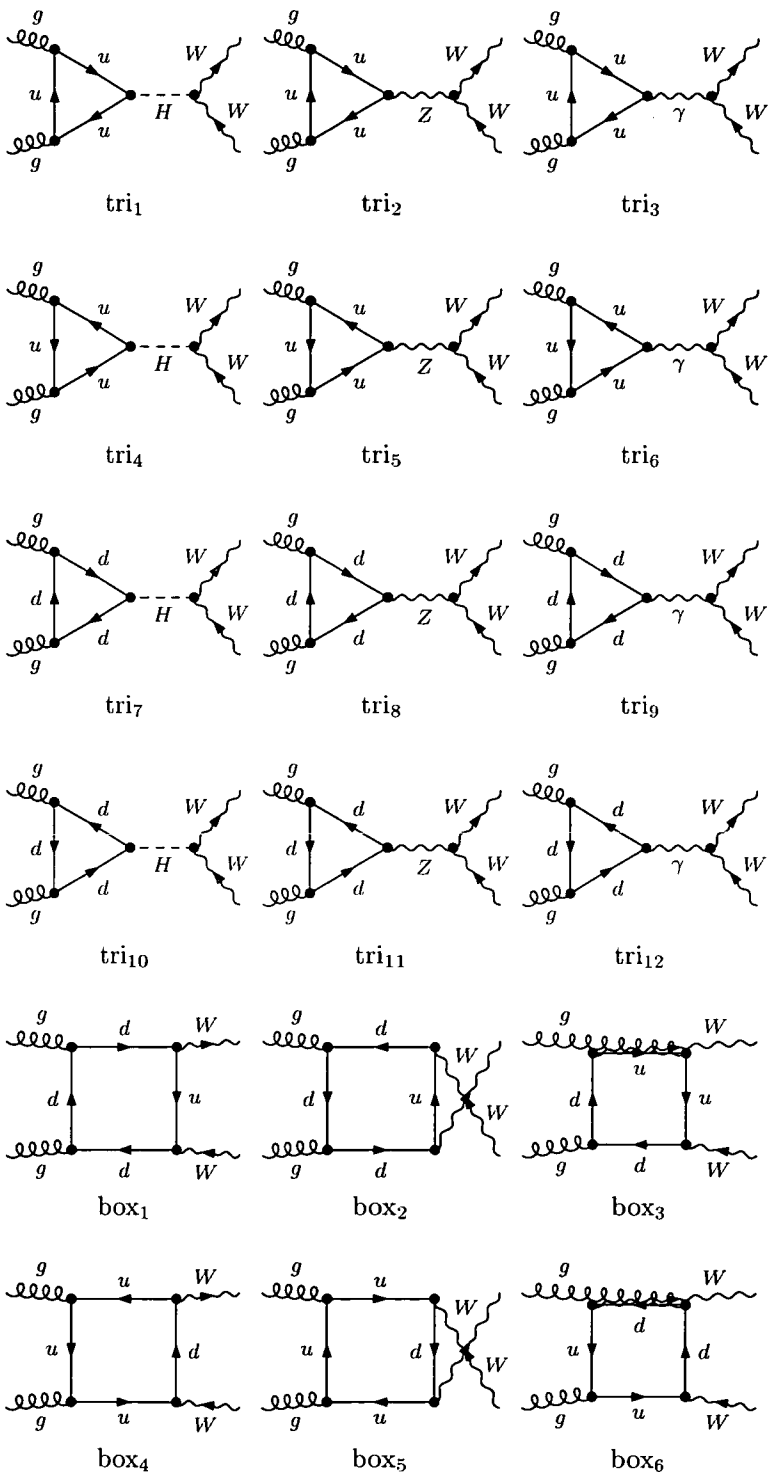

Figure 5.2: Feynman diagrams contributing to the gluon-induced off-shell production of W-boson pairs.

The more general trace $\mathcal{T}$ will be used,

$$\mathcal{T} = \mathrm{Tr}\left\{f^-(\not{k}+m_u)\gamma^{\mu_3}f^-(\not{k}+\not{p}_3+m_d)\gamma^{\mu_1}(\not{k}+\not{p}_3-\not{p}_1-m_d)\gamma^{\mu_2}(\not{k}-\not{p}_4-m_d)\gamma^{\mu_4}\right\},$$

where $f^{\pm} = V_{u,d} \pm A_{u,d}\gamma_5$. Following the Breitenlohner-Maison prescription, the D-dimensional loop-momentum k is split into a four-dimensional component $\tilde{k}$ and a $(D-4)$-dimensional one, $\hat{k}$, such that $k = \hat{k} + \tilde{k}$. Then

$$\begin{aligned} f^+(\not{k}+m_u)\gamma^{\mu_3}f^+ &= f^+(\not{k}+m_u)f^-\gamma^{\mu_3} \\ &= (V_{u,d}^2 - A_{u,d}^2)(\hat{\not{k}}+m_u)\gamma^{\mu_3} \\ &\quad + (A_{u,d}^2 + V_{u,d}^2)(\not{k}-\hat{\not{k}})\gamma^{\mu_3} + 2\gamma_5 A_{u,d}V_{u,d}\tilde{\not{k}}\gamma^{\mu_3}. \end{aligned}$$

Remembering that the couplings for the interaction vertex $u\bar{d}W^-$ satisfies $A_{u,d} = -V_{u,d}$, the trace yields

$$\begin{aligned} \mathcal{T} &= 2V_{u,d}^2\mathrm{Tr}\left\{(\not{k}-\hat{\not{k}}-\gamma_5\tilde{\not{k}})\gamma^{\mu_3}(\not{k}+\not{p}_3+m_d)\gamma^{\mu_1}(\not{k}+\not{p}_3-\not{p}_1-m_d)\gamma^{\mu_2}\right. \\ &\quad \left.(\not{k}-\not{p}_4-m_d)\gamma^{\mu_4}\right\}. \end{aligned}$$

Similar algebraic manipulations were applied to the rest of the box and triangle diagrams.

Due to symmetries in the amplitudes expressions, not all the diagrams contributions need to be calculated explicitly. Out of six different box diagrams, only two are needed, as the following relations demonstrate:

$$\begin{aligned} \mathcal{D}_{\mathrm{box}_4}^{\mu_1\mu_2\mu_3\mu_4}(p_1,p_2,p_3,p_4,m_u,m_d) &= \mathcal{D}_{\mathrm{box}_1}^{\mu_1\mu_2\mu_3\mu_4}(p_1,p_2,p_3,p_4,m_d,m_u)|_{A_{ud}\to -A_{ud}} \\ \mathcal{D}_{\mathrm{box}_2}^{\mu_1\mu_2\mu_3\mu_4}(p_1,p_2,p_3,p_4,m_u,m_d) &= \mathcal{D}_{\mathrm{box}_1}^{\mu_2\mu_1\mu_3\mu_4}(p_2,p_1,p_3,p_4,m_u,m_d) \\ \mathcal{D}_{\mathrm{box}_5}^{\mu_1\mu_2\mu_3\mu_4}(p_1,p_2,p_3,p_4,m_u,m_d) &= \mathcal{D}_{\mathrm{box}_1}^{\mu_2\mu_1\mu_3\mu_4}(p_2,p_1,p_3,p_4,m_d,m_u)|_{A_{ud}\to -A_{ud}} \\ \mathcal{D}_{\mathrm{box}_6}^{\mu_1\mu_2\mu_3\mu_4}(p_1,p_2,p_3,p_4,m_u,m_d) &= \mathcal{D}_{\mathrm{box}_3}^{\mu_1\mu_2\mu_3\mu_4}(p_1,p_2,p_3,p_4,m_d,m_u)|_{A_{ud}\to -A_{ud}}. \end{aligned}$$

On the other hand, all the triangle diagrams satisfy the following relation

$$\mathcal{D}_{\mathrm{tri}_i}^{\mu_1\mu_2\mu_3\mu_4}(p_1,p_2,p_3,p_4,m_f) = \mathcal{D}_{\mathrm{tri}_{3+i}}^{\mu_2\mu_1\mu_3\mu_4}(p_2,p_1,p_3,p_4,m_f)|_{V_{ff}\to -V_{ff}},$$

with $i = \{2,3,8,9\}$. Note that adding all the triangle diagrams corresponding to Z,γ interchange yields a contribution with terms always containing a γ_5 matrix. Consequently, the contribution from the photon exchange diagrams vanishes. This is a clear manifestation of Furry's theorem.

The next step in the calculation involves obtaining the γ matrix traces and writing the invariant amplitude as a linear combination of rational functions of the kinematic invariants of the theory

$$\begin{aligned} \hat{s} &= (p_1 + p_2)^2 \\ \hat{t} &= (p_1 - p_3)^2 \\ \hat{u} &= (p_1 - p_4)^2, \end{aligned}$$

the fermion masses, and one-loop four-point tensor integrals of the form[2]

$$\frac{\mu^{2\epsilon}}{(2\pi)^{4-2\epsilon}} \int d^{4-2\epsilon}k \frac{1,\, k^\mu,\, k^\mu k^\nu,\, k^\mu k^\nu k^\rho,\, k^\mu k^\nu k^\rho,\, k^\mu k^\nu k^\rho k^\sigma}{(k^2 - m_0^2)((k+r_1)^2 - m_1^2)((k+r_2)^2 - m_2^2)((k+r_3)^2 - m_3^2)}. \quad (5.8)$$

After applying the Passarino-Veltman [72, 73] tensor reduction formalism, the invariant amplitude takes the form

$$\mathcal{M}^{\mu_1\mu_2\mu_3\mu_4}(p_1, p_2, p_3, p_4; m_u, m_d) = \sum_{i=1}^{N_V} C_i^V \, \mathcal{T}_{V,i}^{\mu_1\mu_2\mu_3\mu_4} + \sum_{i=1}^{N_A} C_i^A \, \mathcal{T}_{A,i}^{\mu_1\mu_2\mu_3\mu_4},$$

where C_i^A and C_i^V are combinations of rational functions of $\hat{s}$, $\hat{t}$, $\hat{u}$, m_u, m_d, and scalar one-loop integrals. $\mathcal{T}_{V,i}$ and $\mathcal{T}_{A,i}$ are tensor structures constructed using the metric $g_{\mu\nu}$, the Levi-Civita tensor $\epsilon_{\mu\nu\rho\sigma}$, and the three independent external momenta p_1, p_2 and p_3. The tensor structures coming from terms with an odd number of γ_5 matrices contain Levi-Civita tensors. These terms, axial terms, are noted $\mathcal{T}_{A,i}^{\mu_1\mu_2\mu_3\mu_4}$. On the other hand, terms without Levi-Civita tensors, vector contributions, are noted $\mathcal{T}_{V,i}^{\mu_1\mu_2\mu_3\mu_4}$.

If there are no constraints over the amplitude, all the vector C_i^V and axial C_i^A coefficients must be calculated. Symmetry considerations may reduce the number of coefficients to calculate. For instance, there are a total of 138 possible vector coefficients. However, imposing transversality of the gluon polarization vectors

$$\epsilon_i(p_i) \cdot p_j = 0 \;\text{ with }\; i = j = 1, 2 \;, \quad (5.9)$$

the number of needed coefficients is reduced to 76. Furthermore, if gluon polarization vectors are chosen such that they satisfy

$$\epsilon_i(p_i) \cdot p_j = 0 \;\text{ with }\; i \neq j = 1, 2 \;, \quad (5.10)$$

[2]Using $\tilde{k} = k - \hat{k}$ it can be shown that the integrals with $\hat{k}$ in the numerator cancel out when adding the contributions from all Feynman diagrams.

the number of needed coefficients is reduced to 34. As the amplitude is invariant under gluon exchange,

$$\mathcal{M}^{\mu_1\mu_2\mu_3\mu_4}(p_1,p_2,p_3,p_4) = \mathcal{M}^{\mu_2\mu_1\mu_3\mu_4}(p_2,p_1,p_3,p_4)\,, \tag{5.11}$$

the number of independent coefficients is finally reduced to 19. Further simplifications are possible if more assumption are made regarding the W-bosons polarization vectors. For example, including decays into massless leptons reduces the number of needed coefficients to only 13. Similar considerations are valid for the axial coefficients.

This method of writing the invariant amplitude as a combination of tensor structures multiplied by tensor coefficients, which then can be eliminated using symmetry considerations, has already demonstrated an efficient reduction in the complexity of calculations of processes with four external vector bosons. An example where this method has been successfully applied is the calculation of light-by-light scattering in supersymmetric QED theories, in ref. [126].

5.2.1 Calculation Details

As mentioned in the previous section, to calculate the tensor coefficients it is necessary to use the Passarino-Veltman tensor reduction formalism. This technique is of recursive nature, and can be implemented symbolically using computer algebraic software. To that purpose, a set of programs in FORM[127] and Maple were written to accomplish the tensor reduction. The final aim was to write each tensor coefficient as a linear combination of rational functions of the Mandelstam variables and the quark masses, multiplying four- and six-dimensional *scalar* integrals. In the following paragraphs an outline of the different programs is given.

1. A FORM procedure generates basic expressions for the box and triangle diagrams without polarization vectors or lepton currents. The Dirac matrix algebra is calculated, and all the traces are obtained. After these manipulations the contributions of each Feynman diagram to the total amplitude is written as a function of one-loop *tensor* integrals.

2. Another FORM code reduces the one-loop tensor integrals using the Passarino-Veltman reduction technique. The final expression for the amplitude contribu-

tions of each Feynman diagram are written as a linear combination of the basic tensor structures, multiplied by tensor coefficients.

3. A Maple code is used to simplify the FORM output.

4. Finally, another Maple code combines the contributions from all Feynman diagrams, further simplifying the results. The final output contains the invariant amplitude tensor coefficients, each of which is written as a linear combination of one-loop *scalar* functions.

Negative Powers of Gram Determinants

The expression for the invariant amplitude obtained with this method suffers from the presence of negative powers of Gram determinants, which arise in the Passarino-Veltman reduction formalism. It can be shown that the vanishing of these Gram determinants does not introduce divergences in the calculation. This is because the determinants appear only as a calculational tool, they do not have a physical interpretation. As the vanishing of the Gram determinants in the denominators does not generate real divergences, there must be cancellations acting also in the corresponding numerators. This is easily seen in the following example. Using the Passarino-Veltman technique, the two-point tensor integral

$$B_\mu(p^2, m_0^2, m_1^2) = \frac{\mu^{2\epsilon}}{(2\pi)^{4-2\epsilon}} \int d^{4-2\epsilon}k \frac{k_\mu}{(k^2 - m_0^2)((k+p)^2 - m_1^2)},$$

can be written as

$$B_\mu(p^2, m_0^2, m_1^2) = p_\mu B_1(p^2, m_0^2, m_1^2),$$

where

$$B_1(p^2, m_0^2, m_1^2) = \frac{1}{2p^2}\left[A_0(m_0^2) - A_0(m_1^2) - (m_0^2 - m_1^2 + p^2)B_0(p^2, m_0^2, m_1^2)\right].$$

In this case, the Gram determinant is just $\Delta = p^2$. Before taking the limit $\Delta \to 0$ one can rewrite the tensor integral using the relation

$$B_0(0, m_0^2, m_1^2) = \frac{A_0(m_0^2) - A_0(m_1^2)}{m_0^2 - m_1^2}.$$

Then,

$$B_1(p^2, m_0^2, m_1^2) = \frac{1}{2p^2}\left[-(m_0^2 - m_1^2)(B_0(p^2, m_0^2, m_1^2) - B_0(0, m_0^2, m_1^2)) - p^2 B_0(p^2, m_0^2, m_1^2)\right].$$

Taking the limit $p^2 \to 0$ yields

$$\begin{aligned} & B_1(p^2 \to 0, m_0^2, m_1^2) = \\ &= -\frac{m_0^2 - m_1^2}{2} \frac{\partial}{\partial p^2} B_0(p^2, m_0^2, m_1^2) - \frac{1}{2} B_0(p^2, m_0^2, m_1^2) \\ &= \frac{1}{2D} \frac{1}{(m_1^2 - m_0^2)^2} \left[A_0(m_1^2)((4-D)m_1^2 + Dm_0^2) \right. \\ &\quad \left. + A_0(m_0^2)((D-4)m_0^2 - Dm_1^2) \right] - \frac{1}{2} B_0(0, m_0^2, m_1^2) \,. \end{aligned} \tag{5.12}$$

As expected, B_1 remains finite in the limit of vanishing Gram determinant. With higher order and/or higher rank tensor integrals the simplifications become more complex, and the risk of numerical instabilities when evaluating these functions numerically increases.

In the invariant amplitude for gluon induced off-shell production of W-boson pairs, one class of Gram determinants becomes problematic. This Gram determinant arises from a one-loop rank-four tensor integral and can be written as

$$\begin{aligned} \Delta &= \hat{u}\hat{t} - p_3^2 p_4^2 \\ &= \hat{t}p_3^2 + \hat{t}p_4^2 - \hat{s}\hat{t} - \hat{t}^2 - p_3^2 p_4^2 \\ &= \hat{u}p_3^2 + \hat{u}p_4^2 - \hat{s}\hat{u} - \hat{u}^2 - p_3^2 p_4^2 \\ &= \hat{s}|\vec{p}_3^{\,T}|^2 \,, \end{aligned}$$

where $\vec{p}_3^{\,T}$ is the transverse momenta of the W^- boson in the gluons centre-of-mass frame. In some tensor coefficients the Gram determinant appears evaluated to the fourth power in the denominator. This introduces serious instabilities in the numerical evaluation of the cross section. This problem has been solved evaluating the cross section in the limit of massless quarks circulating the loops, as explained in Section 5.4, and applying a cut on $|\vec{p}_3^{\,T}|$.

5.2.2 Ultraviolet and Infrared Divergences

Although the process studied here does not suffer from ultraviolet (UV) or infrared (IR) divergences, the individual Feynman diagrams do contain divergences. The UV finiteness of the total amplitude is easy to see, as in the Standard Model there is no counterterm for a vertex of the form ggW^+W^-.

More rigorously, one can regularize the UV and IR divergences using dimensional regularization. Any divergence can be isolated as a pole in the parameter $\epsilon = 2 - D/2$, where D is the number of dimensions. After the tensor reduction procedure the amplitude is written as a linear combination of two-, three- and four-point one-loop scalar functions. UV divergences arise only from two-point scalar functions. Expanding this contributions as a Laurent series in ϵ, it was explicitly demonstrated that the total amplitude does not contain poles coming from ultraviolet divergences.

On the other hand, IR divergences appear as a result of the quarks circulating the loops becoming massless. In that case on can rewrite the invariant amplitude as a function of two- and three-point four-dimensional scalar functions together with four-point six-dimensional scalar functions. These two-point and four-point integrals are IR safe quantities. It was demonstrated that the only three point scalar functions that contribute to the total invariant amplitude are IR finite, too. Consequently, there are no IR divergences in the final result.

5.3 Gluon Induced off-shell W^+W^- Production with Decay into lepton-neutrino pairs

The tensor coefficients calculated in Section 5.2 can be used to study gluon induced W-boson pair production with decay into lepton-neutrino pairs,

$$g(p_1)\, g(p_2) \;\rightarrow\; W^{-*}(p_3)\, W^{+*}(p_4) \;\rightarrow\; l(p_5)\, \bar{\nu}_l(p_6)\, \bar{l}'(p_8)\, \nu_{l'}(p_7)\,, \tag{5.13}$$

where $p_3 = p_5 + p_6$ and $p_4 = p_7 + p_8$. The invariant amplitude can be written as

$$\mathcal{M}_{\mu_1\mu_2\mu_3\mu_4}(p_1, p_2, p_3, p_4, m_u, m_d)\epsilon_1{}^{\mu_1}(p_1, \lambda_1)\epsilon_2{}^{\mu_2}(p_2, \lambda_2)J_3^{\mu_3}(p_5, p_6)J_4^{\mu_4}(p_7, p_8)\,,$$

where $\mathcal{M}_{\mu_1\mu_2\mu_3\mu_4}(\ldots)$ is defined in eq. 5.6. The lepton currents read

$$J_3^{\mu_3}(p_5, p_6) = \left(g_{\nu_3}^{\mu_3} - \frac{p_3{}^{\mu_3} p_{3\nu_3}}{M_W^2}\right) \frac{1}{p_3^2 - M_W^2 + i\Gamma_W M_W} \bar{u}_l(p_5)\gamma^{\nu_3}\omega^- v_{\bar{\nu}}(p_6) \tag{5.14}$$

$$J_4^{\mu_4}(p_7, p_8) = \left(g_{\nu_4}^{\mu_4} - \frac{p_4{}^{\mu_4} p_{4\nu_4}}{M_W^2}\right) \frac{1}{p_4^2 - M_W^2 + i\Gamma_W M_W} \bar{u}_{\nu'}(p_7)\gamma^{\nu_4}\omega^- v_{\bar{l}'}(p_8) \tag{5.15}$$

where the narrow width approximation and unitary gauge have been used. In the massless lepton limit these expressions reduce to

$$J_3^{\mu_3}(p_5, p_6) = \frac{1}{p_3^2 - M_W^2 + i\Gamma_W M_W} \bar{u}_l(p_5)\gamma^{\mu_3}\omega^- v_{\bar{\nu}}(p_6) \tag{5.16}$$

$$J_4^{\mu_4}(p_7,p_8) = \frac{1}{p_4^2 - M_W^2 + i\Gamma_W M_W}\bar{u}_{\nu'}(p_7)\gamma^{\mu_4}\omega^- v_{\bar{l}'}(p_8)\,. \tag{5.17}$$

As mentioned before, in the massless lepton limit there are extra constraints on the invariant amplitude that allow for a reduction in the number of tensor coefficients needed to be calculated explicitly. This is due to the relations

$$\begin{aligned} p_3 \cdot J_3 &= 0 \\ p_4 \cdot J_4 &= 0\,. \end{aligned}$$

The gluon polarization vectors and the lepton currents are calculated as spinor products using the helicity spinor formalism[128][3]:

$$\epsilon_{g_1}^{\mu_1}(p_1,\pm) = \frac{\langle p_2^{\mp}|\gamma^{\mu_1}|p_1^{\mp}\rangle}{\langle 2\ 1\rangle^{(*)}} \tag{5.18}$$

$$\epsilon_{g_2}^{\mu_2}(p_2,\pm) = \frac{\langle p_1^{\mp}|\gamma^{\mu_2}|p_2^{\mp}\rangle}{\langle 1\ 2\rangle^{(*)}} \tag{5.19}$$

$$J_3^{\mu_3}(p_5,p_6) = \langle p_5^-|\gamma^{\mu_3}|p_6^-\rangle \tag{5.20}$$

$$J_4^{\mu_3}(p_7,p_8) = \langle p_7^-|\gamma^{\mu_4}|p_8^-\rangle\,. \tag{5.21}$$

In this formalism, the following products of polarization vectors are easily obtained

$$\epsilon_{g_1}^{\mu_1}(p_1,+)\epsilon_{g_2}^{\mu_2}(p_2,+) = \frac{e^{-i\phi(p_1,p_2)}}{2}\frac{\mathrm{Tr}\{\not p_1\gamma^{\mu_1}\not p_2\gamma^{\mu_2}\} - 4i\epsilon^{p_1\mu_1 p_2\mu_2}}{2p_1\cdot p_2} \tag{5.22}$$

$$\begin{aligned}\epsilon_{g_1}^{\mu_1}(p_1,+)\epsilon_{g_2}^{\mu_2}(p_2,-) &= \frac{e^{-i\phi(p_1,p_2,p_3)}}{8}\frac{1}{\hat{s}(\hat{t}\hat{u} - p_3^2p_4^2)} \\ &\quad (\mathrm{Tr}\{\not p_2\not p_3\not p_1\gamma^{\mu_1}\} \mp 4i\epsilon^{p_2p_3p_1\mu_1})(\mathrm{Tr}\{\not p_2\not p_3\not p_1\gamma^{\mu_1}\} \mp 4i\epsilon^{p_2p_3p_1\mu_1})\,.\end{aligned} \tag{5.23}$$

The lepton currents J_3 and J_4 can be worked out in a similar way.

Finally, the full amplitude can be rewritten as

$$\begin{aligned}\mathcal{M}^{\zeta_1\zeta_2 J_3 J_4}\Big|_{\zeta_1\zeta_2=++,+-} &= \epsilon_{g_1}^{\mu_1}(p_1,\zeta_1)\epsilon_{g_2}^{\mu_2}(p_2,\zeta_2)\frac{J_3{}^{\mu_3}(p_5,p_6)}{p_3^2 - M_W^2 + i\Gamma_W M_W} \\ &\quad \frac{J_4{}^{\mu_4}(p_7,p_8)}{p_4^2 - M_W^2 + i\Gamma_W M_W}\mathcal{M}_{\mu_1\mu_2\mu_3\mu_4} \\ \mathcal{M}^{--J_3J_4} &= \left[\mathcal{M}^{++J_4J_3}\right]^* \\ \mathcal{M}^{-+J_3J_4} &= \left[\mathcal{M}^{+-J_4J_3}\right]^*\,.\end{aligned}$$

[3] A brief summary of the basic concepts in the helicity spinor formalism is given in Appendix A.

5.3.1 Gauge Invariance

When calculating the invariant amplitude of the process which includes vector boson leptonic decays it is essential to note that, as mentioned in Section 5.1.2, the set of double resonant diagrams of figure 5.2 does not constitute a gauge invariant set. This

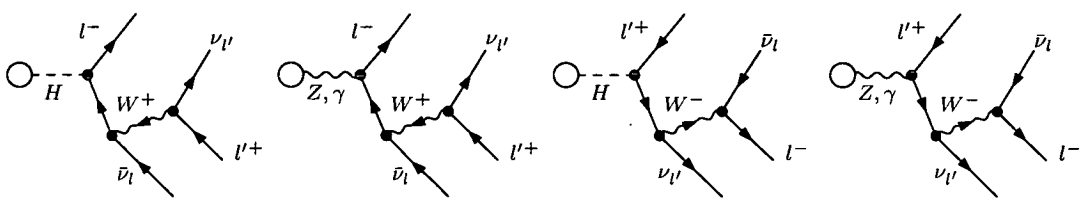

Figure 5.3: Single-resonant diagrams contributing to the process eq. 5.4, needed to maintain gauge invariance. Only contributions where the resonant W-boson is attached to the neutrino line are shown. Four more diagrams are needed, similar to these but with the W-boson attached to the charged lepton line.

can be seen calculating this contribution in different gauges, for instance unitary gauge and axial gauge[4]. More generally, a set of Feynman diagrams is gauge invariant if and only if it satisfies the Ward identities of the theory. In this case the Ward identity shown in figure 5.4 was calculated using the set of graphs in fig. 5.2, see for instance [130]. The obtained result, as expected, is nonzero. This means that the Ward identity

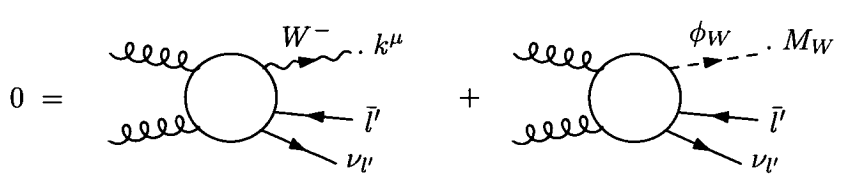

Figure 5.4: Ward Identity that must be satisfied by the gauge invariant amplitude.

is not satisfied by the set of double-resonant graphs, and that this set of diagrams is not gauge invariant. This problem is solved introducing the single resonant graphs. Calculating the Ward identity for the set of single resonant diagrams, examples of which

[4]The Standard Model in the axial gauge has been recently studied in [129].

are shown in fig. 5.3, one obtains exactly the same contribution as obtained for the double resonant diagrams, but with opposite sign. Which means that the total set of single- and double-resonant graphs is indeed gauge invariant.

It is interesting to note that the terms contributing to the violation of the Ward identity are all axial terms, that is, terms containing Levi-Civita tensors. Using the relations between Feynman diagrams in Section 5.2 it can be seen that the contribution from the axial terms vanishes if massless/degenerate quarks are circulating the loops. This means that the single resonant contributions are not needed in the massless case. What's more, in the massless quark approximation, the total contribution from single resonant diagrams is zero.

The inclusion of single resonant diagrams is not particular to gluon initiated W-boson pair production. The calculation of the NLO production cross section for gauge boson pairs at hadron colliders presented in ref [107] also includes the single-resonant diagrams in their analysis. Gauge-invariance problems also appear when calculating off-shell W-boson pair production in e^+e^- collisions, see for instance ref. [131]. As in the hadronic case, to recover gauge-invariance the introduction of single-resonant graphs is needed.

5.4 The Massless Case

As mentioned in the previous section, the representation of the invariant amplitude contains negative powers of Gram determinants which make the numerical evaluation of the full expression for massless and massive quarks unstable. In order to obtain a stable evaluation of the cross section, the numerical calculation was done in the massless quark approximation: the mass m_q of the quarks circulating the loops are assumed to satisfy $m_q \ll \hat{s}$. This approximation greatly simplifies the invariant amplitude for off-shell production of W-boson pairs. The axial terms cancel out and a new representation for the amplitude can be obtained. This representation is written in terms of only nine tensor coefficients and nine analytic functions. What's more, the splitting of the amplitude as a function of the gluon helicities and the use of explicit expressions for the one-loop scalar functions yields a much simpler and more stable result. In the case of gluons with the same helicity, no negative powers of the Gram determinant are found

in the tensor coefficients. In the case of gluons with different helicities only a power of two of the Gram determinant appears in the denominator, one of which is an overall factor. The final expressions for the amplitudes can be written as follows

$$\mathcal{M} = \sum_{i,j=1}^{9} \mathcal{T}_i(p_l, J_l, \epsilon_l)\mathcal{F}_i(\hat{s},\hat{t},\hat{u},p_3^2,p_4^2)C^{ij}(\hat{s},\hat{t},\hat{u},p_3^2,p_4^2)\,,$$

where $\mathcal{T}_i$ are nine tensor structures depending on the external momenta, polarization vectors and spinor products, $\mathcal{F}_i$ are functions arising from the explicit expression of one-loop scalar functions and C^{ij} are rational functions of $\hat{s}$, $\hat{t}$, $\hat{u}$, p_3^2 and p_4^2. Explicitly, the functions base is

$$\begin{aligned}
\mathcal{F}_1(\hat{s},\hat{t},\hat{u},p_3^2,p_4^2) &= D_0^{D=6-2\epsilon}(\hat{s},\hat{t},p_3^2,p_4^2)\,,\\
\mathcal{F}_2(\hat{s},\hat{t},\hat{u},p_3^2,p_4^2) &= D_0^{D=6-2\epsilon}(\hat{s},\hat{u},p_3^2,p_4^2)\\
\mathcal{F}_3(\hat{s},\hat{t},\hat{u},p_3^2,p_4^2) &= F_B(\hat{t},\hat{u},p_3^2,p_4^2)\,,\\
\mathcal{F}_4(\hat{s},\hat{t},\hat{u},p_3^2,p_4^2) &= C_0(p_3^2,\hat{s},p_4^2)\,,\\
\mathcal{F}_5(\hat{s},\hat{t},\hat{u},p_3^2,p_4^2) &= \ln\left(\frac{s}{t}\right)\,,\\
\mathcal{F}_6(\hat{s},\hat{t},\hat{u},p_3^2,p_4^2) &= \ln\left(\frac{s}{u}\right)\,,\\
\mathcal{F}_7(\hat{s},\hat{t},\hat{u},p_3^2,p_4^2) &= \ln\left(\frac{s}{w_1^2}\right)\,,\\
\mathcal{F}_8(\hat{s},\hat{t},\hat{u},p_3^2,p_4^2) &= \ln\left(\frac{s}{w_2^2}\right)\,,\\
\mathcal{F}_9(\hat{s},\hat{t},\hat{u},p_3^2,p_4^2) &= 1\,.
\end{aligned} \tag{5.24}$$

In these expressions, $D_0^{D=6-2\epsilon}$ is the six-dimensional four-point scalar function, F_B is related to the four-dimensional four-point scalar function and C_0 is the three-point scalar function. All these functions are defined in Appendix B. On the other hand, the tensor structures are

$$\begin{aligned}
\mathcal{T}_1(p_i,J_i,\epsilon_i) &= J_3\cdot J_4\,,\\
\mathcal{T}_2(p_i,J_i,\epsilon_i) &= J_3\cdot p_1\; J_4\cdot p_1\,,\\
\mathcal{T}_3(p_i,J_i,\epsilon_i) &= J_3\cdot p_1\; J_4\cdot \tilde{p}_3\,,\\
\mathcal{T}_4(p_i,J_i,\epsilon_i) &= J_3\cdot \tilde{p}_3\; J_4\cdot p_1\,,\\
\mathcal{T}_5(p_i,J_i,\epsilon_i) &= J_3\cdot \tilde{p}_3\; J_4\cdot \tilde{p}_3\,,\\
\mathcal{T}_6(p_i,J_i,\epsilon_i) &= J_3\cdot p_1\; \epsilon_{p_1p_2\tilde{p}_3J_4}\,,
\end{aligned}$$

$$\begin{aligned}
\mathcal{T}_7(p_i, J_i, \epsilon_i) &= J_3 \cdot \tilde{p}_3 \, \epsilon_{p_1 p_2 \tilde{p}_3 J_4} \,, \\
\mathcal{T}_8(p_i, J_i, \epsilon_i) &= J_4 \cdot p_1 \, \epsilon_{p_1 p_2 \tilde{p}_3 J_3} \,, \\
\mathcal{T}_9(p_i, J_i, \epsilon_i) &= \epsilon_{p_1 p_2 J_3 J_4} \,,
\end{aligned} \tag{5.25}$$

where the auxiliary momentum $\tilde{p}_3$ is defined as

$$\tilde{p}_3 = p_3 + \frac{\hat{u} - p_3^2}{\hat{s}} p_1 + \frac{\hat{t} - p_3^2}{\hat{s}} p_2 \,.$$

5.5 Numerical Evaluation

5.5.1 Methodology

After obtaining the final representation for the invariant amplitude, a Maple program was used to translate the algebraic expressions into FORTRAN code, suitable for numerical evaluation. It is important to note that the numerical evaluation is done at the amplitude level, not at the cross section level and that, in order to retain all spin-angle correlations of the final states, no polarization sums are done. Once the amplitudes and spinor products have been calculated, the parton cross section $\hat{\sigma}$ is obtained. Convoluting $\hat{\sigma}$ with the gluon parton distribution functions $f_{p,g}(x)$ yields the hadron cross section

$$\sigma(pp \to W^{-*} W^{+*} \to e^- \bar{\nu}_e \, \mu^+ \nu_\mu) = \int dx_1 dx_2 f_{p_1,g}(x_1) f_{p_2,g}(x_2) \hat{\sigma}(x_1 p_1, x_2 p_2). \tag{5.26}$$

To make this convolution and integrate over the final particles momenta, a phase space generator was written, which was combined with the code for calculating the differential cross section and the VEGAS[132] adaptive Monte Carlo integrator.

As mentioned in the previous section, the numerical evaluation of the total cross section becomes unstable due to the presence of negative powers of the Gram determinant $\Delta = \hat{t}\hat{u} - p_3^2 p_4^2$ in the amplitudes of processes induced by gluons of opposite helicities. The first step in avoiding these instabilities involved working in the approximation of massless quarks circulating the loops. The final step involves introducing a technical cut on the W-boson transverse momenta $p_T = |\vec{p}_{3T}|$. For gluon induced off-shell production of W-boson pairs which decay leptonically

$$1\,\text{GeV} \leq p_T^W \tag{5.27}$$

is imposed to obtain a stable result. The choice of phase space parametrization is also important. To further reduce instabilities in the final result p_T can be chosen as integration variable. A detailed discussion of the different phase space parametrizations for processes with four massless particles in the final state is presented in Appendix C.

It is important to compare the size of the gluon induced contributions to the size of quark initiated processes. The contribution to the cross section for off-shell W-boson pair production with leptonic decays from quark induced processes was calculated using the Monte Carlo program MCFM[107]. This contribution was calculated in leading-order and next-to-leading order in α_s.

5.5.2 Input Parameters

The electroweak parameter scheme used is the G_μ-scheme. As discussed in Chapter 4, large fermion-mass logarithms are resummed and universal corrections to the SU(2) gauge coupling $e/s_{\rm W}$ induced by the ρ-parameter are automatically absorbed in this input parameter scheme. To simplify the comparison with the $q\bar{q} \to WW$ contribution the numerical values for the input parameters were chosen to be the same as the G_μ-scheme input parameters in MCFM. The following values were used,

$$\begin{aligned}
G_\mu &= 1.16639 \times 10^{-5}\,\text{GeV}^{-2} & M_{\rm H} &= 165\,\text{GeV} \\
M_{\rm W} &= 80.419\,\text{GeV} & M_{\rm Z} &= 91.188\,\text{GeV} \\
\Gamma_W &= 2.06\,\text{GeV} & \Gamma_Z &= 2.49\,\text{GeV} \\
|V_{\rm ud}| &= 1.0 & |V_{\rm us}| &= 0.0 \\
|V_{\rm cd}| &= 0.0 & |V_{\rm cs}| &= 1.0.
\end{aligned} \tag{5.28}$$

The CTEQ6[85] set of parton distribution functions was used. For NLO quark and gluon initiated processes, the parton distribution function set CTEQ6M was chosen. On the other hand, for the LO calculation of the quark initiated processes the CTEQ6L1 set was used.

The strong coupling used is consistent with the parton distribution set chosen: when using CTEQ6L1 a LO running α_s is used, with $\alpha_s(M_Z^2) = 0.130$. When using CTEQ6M a NLO evolved α_s is used, with $\alpha_s(M_Z^2) = 0.118$. A $\Lambda_{\rm QCD}$ for 5 active flavours was

used with value 226 GeV for CTEQ6M and 165 GeV for CTEQ6L1. The factorization scale was always chosen to be $\Lambda = M_W$.

All calculations were evaluated for an LHC-type collider: pp collisions with centre-of-mass energy of 14 TeV and for two degenerate massless generations(u, d, c and s quarks).

5.5.3 Technical and signal-enhancing Cuts

As explained above, a technical cut on the W-bosons transverse momenta is needed to obtain a stable numerical result. The technical cut used is

$$p_T^{\text{cut}} < p_T \quad \text{with} \quad p_T^{\text{cut}} = 1\,\text{GeV}\,. \tag{5.29}$$

In addition to calculating the total cross section for the process 5.13, the effect of the cuts proposed in [112] to enhance the signal to background ratio in Higgs boson searches was studied. The set of cuts used is the following,

1. The transverse polar angle of the dilepton system must satisfy $\phi_\perp(ll) < 45°$ and the dilepton invariant mass $M_{ll} < 35\,\text{GeV}$.

2. Jet veto: events with jets with $p_T^{\text{jet}} > 20\,\text{GeV}$ and pseudorapidity $|\eta^{\text{jet}}| < 3$ are removed.

3. The leptons in the final state are classified according to their transverse momenta: calling $p_{T\text{min}}$ and $p_{T\text{max}}$ the largest and smallest lepton transverse momenta the following selection cuts are imposed: $25\,\text{GeV} < p_{T\text{min}}$ and $35\,\text{GeV} < p_{T\text{max}} < 50\,\text{GeV}$.

5.5.4 Cross Section Results

First, on-shell production of W-boson pairs was studied. As the cross section was calculated from the invariant matrix elements where the vector bosons decay into massless leptons, these results only take into account transverse W-bosons. Figure 5.5 shows the W^-W^+ invariant mass distribution $d\sigma/dM_{M_{WW}}$. This distribution was calculated imposing a standard pseudorapidity cut $|\eta_W| < 2.5$, consequently, the calculation is not sensitive to the instabilities that appear in the small p_T region, and the technical p_T cut has not been used. The three curves show the gluon induced and the LO and NLO

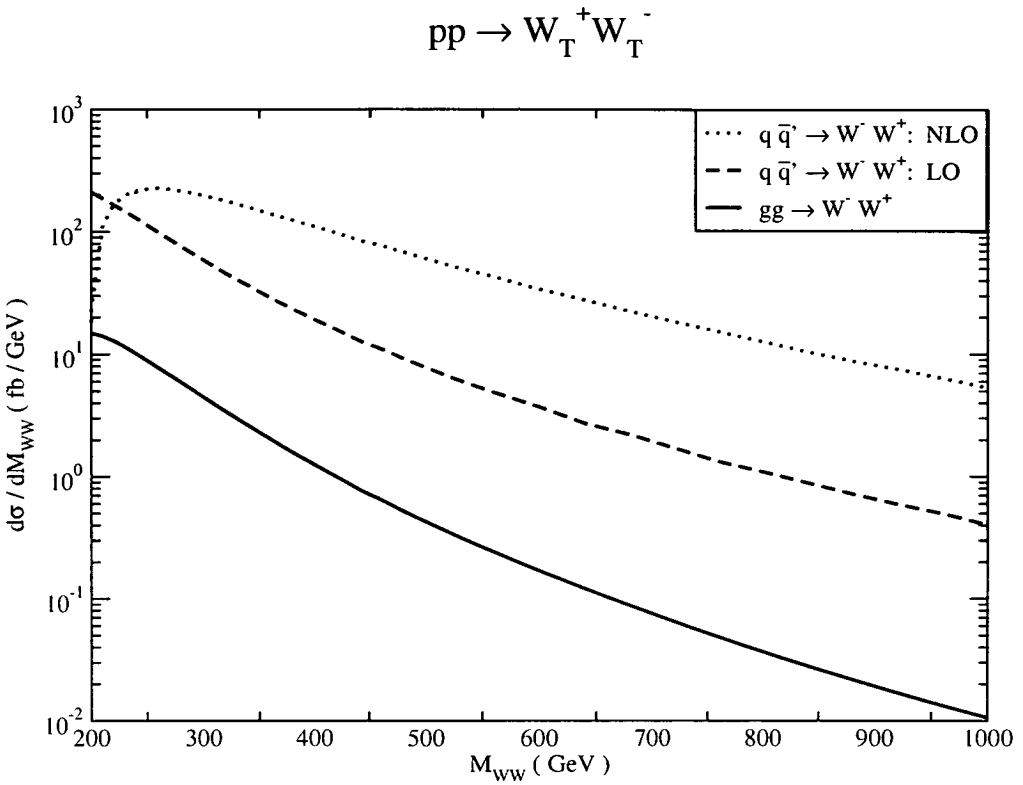

Figure 5.5: Invariant mass distributions for gluon and quark induced on-shell $W^+ W^- + X$ production at a pp collider with center of mass energy $\sqrt{s} = 14\,\text{TeV}$. The standard acceptance cut $|\eta_W| < 2.5$ was imposed. The quark induced contributions are calculated to LO and NLO using MCFM. No further cuts are applied.

quark induced contributions. As expected, the contribution from $gg \to WW$ is the smallest one, being one or more orders of magnitude smaller that the quark initiated processes. In all cases, the mass distribution is strongly dependent on the W-boson pair mass, and it decreases sharply for increasing invariant mass. The total cross section for these contributions, together with the ratio between the gluon and quark(NLO) induced processes, are shown in table 5.2.

The cross section for the contribution $gg \to W^-W^+ \to l^-\bar{\nu}\, l'^+\nu_{l'}$ to the process $pp \to W^-W^+ \to l^-\bar{\nu}\, l'^+\nu_{l'} + X$ is shown in figure 5.6. The contributions from different gluon helicities are depicted, together with the total cross section. The notation in the plot is related to the gluons helicities as follows,

$$++ \;\to\; \epsilon_{g_1}(p_1,+)\epsilon_{g_2}(p_2,+)$$

$\sigma(gg \to WW)$	$\sigma_{LO}(qq \to WW)$	$\sigma_{NLO}(qq \to WW)$	$\frac{\sigma(gg \to WW)}{\sigma_{NLO}(qq \to WW)}$
0.907(2)pb	25.73(4)pb	45.86(2)pb	0.01978(5)

Table 5.2: Total cross section for gluon and quark induced contributions to the process $pp \to W^+W^-$, with $\sqrt{s} = 14\,\text{TeV}$. The cross section for quark induced processes was calculated to LO and NLO in QCD. Furthermore, the last column shows the ratio between the gluon induced process cross section and the NLO QCD corrected quark induced process.

$\sigma(gg \to WW)$	$\sigma_{LO}(qq \to WW)$	$\sigma_{NLO}(qq \to WW)$	$\frac{\sigma(gg \to WW)}{\sigma_{NLO}(qq \to WW)}$
40.03(6) fb	877(1)fb	1372(2)fb	0.02918(6)

Table 5.3: Total cross section for gluon and quark induced contributions to the process $pp \to W^+W^- \to l^-\bar{\nu}l'^+\nu_{l'}$, with $\sqrt{s} = 14\,\text{TeV}$. The cross section for quark induced processes was calculated to LO and NLO in QCD. Furthermore, the last column shows the ratio between the gluon induced process cross section and the NLO QCD corrected quark induced process. No physical cuts are applied. The technical cut on the W-boson transverse momenta $1\,\text{GeV} < p_T$ was used.

$\sigma(gg \to WW)$	$\sigma_{LO}(qq \to WW)$	$\sigma_{NLO}(qq \to WW)$	$\frac{\sigma(gg \to WW)}{\sigma_{NLO}(qq \to WW)}$
0.687(2) fb	6.806(7)fb	7.06(3)fb	0.0973(5)

Table 5.4: Same as table 5.3, but the three physical cuts described in Section 5.5.3 have been applied.

$$
\begin{aligned}
-- &\to \epsilon_{g_1}(p_1,-)\epsilon_{g_2}(p_2,-) \\
+- &\to \epsilon_{g_1}(p_1,+)\epsilon_{g_2}(p_2,-) \\
-+ &\to \epsilon_{g_1}(p_1,-)\epsilon_{g_2}(p_2,+)\,.
\end{aligned}
$$

The cross sections are plotted against the value of the technical cut p_T^{cut}. It can be seen that for small p_T^{cut} there is not a strong dependence of the cross section with respect to the cut, and the curves become flat for $p_T^{\text{cut}} \to 0$. This reinforces the hypothesis of

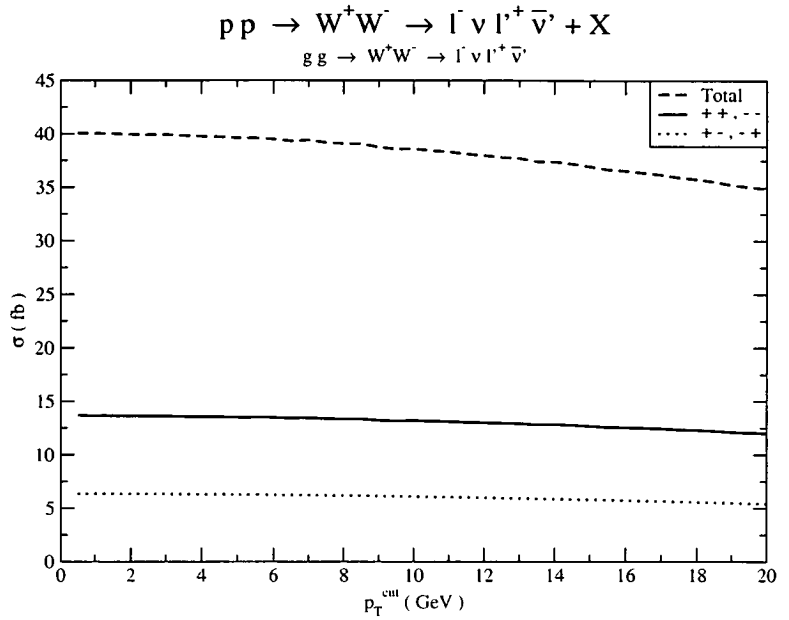

Figure 5.6: Total cross section for the gluon induced contribution to the process $pp \to W^-W^+ \to l^-\bar{\nu}\, l'^+\nu_{l'} + X$ as a function of the technical cut p_T^{cut}. The $--, ++$ curve corresponds to processes with gluons of same helicities in the initial state. On the other hand, the $+-, -+$ curve shows the cross section of the contribution with gluons of opposite helicities.

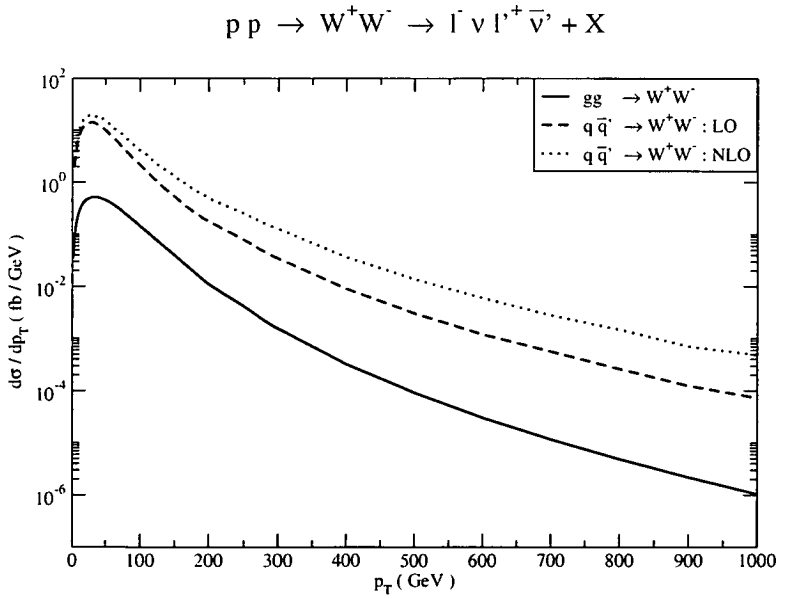

Figure 5.7: p_T distributions for gluon and quark induced contributions to the process $pp \to W^-W^+ \to l^-\bar{\nu}\, l'^+\nu_{l'} + X$. The quark induced process distribution was calculated to LO and NLO using the MCFM program.

the instabilities for small p_T[5] being of a calculational origin, and not having a physical interpretation.

The p_T distributions $d\sigma/dp_T$ for the gluon induced contribution and for the quark initiated processes to LO and NLO are depicted in figure 5.7. The quark induced distributions were calculated using MCFM. As expected, due to the α_S^2 suppression, the gluon distribution is at least one order of magnitude smaller than the distribution corresponding to quark initiated processes. Despite the difference in value, the distributions from both contributions behave similarly. For very small increasing p_T a sharp increase can be seen in the distributions. A peak appears at a value $p_t \sim 30\,\text{GeV}$, and then the distributions start a sharp decrease as p_T is increased. A similar behaviour has been observed in the gluon induced on-shell production of Z-boson pairs[119]. It is interesting to note that the value chosen for the technical cut, $p_T^{\text{cut}} = 1\,\text{GeV}$, is much smaller than the p_T for which the distributions peak. Consequently, the contributions that are left out because of the cut are expected to be small. The total cross section for each of the contributions, with the technical cut $1\,\text{GeV} < p_T$, can be seen in table 5.3, together with the ratio between the gluon induced process cross section and the quark induced process NLO corrected cross section.

The effect of the signal-enhancing cuts discussed in section 5.5.3, based on the cuts proposed in [112], has been studied for the gluon and quark induced contributions. Figure 5.8 shows the cross section of the gluon induced contribution, for different gluon helicities, as a function of the technical cut p_T^{cut}. One would expect that the inclusion of the physical cuts would decrease the dependence of the cross section with respect to p_T^{cut}. On the contrary, figure 5.8 shows that the dependence on the technical cut is increased after the use of the cuts. Namely, in the interval $1\,\text{GeV} < p_T^{\text{cut}} < 10\,\text{GeV}$ the total cross section variation is approx. 7% in the configuration without physical cuts, and approx. 17% when the cuts are applied.

Finally, figure 5.9 shows the p_T distributions for the gg and the qq contributions to W-boson pair production with leptonic decay after the inclusion of the signal-enhancing cuts. It can be seen that the cuts have had an important effect on the cross sections. For transverse momenta $100\,\text{GeV} < p_T$ the distributions decrease sharply. In the case

[5]Unless otherwise specified, in the rest of this chapter the notation p_T is used to describe the transverse momenta of either the W^+ or W^- gauge boson.

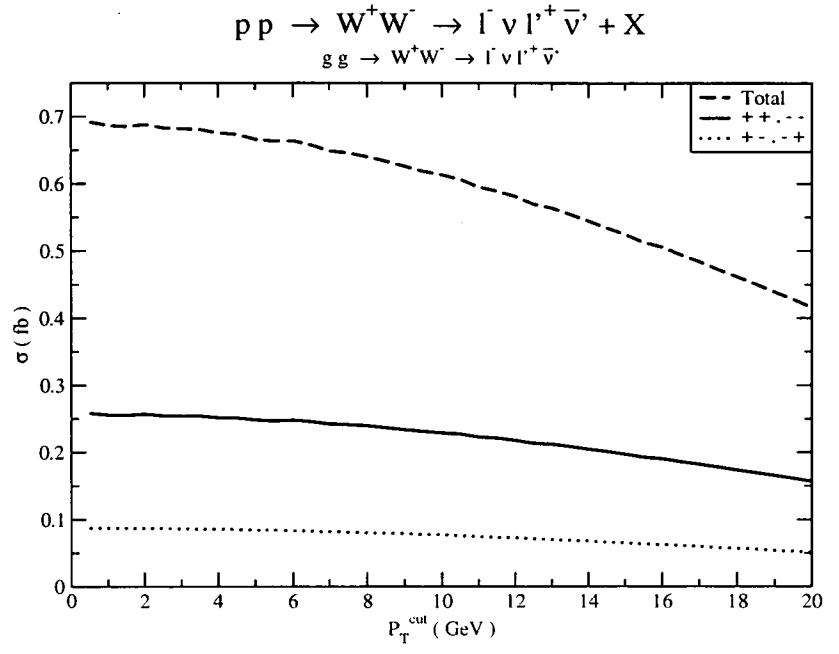

Figure 5.8: Total cross section for the gluon induced contribution to the process $pp \to W^-W^+ \to l^-\bar{\nu}\, l'^+\nu_{l'} + X$ as a function of the technical cut p_T^{cut}, after applying the set of experimental cuts discussed in Section 5.5.3. Notation is the same as in figure 5.6.

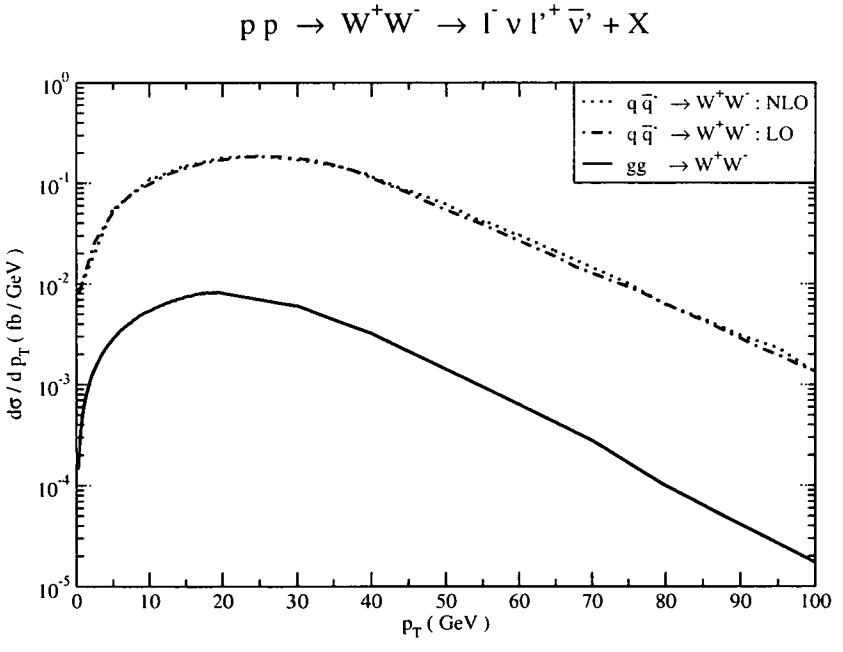

Figure 5.9: p_T distributions for gluon and quark induced contributions to the process $pp \to W^-W^+ \to l^-\bar{\nu}\, l'^+\nu_{l'} + X$, including the signal-enhancing cuts of section 5.5.3. The quark induced process distribution was calculated to LO and NLO using the MCFM program.

of MCFM the number of events used to construct the histogram of the distribution falls abruptly, and the results become unreliable. Consequently, the p_T distributions have been plotted only in the range 0 GeV – 100 GeV. Another notorious feature is that the NLO corrections to the quark initiated contribution are strongly suppressed by the experimental cuts. Without applying any cuts, the ratio between $d\sigma_{qq}^{NLO}/dp_T$ and $d\sigma_{qq}^{LO}/dp_T$ is approx. 1.95 for $p_T = 100\,\text{GeV}$. The inclusion of the physical cuts suppress the corrections such that the same ratio is in this case approx. 1.05. The general behaviour of these curves is similar to the case without the physical cuts, figure 5.7, with the distributions reaching a maximum at $p_T \sim 30\,\text{GeV}$, and then sharply decreasing for increasing values of the transverse momentum. Table 5.4 shows the values for the total cross section, obtained using the physical cuts, for the gluon and quark induced contributions to W-boson pair production including leptonic decays. Comparing with the results without physical cuts, table 5.3, it can be clearly seen the effect of the cuts on the gluon initiated background. While the cuts reduce the quark initiated background to 0.5% of the value without the cuts, the gluon initiated background is reduced to 1.7%. This confirms the expectations that the efficiency of the cuts on the gluon initiated background is lower than in the case of qq processes. As explained in Section 5.1.1, the reason for this is that the cuts select events centrally distributed. These events correspond to gluon initiated events, irrespective of them being signal or background. The effect of the cuts is summarized in table 5.5.

Process	Cross Section (fb)		$\sigma_{\text{cuts}}/\sigma_{\text{no cuts}}$
	No Cuts	Cuts applied	
$gg \to W^+W^- \to l^-\bar{\nu}\,l'^+\nu_{l'}$	40.03(6)	0.687(2)	0.01716(6)
$qq \overset{\text{NLO}}{\to} W^+W^- \to l^-\bar{\nu}\,l'^+\nu_{l'}$	1372(2)	7.06(3)	0.00515(2)

Table 5.5: Cuts effect summary: total cross section for gluon and quark induced(NLO) contributions to off-shell W-boson pair production, with a technical cut 1 GeV $< p_T$. The results shown are for cross sections with and without applying the physical cuts. The ratio between these two values, which is shown in the last column, is and indicative of the cuts efficiency.

5.6 Conclusions

The analytic expression for the invariant amplitude corresponding to gluon induced off-shell production of W-boson pairs has been calculated. This symbolic expression has been used to derive the invariant amplitudes for the process

$$gg \to W^-W^+ \to l^-\bar{\nu}\, l'^+\nu_{l'} .$$

The results have been evaluated in the massless, degenerate quarks approximation. The numerical evaluation uses a technical cut on the W-bosons transverse momenta to avoid numerical instabilities caused by the presence of Gram determinants in the amplitudes denominators. These instabilities arise only as a consequence of the calculation technique used, they are not physical. The suppression of gluon induced processes has been confirmed. The ratio between gluon and quark initiated processes is approx 3% without any physical cut. The effect of the set of cuts proposed in ref. [112] was also studied. It was found that the ratio between gluon and quark contributions increases up to almost 10% after the application of these cuts. The ratio between the gluon contribution before and after the application of the cuts is approx. 1.7%, while this ratio for the NLO corrected quark initiated processes is 0.5%.

This results were obtained in the massless quark approximation. It is interesting to evaluate the possible effect of the inclusion of the top/bottom loop diagrams. For $m_{\text{top}} \to \infty$, the top quark decouples and the result of the gluon induced contribution can be calculated with two generations of massless degenerate quarks. On the other hand, for $m_{\text{top}} \to 0$ the gluon contribution can be calculated in the three generations of massless degenerate quarks approximation. This is equivalent to multiplying all the gg results of the previous section by a factor $\frac{9}{4} = 2.25$.

Chapter 6

Conclusions

In this thesis, higher order corrections to Higgs boson production processes and background processes to Higgs-boson searches relevant at hadron colliders have been calculated.

The electroweak $\mathcal{O}(\alpha)$ corrections to Higgs-boson production in association with W or Z bosons at hadron colliders have been calculated. These corrections decrease the theoretical prediction by up to 5–10%, depending in detail on the Higgs-boson mass and the input-parameter scheme. The cross section prediction for associated WH and ZH production at the Tevatron and at the LHC, including the next-to-leading order electroweak and QCD corrections, have been updated. The remaining theoretical uncertainty has been studied by varying the renormalization and factorization scales and by taking into account the uncertainties in the parton distribution functions. It was found that the scale dependence is reduced to about 10% at next-to-leading order, while the uncertainty due to the parton densities is less than about 5%. The electroweak $\mathcal{O}(\alpha)$ corrected cross section and the next-to-next-to-leading order QCD corrected results from [57] were combined, yielding the most precise cross section prediction for a Higgs production process at hadron colliders. Both corrections are of order $5\%-10\%$, but have opposite signs. The theoretical uncertainties are dominated by scale dependence and parton distribution functions uncertainties, which are of order 3% and 5%, respectively. Calculating the ratios of the Higgs production cross section with the corresponding Drell-Yan-like vector boson production process $\sigma_{p\bar{p}/pp\to VH+X}/\sigma_{p\bar{p}/pp\to V+X}$ may further reduce these uncertainties.

The analytic expression for the invariant amplitude corresponding to gluon induced

off-shell production of W-boson pairs has been calculated. This symbolic expression has been used to derive the invariant amplitudes for the process $gg \to W^-W^+ \to l^-\bar{\nu}\, l'^+\nu_{l'}$, a contribution to the main background to Standard Model Higgs-boson searches at the CERN LHC in the mass range $155\,\text{GeV} \lesssim M_H \lesssim 180\,\text{GeV}$. The results have been evaluated in the massless, degenerate quarks approximation, assuming two quarks generations. The suppression of gluon induced processes has been confirmed. The ratio between gluon and quark contributions to $pp \to W^-W^+ \to l^-\bar{\nu}_l\, l'^+\nu_{l'}$ is approx. 3% without any physical cuts. The effect of signal enhancing experimental cuts used in Higgs boson searches was also studied. It was found that the ratio between gluon and quark contributions increases up to 10% after the application of these cuts.

The gluon induced off-shell W-boson pair production calculation presents many opportunities for extensions and improvements. First, an improvement in the representation for the amplitudes in the massless case is advisable to improve the numerical stability of the cross section calculation. The next step involves including the contribution from the massive bottom and top quarks in the loops. In this case, diagrams with both massive and massless quarks circulating the loops, using a non-diagonal CKM matrix, and the fully massive diagrams are needed. Another consequence of introducing massive quarks is that the contribution from the gluon fusion Higgs production process becomes nonzero. Consequently, signal and background interference would be studied. Finally, a comprehensive study of physical distributions defined through the lepton momenta will be carried out, studying the influence of variations of the original set of signal-enhancing cuts.

Appendix A

Spinor Helicity Formalism

For a detailed description of the spinor formalism the reader is directed to ref. [128], of which this Appendix is a very brief summary.

One can consider the massless spinors $u_\pm(p)$ and $v_\pm(p)$ with momentum p ($p^2 = 0$) and helicity $\lambda = \pm$. These spinors satisfy the Dirac equation

$$\not{p}\, u_\pm(p) = \not{p}\, v_\pm(p) = \bar{u}_\pm(p)\not{p} = \bar{v}_\pm(p)\not{p} = 0\,.$$

Using the chirality projectors $\omega_\pm = \frac{1\pm\gamma_5}{2}$ it can be shown that

$$\omega_\mp\, u_\pm(p) = \omega_\pm\, v_\pm(p) = \bar{u}_\pm(p)\,\omega_\pm = \bar{v}_\pm(p)\,\omega_\mp = 0\,.$$

The spinors can also be normalized as

$$\bar{u}_\pm(p)\,\gamma_\mu\,u_\pm(p) = \bar{v}_\pm(p)\,\gamma_\mu\,v_\pm(p) = 2\,p_\mu\,.$$

The following notation is used

$$u_\pm(p) = v_\mp(p) = |p_\pm\rangle\,,$$

$$\bar{u}_\pm(p) = \bar{v}_\mp(p) = \langle p_\pm|\,.$$

For any two massless momenta p and q the spinor products are noted as follows:

$$\begin{aligned}\langle p_-|q_+\rangle &= \langle p\,q\rangle\,,\\ \langle q_+|p_-\rangle &= \langle p\,q\rangle^*\,.\end{aligned}$$

Spinors and spinor products satisfy, among others, the following properties:

$$\begin{aligned} |p_\pm\rangle\langle p_\pm| &= \frac{1}{2}(1 \pm \gamma_5)\not{p}\,, \\ \langle p_+|q_+\rangle &= \langle p_-|q_-\rangle = 0\,, \\ \langle p_-|q_+\rangle &= -\langle q_-|p_+\rangle\,, \\ \langle p_-|p_+\rangle &= \langle p_+|p_-\rangle = 0\,. \end{aligned}$$

An important property satisfied by the spinor product is

$$|\langle p\,q\rangle|^2 = 2\,p\cdot q\,.$$

It can be shown that polarization vectors corresponding to massless vector fields, eg. photons, can be written in terms of spinors and spinor products. Referring to an arbitrary massless momentum q, the polarization vectors corresponding to a vector field of momentum p and helicity $\pm$ read

$$\begin{aligned} \epsilon^+_\mu(p,q) &= \frac{\langle q_-|\gamma_\mu|p_-\rangle}{\sqrt{2}\langle q\,p\rangle}\,, \\ \epsilon^-_\mu(p,q) &= \frac{\langle q_+|\gamma_\mu|p_+\rangle}{\sqrt{2}\langle q\,p\rangle^*}\,. \end{aligned}$$

Appendix B

Function Base for $gg \to W^-W^+$ processes

In this appendix the explicit expressions for the special functions in the Function Base eq. 5.24 are given. These functions arise when the the massless quarks limit is taken and explicit forms for the one-loop scalar integrals are calculated.

$$
\begin{aligned}
D_0^{D=6-2\epsilon}(\hat{s},\hat{t},p_3^3,p_4^2) &= \frac{1}{\hat{u}\hat{t}-p_3^2p_4^2}\left[\hat{t}F_{2A}(\hat{s},\hat{t},p_3^2,p_4^2)\right. \\
&\quad \left. -\frac{1}{2}(\hat{t}p_3^2+\hat{t}p_4^2-\hat{s}\hat{t}-2p_3^2p_4^2)C_0(p_3^2,\hat{s},p_4^2)\right], \\
F_{2A}(\hat{s},\hat{t},p_3^2,p_4^2) &= \mathrm{Li}_2\left(1-\frac{p_3^2}{\hat{t}}\right)+\mathrm{Li}_2\left(1-\frac{p_4^2}{\hat{t}}\right) \\
&\quad +\frac{1}{2}\log\left(\frac{\hat{s}}{\hat{t}}\right)\log\left(\frac{p_4^2}{\hat{t}}\right)+\frac{1}{2}\log\left(\frac{\hat{s}}{p_4^2}\right)\log\left(\frac{p_3^2}{\hat{t}}\right), \\
F_B(\hat{t},\hat{u},p_3^3,p_4^2) &= -\mathrm{Li}_2\left(1-\frac{p_3^2p_4^2}{\hat{t}\hat{u}}\right)+\mathrm{Li}_2\left(1-\frac{p_3^2}{\hat{t}}\right)+\mathrm{Li}_2\left(1-\frac{p_3^2}{\hat{u}}\right) \\
&\quad +\mathrm{Li}_2\left(1-\frac{p_4^2}{\hat{t}}\right)+\mathrm{Li}_2\left(1-\frac{p_4^2}{\hat{u}}\right)+\frac{1}{2}\log\left(\frac{\hat{u}}{\hat{t}}\right)^2, \\
C_0(p_3^2,\hat{s},p_4^2) &= \frac{1}{\sqrt{\lambda(\hat{s},p_3^2,p_4^2)}}\log(a_+a_-)\log\left(\frac{1-a_+}{1-a_-}\right) \\
&\quad +2\mathrm{Li}_2(a_+)-2\mathrm{Li}_2(a_-).
\end{aligned}
$$

In the above expressions,

$$\lambda(x,y,z)=x^2+y^2+z^2-2xy-2xz-2yz,$$

and $a_\pm$ read

$$a_\pm = \frac{1}{2\hat{s}} \left(\hat{s} + p_3^2 - p_4^2 \pm \sqrt{\lambda(\hat{s}, p_3^2, p_4^2)} \right) .$$

Appendix C

Phase Space Parametrization

Phase space parametrization for $1 \to 2$ process

For the process

$$X_0(M) \to X_1(p1) + X_2(p2)\,,$$

working on the CM system it can be shown that

$$p_1^0 = \frac{M^2 + p_1^2 - p_2^2}{2M}\,, \tag{C.1}$$

$$p_2^0 = \frac{M^2 + p_2^2 - p_1^2}{2M}\,, \tag{C.2}$$

$$|\vec{p_i}| = \frac{M}{2}\sqrt{\kappa\left(1, \frac{p_1^2}{M^2}, \frac{p_2^2}{M^2}\right)}\,, \tag{C.3}$$

where $\kappa(a,b,c)$ is the two-body phase space function

$$\kappa(a,b,c) = a^2 + b^2 + c^2 - 2ab - 2ac - 2bc\,. \tag{C.4}$$

Then, the phase space element can be written as

$$dP_2\left[X_0(M) \to X_1(p_1) + X_2(p_2)\right] = \tag{C.5}$$

$$\frac{d^3p_1}{2p_1^0}\frac{d^3p_2}{2p_2^0}\delta^4(M - p_1 - p_2) = \frac{\pi}{2}\sqrt{\kappa\left(1, \frac{p_1^2}{M^2}, \frac{p_2^2}{M^2}\right)}d\Omega. \tag{C.6}$$

with

$$d\Omega = \frac{d\cos(\theta)\,d\varphi}{4\pi}\,.$$

Using this notation the final particles momenta yield

$$p_1^\mu = (p_1^0, |\vec{p}|\,\cos(\varphi)\sin(\theta), |\vec{p}|\,\sin(\varphi)\sin(\theta), |\vec{p}|\,\cos(\theta)) \tag{C.7}$$

$$p_2^\mu = (p_2^0, -\vec{p}_1)\,. \tag{C.8}$$

There are only two independent variables, the polar angle θ and the azimuthal angle φ and the integration limits are

$$4\pi \int d\Omega = \int_0^{\pi} d\theta \ \sin(\theta) \int_0^{2\pi} d\varphi = \int_{-1}^{1} d\cos(\theta) \int_0^{2\pi} d\varphi \,. \tag{C.9}$$

If the particles in the final state are massless, the above formulæ simplify to

$$\frac{d^3p_1}{2p_1^0}\frac{d^3p_2}{2p_2^0}\delta^4(M - p_1 - p_2) = \frac{\pi}{2}d\Omega \,,$$

and the particle momenta yield

$$p_1^{\mu} = \frac{\sqrt{M^2}}{2}(1, \cos(\varphi)\sin(\theta), \sin(\varphi)\sin(\theta), \cos(\theta)) \tag{C.10}$$

$$p_2^{\mu} = \frac{\sqrt{M^2}}{2}(1, -\cos(\varphi)\sin(\theta), -\sin(\varphi)\sin(\theta), -\cos(\theta)) \,. \tag{C.11}$$

Phase space parametrization for a $1 \to 4$ process

The four-body phase space element can be written as a combination of two-body phase space elements

$$dP_4\,[X_0(M) \to X_1(p_1) + X_2(p_2) + X_3(p_3) + X_4(p_4)] =$$

$$dq_1{}^2 dq_2{}^2 \; dP_2\,[X_0(M) \to Y_1(q_1) + Y_2(q_2)]$$

$$dP_2\,[Y_1(q_1) \to X_1(p_1) + X_2(p_2)]$$

$$dP_2\,[Y_2(q_2) \to X_3(p_3) + X_4(p_4)] \,.$$

This parametrization can be applied to the process

$$g(p_1)\; g(p_2) \;\to\; W^{-*}(p_3)\; W^{+*}(p_4) \;\to\; l(p_5)\; \bar{\nu}_l(p_6)\; \bar{l}'(p_7)\; \nu_{l'}(p_8) \tag{C.12}$$

in the following way:

$$\frac{d^3p_5}{2p_5^0}\frac{d^3p_6}{2p_6^0}\frac{d^3p_7}{2p_7^0}\frac{d^3p_8}{2p_8^0}\delta^4(p_1 + p_2 - p_5 - p_6 - p_7 - p_8) =$$

$$dp_3^2 dp_4^2 \; \frac{d^3p_3}{2p_3^0}\frac{d^3p_4}{2p_4^0}\delta^4(p_1 + p_2 - p_3 - p_4)$$

$$\frac{d^3p_5}{2p_5^0}\frac{d^3p_6}{2p_6^0}\delta^4(p_3 - p_5 - p_6)\frac{d^3p_7}{2p_7^0}\frac{d^3p_8}{2p_8^0}\delta^4(p_4 - p_7 - p_8) \,.$$

Using the $1 \to 2$ results one obtains

$$\begin{aligned}
\frac{d^3p_3}{2p_3^0}\frac{d^3p_4}{2p_4^0}\delta^4(p_1+p_2-p_3-p_4) &= \frac{\pi}{2}\sqrt{\kappa\left(1,\frac{p_3^2}{\hat{s}},\frac{p_4^2}{\hat{s}}\right)}d\Omega_{34} \\
\frac{d^3p_5}{2p_5^0}\frac{d^3p_6}{2p_6^0}\delta^4(p_3-p_5-p_6) &= \frac{\pi}{2}d\Omega_{56} \\
\frac{d^3p_7}{2p_7^0}\frac{d^3p_8}{2p_8^0}\delta^4(p_4-p_7-p_8) &= \frac{\pi}{2}d\Omega_{78}\,,
\end{aligned}$$

where $p_{i,i+1}$ are calculated in the $i, i+1$ CM frame ($i = 3, 5, 6$).

Presence of Breit Wigner factors

There are eight independent integration variable: 2 angular variables for each $1 \to 2$ sub-process, and the invariant masses p_3^2 and p_4^2. The constraints over the invariant masses are

$$\begin{aligned}
0 &\leq \sqrt{p_{3,4}^2} \\
\sqrt{p_3^2}+\sqrt{p_4^2} &\leq \hat{s}\,,
\end{aligned} \tag{C.13}$$

while the angular variables verify eq. C.9.

In the process shown in eq. C.12, using the narrow width approximation, the factor

$$\frac{1}{(p_3^2-M_W^2)^2+(\Gamma_W M_W)^2}\,\frac{1}{(p_4^2-M_W^2)^2+(\Gamma_W M_W)^2} \tag{C.14}$$

multiplies the differential cross section. The elimination of this factors may be necessary in order to improve the convergence of integration algorithms used to obtain integrated cross sections. The change of variables

$$\xi_{i=3,4} = \frac{1}{\Gamma_W M_W}\arctan\left(\frac{p_i^2-M_W^2}{\Gamma_W M_W}\right) \tag{C.15}$$

$$d\xi_{i=3,4} = \frac{dp_i^2}{(p_i^2-M_W^2)^2+(\Gamma_W M_W)^2} \tag{C.16}$$

has the desired effect. The integration limits for the new $\xi_{3,4}$ variables are easily obtained. Making use of the constraints in eq. C.13 one obtains

$$\begin{aligned}
-\frac{1}{\Gamma_W M_W}\arctan\left(\frac{M_W}{\Gamma_W}\right) \leq\ & \xi_3 \leq \frac{1}{\Gamma_W M_W}\arctan\left(\frac{\hat{s}-M_W^2}{\Gamma_W M_W}\right) \\
-\frac{1}{\Gamma_W M_W}\arctan\left(\frac{M_W}{\Gamma_W}\right) \leq\ & \xi_4 \leq \frac{1}{\Gamma_W M_W}\arctan\left(\frac{(\sqrt{\hat{s}}-\sqrt{p_3^2})^2-M_W^2}{\Gamma_W M_W}\right).
\end{aligned}$$

Presence of inverse powers of $|p_{3,4}^{\mathrm{T}}|$

If there are negative powers of the transverse momenta in the expression for the differential cross section, the behaviour of the VEGAS Monte Carlo algorithm may be improved using $|p_{3,4}^{\mathrm{T}}|$ as integration variable. To this effect the change of variables

$$
\begin{aligned}
{p_3}^2, {p_4}^2 &\rightarrow {p_3}^2, |p_{\mathrm{T}}|^2 && \text{(C.17)}\\
{p_4}^2 &= \hat{s} + {p_3}^2 - 2\sqrt{\hat{s}(|\vec{p}_3|^2 + {p_3}^2)} && \text{(C.18)}\\
\frac{\partial({p_3}^2, {p_4}^2)}{\partial({p_3}^2, |p_{\mathrm{T}}|^2)} &= \frac{2}{\sin^2(\theta)} \frac{\hat{s}}{\hat{s} + {p_3}^2 - {p_4}^2} && \text{(C.19)}
\end{aligned}
$$

is introduced. The phase space element

$$
d{p_3}^2 d{p_4}^2 \, dP_2 \left[g(p_1) + g(p_2) \rightarrow W^-(p_3) + W^+(p_4) \right]
$$

can then be expressed as

$$
d{p_3}^2 d{p_4}^2 \frac{d^3p_3}{2p_3^0} \frac{d^3p_4}{2p_4^0} = \frac{2}{\sin^2(\theta)} \frac{\hat{s}}{\hat{s} + {p_3}^2 - {p_4}^2} d|\vec{p}_T|^2 d{p_3}^2 \frac{d\Omega_{3,4}}{4\pi} . \qquad \text{(C.20)}
$$

In this case, the calculation of the integration limits is not as easy as in the previous choices of phase space parametrization. First, note that, due to energy conservation,the p_T^2 integration limits are

$$
0 \leq p_T^2 \leq \frac{\hat{s}}{4} .
$$

Also note that

$$
\begin{aligned}
|\vec{p}|^2 &\leq \hat{s} && \text{(C.21)}\\
\frac{|p_T|^2}{\sin^2(\theta)} &\leq \hat{s} && \text{(C.22)}\\
\frac{|p_T|^2}{1 - \cos^2(\theta)} &\leq \hat{s} , && \text{(C.23)}\\
& && \text{(C.24)}
\end{aligned}
$$

and finally

$$
-\sqrt{1 - \frac{4p_T^2}{s}} \leq \cos(\theta) \leq \sqrt{1 - \frac{4p_T^2}{s}} .
$$

With $|p_T|^2$ and $\cos(\theta)$ the value of $|\vec{p}|$ can be calculated, which is then used to establish the integration limits for ${p_3}^2 2$:

$$
\begin{aligned}
4\hat{s}|\vec{p}|^2 &= (\hat{s} + p_3^2 - p_4^2)^2 - 4p_3^2\hat{s} && \text{(C.25)}\\
p_4^2 &= \hat{s} + p_3^2 - \sqrt{4p_3^2\hat{s} + 4\hat{s}|\vec{p}|^2} . && \text{(C.26)}
\end{aligned}
$$

Imposing

$$\begin{aligned} 0 &\leq p_{3,4}^2 \\ \sqrt{p_3^2} + \sqrt{p_4^2} &\leq \hat{s}\,, \end{aligned}$$

the following limits of integration for p_3^2 are obtained

$$0 \leq p_3^2 \leq \hat{s}\left(1 - 2\frac{|\vec{p}|}{\sqrt{\hat{s}}}\right).$$

Finally the azimuthal angle integration limits are $[0, 2\pi]$.

Simultaneous presence of Breit Wigner factors and inverse powers of $|p_{3,4}^{\mathrm{T}}|$

If the integrand contains both, Breit Wigner factors and negative powers of transverse momenta, a mixed approach can be used. The following parametrization allows for the simplification of one Breit Wigner factor and the use of P_T as integration variable. The phase space element is obtained applying the change of variables C.15 to p_3^2 in eq. C.20. The final expression for the phase space element is given by

$$\begin{aligned} &dP_4\left[X_0(M) \to X_1(p_1) + X_2(p_2) + X_3(p_3) + X_4(p_4)\right] = \\ &= \hat{s}\frac{2\pi^3}{\sin^2(\theta)}\frac{\left[(p_3^2 - M_W^2)^2 + (\Gamma_W M_W)^2\right]}{\hat{s} + {p_3}^2 - {p_4}^2} d|\vec{p}_T|^2 d\xi_3 d\Omega_{3,4} d\Omega_{5,6} d\Omega_{7,8} \end{aligned} \tag{C.27}$$

Bibliography

[1] S. L. Glashow, Nucl. Phys. **22** (1961) 579.

[2] S. Weinberg, Phys. Rev. Lett. **19** (1967) 1264.

[3] A. Salam, "Weak And Electromagnetic Interactions," Originally printed in Svartholm: Elementary Particle Theory, Proceedings Of The Nobel Symposium Held 1968 At Lerum, Sweden, Stockholm 1968, 367-377.

[4] S. L. Glashow, J. Iliopoulos and L. Maiani, Phys. Rev. D **2**, 1285 (1970).

[5] M. L. Perl *et al.*, Phys. Rev. Lett. **35** (1975) 1489.

[6] S. W. Herb *et al.*, Phys. Rev. Lett. **39** (1977) 252.

[7] S. Abachi *et al.* [D0 Collaboration], Phys. Rev. Lett. **74** (1995) 2632 [arXiv:hep-ex/9503003].

[8] F. Abe *et al.* [CDF Collaboration], Phys. Rev. Lett. **74** (1995) 2626 [arXiv:hep-ex/9503002].

[9] G. Arnison *et al.* [UA1 Collaboration], Phys. Lett. B **126** (1983) 398.

[10] G. Arnison *et al.* [UA1 Collaboration], Phys. Lett. B **122** (1983) 103.

[11] M. Banner *et al.* [UA2 Collaboration], Phys. Lett. B **122** (1983) 476.

[12] The LEP Electroweak Working Group and the SLD Heavy Flavor and Electroweak Groups, Summer 2004 results.

[13] P. W. Higgs, Phys. Lett. **12** (1964) 132; Phys. Rev. Lett. **13** (1964) 508 and Phys. Rev. **145** (1966) 1156;

F. Englert and R. Brout, Phys. Rev. Lett. **13** (1964) 321;
G. S. Guralnik, C. R. Hagen and T. W. Kibble, Phys. Rev. Lett. **13** (1964) 585;
T. W. Kibble, Phys. Rev. **155** (1967) 1554.

[14] R. Barate *et al.* [ALEPH Collaboration], Phys. Lett. B **565** (2003) 61 [arXiv:hep-ex/0306033].

[15] ATLAS Collaboration, Technical Design Report, Vols. 1 and 2, CERN–LHCC–99–14 and CERN–LHCC–99–15;
CMS Collaboration, Technical Proposal, CERN–LHCC–94–38.

[16] W. W. Armstrong *et al.* [ATLAS Collaboration], "ATLAS: Technical proposal for a general-purpose p p experiment at the Large Hadron Collider at CERN", CERN-LHCC-94-43

[17] D. Denegri, CERN-PPE-90-181 *Presented at the ECFA Large Hadron Collider Workshop, Aachen, Germany, Oct 4-9, 1990*

[18] W. Heisenberg, Z. Physik **49** (1928) 619.

[19] Y. Nambu and G. Jona-Lasinio, Phys. Rev. **122** (1961) 345.

[20] Y. Nambu and G. Jona-Lasinio, Phys. Rev. **124** (1961) 246.

[21] M. Baker and S. L. Glashow Phys. Rev. **128** (1962) 2462

[22] J. Goldstone, Nuovo Cim. **19** (1961) 154.

[23] J. Goldstone, A. Salam and S. Weinberg, Phys. Rev. **127** (1962) 965.

[24] M. Bohm, A. Denner and H. Joos, "Gauge theories of the strong and electroweak interaction", Stuttgart, Germany: Teubner (2001).

[25] K. Fujikawa, B. W. Lee and A. I. Sanda, Phys. Rev. D **6** (1972) 2923.

[26] G. 't Hooft, Nucl. Phys. B **35** (1971) 167.

[27] G. 't Hooft, Nucl. Phys. B **33** (1971) 173.

[28] G. 't Hooft and M. J. G. Veltman, Nucl. Phys. B **44** (1972) 189.

[29] W. Hollik, AIP Conf. Proc. **490** (1999) 10.

[30] W. Hollik, *Prepared for ICTP Summer School in Particle Physics, Trieste, Italy, 21 Jun - 9 Jul 1999*

[31] A. Denner, Fortsch. Phys. **41** (1993) 307.

[32] T. P. Cheng and L. F. Lee, "Gauge Theory of Elementary Particle Physics". Oxford: Clarendon Press, 1984.

[33] R. K. Ellis, W. J. Stirling and B. R. Webber, "QCD and collider physics". Cambridge: Cambridge University Press, 1996.

[34] K. Riesselmann, arXiv:hep-ph/9711456.

[35] T. Hambye and K. Riesselmann, Phys. Rev. D **55** (1997) 7255

[36] W. Langguth and I. Montvay, Z. Phys. C **36**, 725 (1987). A. Hasenfratz, K. Jansen, C. B. Lang, T. Neuhaus and H. Yoneyama, Phys. Lett. B **199**, 531 (1987). A. Hasenfratz and T. Neuhaus, "Upper Bound Estimate For The Higgs Mass From The Lattice Regularized Nucl. Phys. B **297**, 205 (1988). P. Hasenfratz and J. Nager, "The Cutoff Dependence Of The Higgs Meson Mass And The Onset Of New Physics In Z. Phys. C **37**, 477 (1988). U. M. Heller, H. Neuberger and P. Vranas, Nucl. Phys. B **399**, 271 (1993) [arXiv:hep-lat/9207024].

[37] M. Luscher and P. Weisz, Phys. Lett. B **212**, 472 (1988).

[38] M. Gockeler, H. A. Kastrup, T. Neuhaus and F. Zimmermann, Nucl. Phys. B **404**, 517 (1993) [arXiv:hep-lat/9206025].

[39] U. M. Heller, M. Klomfass, H. Neuberger and P. Vranas, Nucl. Phys. B **405**, 555 (1993) [arXiv:hep-ph/9303215].

[40] G. Altarelli and G. Isidori, Phys. Lett. B **337** (1994) 141.

[41] J. A. Casas, J. R. Espinosa and M. Quiros, Phys. Lett. B **342** (1995) 171 [arXiv:hep-ph/9409458].

[42] J. A. Casas, J. R. Espinosa and M. Quiros, Phys. Lett. B **382** (1996) 374 [arXiv:hep-ph/9603227].

[43] K. Holland and J. Kuti, Nucl. Phys. Proc. Suppl. **129** (2004) 765 [arXiv:hep-lat/0308020].
K. Holland, arXiv:hep-lat/0409112.

[44] A. Djouadi, J. Kalinowski and M. Spira, Comput. Phys. Commun. **108** (1998) 56 [arXiv:hep-ph/9704448].

[45] M. Spira, Fortsch. Phys. **46** (1998) 203 [arXiv:hep-ph/9705337].

[46] M. Spira, arXiv:hep-ph/9810289.

[47] L. Reina and S. Dawson, Phys. Rev. Lett. **87**, 201804(2001); L. Reina, S. Dawson and D. Wackeroth, Phys. Rev. D. **65**, 053017 (2002).

[48] W. Beenakker, S. Dittmaier, M. Krämer, B. Plumper, M. Spira and P. M. Zerwas, Phys. Rev. Lett. **87**, 201805(2001);

[49] Report of the Tevatron Higgs working group, M. Carena, J. S. Conway, H. E. Haber, J. D. Hobbs *et al.* [hep-ph/0010338].

[50] L. Babukhadia *et al.* [CDF and D0 Working Group Members Collaboration], FERMILAB-PUB-03-320-E

[51] D. L. Rainwater and D. Zeppenfeld, JHEP **9712**, 005 (1997) [arXiv:hep-ph/9712271].

[52] D. L. Rainwater, D. Zeppenfeld and K. Hagiwara, Phys. Rev. D **59**, 014037 (1999) [arXiv:hep-ph/9808468].

[53] T. Plehn, D. L. Rainwater and D. Zeppenfeld, "A method for identifying H $\rightarrow$ tau tau $\rightarrow$ e+- mu-+ missing p(T) at the Phys. Rev. D **61**, 093005 (2000) [arXiv:hep-ph/9911385].

[54] D. L. Rainwater and D. Zeppenfeld, "Observing $H \rightarrow W^{(*)}W^{(*)} \rightarrow e^{\pm}\mu^{\mp}\not{p}_T$ in weak boson Phys. Rev. D **60**, 113004 (1999) [Erratum-ibid. D **61**, 099901 (2000)] [arXiv:hep-ph/9906218].

[55] N. Kauer, T. Plehn, D. L. Rainwater and D. Zeppenfeld, Phys. Lett. B **503**, 113 (2001) [arXiv:hep-ph/0012351].

[56] S. Abdullin et al., CMS Note 2003/33.

[57] O. Brein, A. Djouadi and R. Harlander, Phys. Lett. B **579**, 149 (2004) [arXiv:hep-ph/0307206].

[58] The LEP Working Group for Higgs Boson Searches, LHWG Note/2002-01.

[59] The LEP Electroweak Working Group and the SLD Heavy Flavor and Electroweak Groups, D. Abbaneo *et al.*, LEPEWWG/2003-01.

[60] S. L. Glashow, D. V. Nanopoulos and A. Yildiz, Phys. Rev. D **18** (1978) 1724;
Z. Kunszt, Z. Trócsány and W. J. Stirling, Phys. Lett. B **271** (1991) 247.

[61] T. Han and S. Willenbrock, Phys. Lett. B **273**, 167 (1991);
J. Ohnemus and W. J. Stirling, Phys. Rev. D **47** (1993) 2722;
H. Baer, B. Bailey and J. F. Owens, Phys. Rev. D **47** (1993) 2730;
S. Mrenna and C. P. Yuan, Phys. Lett. B **416** (1998) 200 [hep-ph/9703224];
M. Spira, Fortsch. Phys. **46** (1998) 203 [hep-ph/9705337].

[62] D. A. Dicus and S. S. Willenbrock, Phys. Rev. D **34** (1986) 148;
D. A. Dicus and C. Kao, Phys. Rev. D **38** (1988) 1008 [Erratum-ibid. D **42** (1990) 2412];
V. D. Barger, E. W. Glover, K. Hikasa, W. Y. Keung, M. G. Olsson, C. J. Suchyta and X. R. Tata, Phys. Rev. Lett. **57** (1986) 1672;
B. A. Kniehl, Phys. Rev. D **42** (1990) 2253.

[63] R. Hamberg, W. L. van Neerven and T. Matsuura, Nucl. Phys. B **359** (1991) 343;
W. L. van Neerven and E. B. Zijlstra, Nucl. Phys. B **382** (1992) 11.

[64] U. Baur, S. Keller and D. Wackeroth, Phys. Rev. D **59** (1999) 013002 [hep-ph/9807417].

[65] S. Dittmaier and M. Krämer, Phys. Rev. D **65** (2002) 073007 [hep-ph/0109062].

[66] U. Baur, S. Keller and W. K. Sakumoto, Phys. Rev. D **57** (1998) 199 [hep-ph/9707301];
U. Baur, O. Brein, W. Hollik, C. Schappacher and D. Wackeroth, Phys. Rev. D **65** (2002) 033007 [hep-ph/0108274].

[67] J. Fleischer and F. Jegerlehner, Nucl. Phys. B **216** (1983) 469;
B. A. Kniehl, Z. Phys. C **55** (1992) 605;
A. Denner, J. Küblbeck, R. Mertig and M. Böhm, Z. Phys. C **56** (1992) 261.

[68] F. Jegerlehner, DESY 01-029, LC-TH-2001-035 [hep-ph/0105283].

[69] A. Denner, S. Dittmaier, M. Roth and M. M. Weber, Nucl. Phys. B **660** (2003) 289 [hep-ph/0302198].

[70] J. Küblbeck, M. Böhm and A. Denner, Comput. Phys. Commun. **60** (1990) 165;
H. Eck and J. Küblbeck, *Guide to FeynArts 1.0*, University of Würzburg, 1992.

[71] T. Hahn, Comput. Phys. Commun. **140** (2001) 418 [hep-ph/0012260].

[72] G. 't Hooft and M. J. G. Veltman, Nucl. Phys. B **153** (1979) 365.

[73] G. Passarino and M. J. G. Veltman, Nucl. Phys. B **160** (1979) 151.

[74] W. Beenakker and A. Denner, Nucl. Phys. B **338** (1990) 349;
A. Denner, U. Nierste and R. Scharf, Nucl. Phys. B **367** (1991) 637.

[75] R. Mertig, M. Böhm and A. Denner, Comput. Phys. Commun. **64** (1991) 345;
R. Mertig, *Guide to FeynCalc 1.0*, University of Würzburg, 1992.

[76] T. Hahn, Nucl. Phys. Proc. Suppl. **89** (2000) 231 [hep-ph/0005029].

[77] A. Sirlin, Phys. Rev. D **22** (1980) 971;
W. J. Marciano and A. Sirlin, Phys. Rev. D **22** (1980) 2695 [Erratum-ibid. D **31** (1980) 213] and Nucl. Phys. B **189** (1981) 442.

[78] B. A. Kniehl and M. Steinhauser, Nucl. Phys. B **454** (1995) 485 [hep-ph/9508241].

[79] T. Stelzer and W. F. Long, Comput. Phys. Commun. **81** (1994) 357 [hep-ph/9401258];
F. Maltoni and T. Stelzer, JHEP **0302** (2003) 027 [hep-ph/0208156].

[80] H. Murayama, I. Watanabe and K. Hagiwara, KEK-91-11.

[81] S. Dittmaier, Nucl. Phys. B **565** (2000) 69 [hep-ph/9904440].

[82] S. Catani and M. H. Seymour, Phys. Lett. B **378** (1996) 287 [hep-ph/9602277] and Nucl. Phys. B **485** (1997) 291 [Erratum-ibid. B **510** (1997) 291] [hep-ph/9605323].

[83] J. Kripfganz and H. Perlt, Z. Phys. C **41** (1988) 319;
H. Spiesberger, Phys. Rev. D **52** (1995) 4936 [hep-ph/9412286].

[84] K. Hagiwara *et al.* [Particle Data Group Collaboration], Phys. Rev. D **66** (2002) 010001.

[85] J. Pumplin, D. R. Stump, J. Huston, H. L. Lai, P. Nadolsky and W. K. Tung, JHEP **0207** (2002) 012 [hep-ph/0201195].

[86] T. Bhattacharya and S. Willenbrock, Phys. Rev. D **47** (1993) 4022;
B. A. Kniehl, C. P. Palisoc and A. Sirlin, Phys. Rev. D **66** (2002) 057902 [hep-ph/0205304].

[87] G. Belanger *et al.*, hep-ph/0211268; Phys. Lett. B **559** (2003) 252 [hep-ph/0212261];
A. Denner, S. Dittmaier, M. Roth and M. M. Weber, Phys. Lett. B **560** (2003) 196 [hep-ph/0301189].

[88] C. S. Li and S. H. Zhu, Phys. Lett. B **444** (1998) 224 [hep-ph/9801390];
Q. H. Cao, C. S. Li and S. H. Zhu, Commun. Theor. Phys. **33** (2000) 275 [hep-ph/9810458].

[89] A. D. Martin, R. G. Roberts, W. J. Stirling and R. S. Thorne, Eur. Phys. J. C **28** (2003) 455 [arXiv:hep-ph/0211080].

[90] A. D. Martin, R. G. Roberts, W. J. Stirling and R. S. Thorne, Eur. Phys. J. C **23** (2002) 73 [arXiv:hep-ph/0110215].

[91] O. Brein, M. Ciccolini, S. Dittmaier, A. Djouadi, R. Harlander and M. Kramer, arXiv:hep-ph/0402003.

[92] R. Hamberg, W. L. van Neerven and T. Matsuura, "A Complete Calculation Of The Order Alpha-S**2 Correction To The Drell-Yan K Nucl. Phys. B **359**, 343 (1991) [Erratum-ibid. B **644**, 403 (2002)].

[93] W. L. van Neerven and E. B. Zijlstra, Nucl. Phys. B **382**, 11 (1992) [Erratum-ibid. B **680**, 513 (2004)].

[94] R. V. Harlander and W. B. Kilgore, Phys. Rev. Lett. **88**, 201801 (2002) [arXiv:hep-ph/0201206].

[95] V. D. Barger, E. W. N. Glover, K. Hikasa, W. Y. Keung, M. G. Olsson, C. J. Suchyta and X. R. Tata, "Higgs Boson Z0 Associated Production From Fourth Generation Quarks At Super Phys. Rev. Lett. **57**, 1672 (1986).

[96] D. A. Dicus and C. Kao, Phys. Rev. D **38**, 1008 (1988) [Erratum-ibid. D **42**, 2412 (1990)].

[97] B. A. Kniehl, "Associated Production Of Higgs And Z Bosons From Gluon Fusion In Hadron Phys. Rev. D **42**, 2253 (1990).

[98] D. L. Rainwater, M. Spira and D. Zeppenfeld, arXiv:hep-ph/0203187.

[99] L. J. Dixon, Z. Kunszt and A. Signer, Nucl. Phys. B **531** (1998) 3 [arXiv:hep-ph/9803250].

[100] L. J. Dixon, Z. Kunszt and A. Signer, Phys. Rev. D **60** (1999) 114037 [arXiv:hep-ph/9907305].

[101] D. A. Dicus, C. Kao and W. W. Repko, Phys. Rev. D **36** (1987) 1570.

[102] C. Kao and D. A. Dicus, Phys. Rev. D **43**, 1555 (1991).

[103] E. W. N. Glover and J. J. van der Bij, Phys. Lett. B **219** (1989) 488.

[104] E. W. N. Glover, J. Ohnemus and S. S. D. Willenbrock, Phys. Rev. D **37** (1988) 3193.

[105] V. D. Barger, G. Bhattacharya, T. Han and B. A. Kniehl, Phys. Rev. D **43** (1991) 779.

[106] T. Han, A. S. Turcot and R. J. Zhang, Phys. Rev. D **59** (1999) 093001 [arXiv:hep-ph/9812275].

[107] J. M. Campbell and R. K. Ellis, Phys. Rev. D **60** (1999) 113006 [arXiv:hep-ph/9905386].

[108] M. Dittmar and H. K. Dreiner, Phys. Rev. D **55** (1997) 167 [arXiv:hep-ph/9608317].

[109] M. Dittmar and H. K. Dreiner, arXiv:hep-ph/9703401.

[110] M. Dittmar and H. K. Dreiner, CMS Note 1997/083

[111] K. Jacobs and T. Trefzger ATL-PHYS-2000-015

[112] G. Davatz, G. Dissertori, M. Dittmar, M. Grazzini and F. Pauss, JHEP **0405** (2004) 009 [arXiv:hep-ph/0402218].

[113] T. Sjostrand, P. Eden, C. Friberg, L. Lonnblad, G. Miu, S. Mrenna and E. Norbin, Comput. Phys. Commun. **135** (2001) 238 [arXiv:hep-ph/0010017].

[114] C. A. Nelson, Phys. Rev. D **37** (1988) 1220.

[115] J. C. Pumplin, W. W. Repko and G. L. Kane, Print-86-1256 (MICHIGAN STATE)

[116] L. Ametller, E. Gava, N. Paver and D. Treleani, Phys. Rev. D **32** (1985) 1699.

[117] D. A. Dicus, Phys. Rev. D **38** (1988) 394.

[118] D. A. Dicus, S. L. Wilson and R. Vega, Phys. Lett. B **192**, 231 (1987).

[119] E. W. N. Glover and J. J. van der Bij, Nucl. Phys. B **321** (1989) 561.

[120] C. Zecher, T. Matsuura and J. J. van der Bij, Z. Phys. C **64** (1994) 219 [arXiv:hep-ph/9404295].

[121] K. L. Adamson, D. de Florian and A. Signer, Phys. Rev. D **67** (2003) 034016 [arXiv:hep-ph/0211295].

[122] K. L. Adamson, D. de Florian and A. Signer, Phys. Rev. D **65** (2002) 094041 [arXiv:hep-ph/0202132].

[123] P. Breitenlohner and D. Maison, Commun. Math. Phys. **52** (1977) 11.

[124] P. Breitenlohner and D. Maison, Commun. Math. Phys. **52** (1977) 39.

[125] P. Breitenlohner and D. Maison, Commun. Math. Phys. **52** (1977) 55.

[126] T. Binoth, E. W. N. Glover, P. Marquard and J. J. van der Bij, JHEP **0205** (2002) 060 [arXiv:hep-ph/0202266].

[127] J. A. M. Vermaseren, arXiv:math-ph/0010025.

[128] Z. Xu, D. H. Zhang and L. Chang, Nucl. Phys. B **291** (1987) 392.

[129] C. Dams and R. Kleiss, Eur. Phys. J. C **34** (2004) 419 [arXiv:hep-ph/0401136].

[130] D. Y. Bardin and G. Passarino, The standard model in the making : precision study of the electroweak interactions, Oxford : Clarendon Press, 1999.

[131] W. Beenakker and A. Denner, Int. J. Mod. Phys. A **9** (1994) 4837.

[132] G. P. Lepage, J. Comput. Phys. **27** (1978) 192.

[133] P. B. Renton, arXiv:hep-ph/0410177.

[134] A. Abbasabadi and W. W. Repko, Phys. Rev. D **37** (1988) 2668.

[135] M. J. Duncan, G. L. Kane and W. W. Repko, Nucl. Phys. B **272** (1986) 517.

[136] M. J. Duncan, Phys. Lett. B **179** (1986) 393.

[137] J. J. van der Bij and E. W. N. Glover, Phys. Lett. B **206** (1988) 701.

[138] J. J. van der Bij and E. W. N. Glover, Nucl. Phys. B **313** (1989) 237.

[139] U. Baur, E. W. N. Glover and J. J. van der Bij, Nucl. Phys. B **318** (1989) 106.

[140] B. Mele, P. Nason and G. Ridolfi, "QCD Radiative Corrections To Z Boson Pair Production In Hadronic Nucl. Phys. B **357**, 409 (1991).

[141] S. Frixione, P. Nason and G. Ridolfi, Nucl. Phys. B **383**, 3 (1992).

[142] S. Frixione, Nucl. Phys. B **410**, 280 (1993).

[143] J. Ohnemus and J. F. Owens, Phys. Rev. D **43**, 3626 (1991).

[144] J. Ohnemus, Phys. Rev. D **44**, 1403 (1991).

[145] J. Ohnemus, Phys. Rev. D **44**, 3477 (1991).